

Cover Page



Universiteit Leiden



The handle <http://hdl.handle.net/1887/20986> holds various files of this Leiden University dissertation.

Author: Akkılıç, Namık

Title: Fluorescent electrochemistry : towards controlled redox-switching of a single metalloprotein

Issue Date: 2013-06-20

Fluorescent Electrochemistry

Towards controlled redox-switching of a single metalloprotein

Proefschrift

ter verkrijging van
de graad van Doctor aan de Universiteit Leiden,
op gezag van Rector Magnificus Prof.mr. C.J.J.M. Stolker,
volgens besluit van het College voor Promoties
te verdedigen op donderdag 20 juni 2013
klokke 11.15 uur

door

Namık Akkılıç

geboren te Istanbul, Turkije
in 1979

Promotiecommissie:

Promotores:	Prof. dr. T.J. Aartsma	Universiteit Leiden
	Prof. dr. G.W. Canters	Universiteit Leiden
Overige Leden:	Prof. dr. E.R. Eliel	Universiteit Leiden
	Prof. dr. A.M. van Oijen	Rijksuniversiteit Groningen
	Prof. dr. T. Schmidt	Universiteit Leiden
	Prof. dr. G.T. Robillard	Rijksuniversiteit Groningen

Dit onderzoek werd mede gefinancierd door het Marie Curie Research Training Network “EdRox” (contract no. MRTN-CT-2006-035649)

© 2013. All rights reserved.

ISBN: 978-90-8593-156-0

Casimir PhD series, Delft-Leiden 2013-16

Printed by: Uitgeverij BOXPress (Proefschriftmaken.nl)

*This thesis is dedicated to my parents,
for their endless love and encouragement.*

Cover design by Kerem Masaracı & Namık Akkılıç

Front: Fluorescence intensity time trace of Cy5 labeled azurin in response to an applied potential.

Back: Artistic depiction of Cy5 labeled single azurin molecules on an octanethiol-modified thin gold layer.

Table of Contents

1. Introduction	3
1.1 Introduction	4
1.2 The FluRedox principle	5
1.3 A metalloprotein: Azurin	7
1.4 Experimental Methods	8
1.4.1 Electrochemistry	8
1.4.2 Introduction to Fluorescence	13
1.4.3 Fluorescence Resonance Energy Transfer (FRET)	15
1.4.4 FluRedox Principle applied to azurin	16
1.5 Single molecule detection techniques in this thesis	18
1.5.1 Fluorescence electrochemistry	18
1.5.2 Chemically-induced SM fluorescence spectroscopy	20
1.6 Scope of this thesis	22
References	22
2. Fluorescent cyclic voltammetry of immobilized azurin: Direct observation of thermodynamic and kinetic heterogeneity	27
2.1 Introduction	29
2.2 Results and Discussion	29
2.3 Experimental Section	36
2.3.1 Sample preparation	36
2.3.2 Sample immobilization and electrode preparation	37
2.3.3 Fluorescent electrochemistry setup	37
2.3.4 Electrochemistry	37
2.4 Appendix	38
2.4.1 Cyclic and fluorescent voltammetry	38
2.4.2 Fluorescence time traces and switching ratio	39
2.4.3 Fluorescent cyclic voltammograms-scan rate dependence	40
2.4.4 Non FRET coupled emission changes	42
2.4.5 Analyzing the CV data with Butler-Volmer theory	43
2.4.6 Analyzing the FCV data	45
2.4.7 Comparison between conventional CV-full-image FCV data	50
2.4.8 Sample Size	53
2.4.9 Width calculations of E_0 and k_0 histograms	54
2.4.10 Sample preparation	55
2.4.11 Sample immobilization and electrode preparation	55
2.4.12 Fluorescent electrochemistry setup	57
References	59

3. Fluorescence-detected electrochemistry of single redox proteins reveals the thermodynamic dispersion	65
3.1 Introduction	67
3.2 Experimental Section	72
3.2.1 Sample preparation	72
3.2.2 Fluorescence time courses in bulk	73
3.2.3 Azurin immobilization on gold	73
3.2.4 Surface characterization	75
3.2.5 Fluorescent electrochemistry setup	75
3.3 Results	77
3.3.1 Purification of Az-Cy5	77
3.3.2 Fluorescence switching ratio (SR) in bulk	78
3.3.3 Topography of Az-Cy5-functionalized thin Au film	80
3.3.4 Electrochemical Measurements	81
3.3.5 Fluorescence-electrochemistry on SM azurins	84
3.4 Discussion	89
3.5 Conclusion	93
References	93
4. Chemically-induced redox switching of single azurin molecules	99
4.1 Introduction	101
4.2 Experimental Section	104
4.2.1 Azurin Purification and Labeling	104
4.2.2 Purification of labeled species	106
4.2.3 Absorption and Fluorescence Spectroscopy	107
4.2.4 Azurin immobilization on glass	107
4.2.5 Single molecule imaging setup and single photon counting	109
4.2.6 Redox potential of buffer solution	111
4.2.7 Data elaboration and analysis	111
4.3 Redox thermodynamics of single molecules	113
4.4 Results	116
4.4.1 Purification of labeled azurin	116
4.4.2 Fluorescence switching in bulk	117
4.4.3 Resolving fluorescence time trace	118
4.4.4 Heterogeneity in fluorescence lifetimes	123
4.4.5 Redox parameters of a single Az-Cy5 molecule	124
4.4.6 Electron transfer kinetics of a single azurin	127
4.5 Discussion	128
4.6 Conclusions	132
References	133
Summary	139
Samenvatting	143
List of Publications	149
Curriculum Vitae	151

Chapter 1

Introduction

1.1 Introduction

Metalloproteins, accounting for almost half of all proteins in nature, are at the heart of many vital oxidation and reduction processes such as photosynthesis, cellular respiration, redox homeostasis and water oxidation (1, 2). Moreover, they hold great promise for applications in biotechnology, e.g., in biosensors and biomolecular electronic devices (3–5). For a full exploitation of their technological potential, however, many challenges still remain. In particular, it would be advantageous to establish reliable and efficient electronic communication under potentiostatic control between the redox-active cofactor and a suitable electrode. Many redox proteins can transfer an electron directly to the electrode, providing favorable conditions for potentiostatic control. Even then, to take full advantage of direct electron transfer, the redox proteins have to be immobilized on the electrode surface with control over their orientation, and without affecting the native conformation and the redox activity.

Under those conditions, the conventional way of monitoring the redox state of the immobilized protein layer is by protein film voltammetry (PFV) (6) which has resulted in significant advancement of our knowledge of the kinetic and thermodynamic nuances of biological electron transfer (6–9). Surface confinement on a carefully engineered or appropriately modified electrode surface removes diffusion limitations in cyclic voltammetry, facilitates direct imaging or spectroscopic analyses, and requires small quantities of material. However, the associated voltammetric responses are typically non-ideal with broad voltammetric peaks and experiment-to-experiment variation. Such observations have been loosely ascribed to kinetic and thermodynamic dispersion across the surface. A range of causes may contribute to this, from lateral molecular interaction and variations in electronic coupling between redox site and electrode, to microenvironmental variances in properties such as surface charge or molecular orientation. A major problem in PFV is the limited control of the orientation of the enzyme, leading to pathway uncertainties and

heterogeneity of the enzyme film. Moreover, the redox cofactors usually lay deeply buried within the protein matrix, rendering electron transfer severely rate limiting.

The objective of the research described in this thesis was to obtain more detailed information on the heterogeneity at the molecular interface between the surface-immobilized redox proteins and the electrode. The work is based on a breakthrough in the detection sensitivity of redox enzyme activity, well beyond what is feasible by amperometric detection: we resorted to optical techniques and fluorescence detection for observing redox proteins and enzymes at work, because of their inherently higher sensitivity.

1.2 The FluRedox principle

Fluorescence detection of redox protein activity, referred to as the FluRedox principle (10, 11), is achieved by making use of a fluorescent label that is covalently attached to the protein of interest. The FluRedox method is based on detection of the redox state of proteins by fluorescence resonance energy transfer (FRET) between this exogenous fluorophore (the donor), and the redox-active site of the protein or enzyme (the acceptor). The acceptor state is an electronic absorption of the active site of the redox protein or enzyme, resonant with the fluorescence of the donor. Thus, changes in the absorbance upon reduction or oxidation of the protein translate in a change of fluorescence intensity of the label (see Figure 1.1).

The fluorescence intensity switches from high to low (or *vice versa*) when a redox event takes place: the fluorescence signals the exchange of electrons with reaction partners or with an electrode. Therefore, we can monitor redox activity by following fluorescence; instead of electrons we monitor photons, *i.e.*, detection is transferred from the amperometric to the optical domain. We can therefore utilize the superior sensitivity and efficiency of optical detectors.

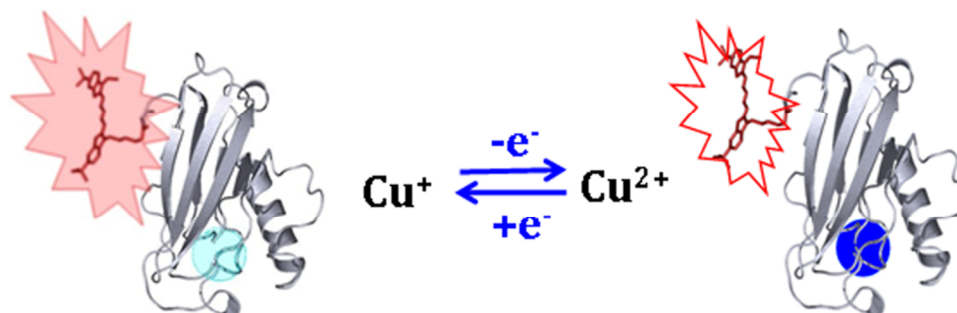


Figure 1.1. FluRedox Principle: Model of Cy5-NHS labeled wt azurin based on the crystal structure of wt azurin by Nar et al. (12) (4AZU.pdb). The copper center is highlighted as a blue sphere. The Cy5 label has been attached to the protein via a covalent (amide) bond to the carboxylate group on the dye molecule. The covalently attached Cy5 is excited at a wavelength close to its extinction maximum, λ_{ex} . In the reduced form of the protein the Cy5 relaxes by the conventional route, with emission of a photon at a characteristic wavelength, λ_{em} . In the oxidized form of the protein a FRET process can occur between the excited Cy5 label and the copper redox center (blue sphere), resulting in loss of fluorescence emission. Thus, the change in the absorbance of the protein can be translated to the fluorescence detection by means of FRET.

Moreover, optical read-out exclusively responds to the redox state of the redox protein or enzyme, which dramatically decreases the chance of spurious contributions to the signal. The FluRedox method can be combined with simultaneous measurement of, for example, absorption or fluorescence of other species in solution, cyclic voltammetry (13–15), and/or fluorescence lifetimes (16, 17). It can be applied to a broad range of proteins and enzymes, establishing a new technology platform (3, 13–21).

Most importantly for the work described in this thesis, the FluRedox method can be applied at the single-molecule level, by which heterogeneity in kinetic and thermodynamic electron transfer parameters can be explored. The method was used to study, both, potentiostatically and chemically induced redox switching of azurin.

1.3 A metalloprotein: Azurin

Wild type (wt) azurin (Figure 1.1) from *Pseudomonas aeruginosa*, an electron-shuttling T1 type metalloprotein with a molecular weight of 14 kDa, is the benchmark protein used in this thesis. It contains one mononuclear copper (Cu) ion which is the redox center in the so-called northern region of the protein buried in a hydrophobic patch at 7 Å distance from the surface. The penta-coordinated Cu center surrounded by its ligands His46, His117, Cys112, Met121 and Gly45 shows a distorted trigonal bipyramidal geometry (12). The geometrical arrangement of ligands around the redox center affects the spectroscopic properties as well as the thermodynamic and kinetic features of azurin (22). Canters and coworkers, for example, rearranged the protein backbone by replacing His117 with glycine thus creating a 'hole' in the azurin coordination sphere. Addition of ligands such as imidazole rescues the T1 Cu center while anionic ligands enhance T2-character (23–25). ET reactions from azurin to its physiological partners occur through the aforementioned hydrophobic patch via a pathway involving His117 (24). Azurin in its oxidized state (Cu²⁺) displays an intense ($\epsilon = 5700 \text{ M}^{-1}\text{cm}^{-1}$) ligand-to-metal-charge-transfer transition in the visible region at ~600 nm, conferring to azurin its blue color (26). The spectroscopic properties of the Cu site are governed mainly by the three strong ligands (His46, His117, Cys112). The ligand configuration around the Cu gives rise to a very small hyperfine coupling of T1 Cu contrary to the normal hyperfine coupling in T2 type proteins (27, 28). The optical absorption essentially disappears when the protein is reduced to Cu⁺.

The physiological partner of azurin has not yet been identified, but azurin may play a role in the oxidative stress response of the microorganism (29). Azurin can exchange electrons *in vitro* with cytochrome c551, nitrite reductase, and several dehydrogenases (30–34). Importantly, azurin, from the pathogenic bacteria *Pseudomonas aeruginosa*, has been reported to selectively induce and trigger apoptosis in human cancer cells, most probably by stabilizing p53 (35,

36). Moreover, azurin can serve as a highly sensitive amperometric biosensor for the detection of superoxide radicals that can be used to understand radical reactions at the cellular level (37).

1.4 Experimental Methods

1.4.1 Electrochemistry

Charge transfer at the electrode-solution interface has been investigated for many decades to elucidate the chemistry of electrode processes and associated reactions. It has resulted in the (still on-going) development of efficient batteries and fuel cells. A common feature of many electrochemical techniques (38) is that they establish a relationship between the applied electrode potential (E), the resulting current (i) flowing through the electrochemical cell, and time (t). Results are amenable to detailed quantitative analyses based on theoretical relationships that are derived from fundamental electrochemical principles and laws. These types of measurements are commonly referred to as voltammetry, and allow us, for example, to probe the thermodynamics and kinetics of redox reactions. Moreover, they can be used for a quantitative determination of chemical substances in solution, which is, for example, very successfully applied in glucose biosensors for monitoring human blood sugar levels.

Manipulation of the interfacial potential difference affords an important way of exerting external control over the electrode reaction. This is typically achieved in a three-electrode configuration (see Figure 1.2A) with a working electrode, a reference electrode and a counter electrode. The working electrode is where the reaction of interest takes place. A potentiostat is used to maintain a well-defined potential difference between the working and the reference electrodes by adjusting and measuring the current that flows between the counter and the working electrodes.

For PFV measurements and fluorescence-detected voltammetry, we used an

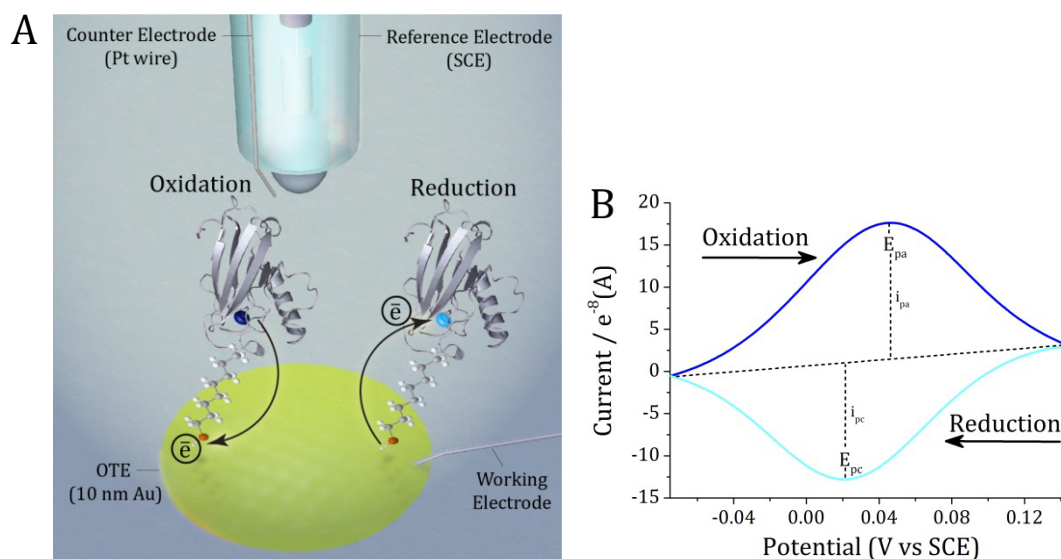


Figure 1.2. (A) Cartoon representation of protein film voltammetry (PFV), where the azurin is adsorbed onto the Au electrode and electron transfer is through the self-assembled monolayer of octanethiol. At a particular electrode potential electrons flow between the metal cofactor and the Au electrode; the current becomes maximal when the electrode potential approaches the midpoint potential of azurin. (B) Typical cyclic voltammogram of a reversible reaction, in this case of wt azurin. It was acquired at a scan rate of 200 mV/s in a positive direction from -0.075 V to $+0.145$ V and back to -0.075 V. The working electrode consisted of a 10 nm thick, homogenous Au film. The reference was a standard calomel electrode (SCE), the counter electrode was a Pt wire, and the supporting electrolyte was 500 mM potassium phosphate at pH 7. E_{pa} and E_{pc} are the potentials where the current (I_{pa} and I_{pc}) reaches a maximum when scanning in the positive or negative direction, respectively.

optically-transparent, homogenous gold layer (~ 10 nm thick) as a working electrode. Figure 1.2A illustrates the basic principle of PFV. Such electrochemical studies can generate important information about intrinsic thermodynamic, kinetic and mechanistic properties of the proteins. Furthermore, structural and binding characteristics and orientation of the redox proteins on different electrode surfaces can also be revealed (Chapter 2 and 3 of this thesis).

Depending on how the potential or the current is manipulated at the working electrode, we can distinguish a large number of different electrochemical techniques, such as amperometry, chronoamperometry, linear sweep voltammetry, and cyclic voltammetry, to name a few. For the experiments

described in this thesis we have specifically used cyclic voltammetry and chronoamperometry in combination with the FluRedox method.

1.4.1.1 Cyclic Voltammetry (CV)

Cyclic voltammetry (CV) is the most widely utilized electrochemical technique (38) that has proven to be highly useful for studies of rather complicated electrode reactions. It is a potential sweep method where the potential is varied periodically at a specific rate, both in the forward and reverse directions, while the current is measured that result from the redox process at the working electrode (the so-called Faradaic current). A wealth of information can be obtained from such a cyclic voltammogram, which can be used to evaluate ET kinetics and thermodynamics, or to obtain diffusion coefficients and follow the course of events regarding absorption/desorption processes at the electrode. A representative cyclic voltammogram (CV) is shown in Figure 1.2B for wt azurin adsorbed on an octanethiol monolayer deposited on a semi-transparent working electrode of gold (10 nm thick). It was acquired at a scan rate of 200 mV/s in a positive direction from -0.075 V to $+0.145$ V and back to -0.075 V. The reference electrode here was a standard calomel electrode (SCE), the counter electrode consisted of a Pt wire, and the solution contained electrolyte in the form of 500 mM phosphate buffer at pH 7.0. When the potential is scanned in a positive direction it reaches a point where the one-electron oxidation of Cu^+ to Cu^{2+} occurs, and current flows between the working electrode and the counter electrode. During the second half of the potential cycle, the reduction of Cu^{2+} to Cu^+ occurs as the electrode potentials are reverted. The parameters of greatest interest for a reversible cyclic voltammogram are the peak cathodic potential (E_{pc}), the peak anodic potential (E_{pa}), the peak cathodic current (i_{pc}), and the peak anodic current (i_{pa}). Specific information about the redox couple can be obtained by calculating the half-wave potential (midway between the anodic and cathodic peak potentials), E_0 , of the voltammetric response:

$$E_0 = \frac{E_{pa} + E_{pc}}{2} \quad (1)$$

At high scan rates the electrode reaction may be kinetically limited, since it depends on mass transport of reactants in solution and on the intrinsic electron transfer rate at the electrode surface. Thus, the current is dependent on the rate of the heterogeneous reaction. Analysis of the current response as a function of the scan rate allows the determination of different kinetic ET parameters for the electrode reactions. Such electrochemical studies can generate important information about intrinsic thermodynamic, kinetic and mechanistic properties of the proteins. Furthermore, structural aspects and binding characteristics of the redox proteins on different electrode surfaces can also be revealed (Chapter 2 and 3 of this thesis).

1.4.1.2 Thermodynamics of biological redox reactions

Redox potentials are used to rationalize the sequence in which electron acceptors are used in mature natural environments and to indicate the oxidation state of the system (39). A fundamental expression for characterizing redox systems under equilibrium conditions is the Nernst equation, given by

$$E = E_0 - \frac{RT}{nF} \ln \frac{[Red]}{[Ox]} \quad (2)$$

The Nernst equation allows the calculation of relative activities of the species in a redox reaction as a function of the measured electrode potential (E) and the standard reduction potential (E_0). Here, F is the Faraday constant ($F = 9.648\,533\,99 \times 10^4 \text{ C mol}^{-1}$), n is the number of transferred electrons ($n = 1$ for azurin) and $[Red]$ and $[Ox]$ are the concentration of the reduced and oxidized form of the redox couple, respectively. Redox potentials in the environment normally range between -300 mV and $+600 \text{ mV}$.

Of special interest for the work in this thesis are mononuclear type I cupredoxins

which contain a single Cu ion with low (0.7 eV) reorganization energies (40, 41). The values of the midpoint potential, E_0 , from various members of this ubiquitous family span about 500 mV range (2, 41, 42). There has been a debate whether the reorganization energy depends mainly on the metal cofactor and its interaction with the surrounding ligands (inner sphere) or whether it is dominated by the protein and solvent rearrangements (outer sphere) (43–45). For instance, electronic properties of the metal-binding site of cupredoxins are particularly depending on the electrostatic field of the protein (46). Molecular dynamic simulations indicate that the inner sphere contribution to the overall reorganization energy is negligible, in contrast to that of solvent rearrangement around the hydrophobic patch and the His117 residue (40).

1.4.1.3 Kinetics of ET in proteins

Copper proteins are involved in a wide range of electron transfer (ET) processes, predominantly in biological energy conversion cycles but also in diverse biochemical transformations such as in metabolism. The availability of the high-resolution three-dimensional (3-D) structures of these proteins has dramatically enhanced our understanding of the electronic and functional properties of copper proteins. Structural information has allowed the analysis of rates and activation parameters of ET processes in relation to their reaction mechanisms according to current theoretical models (22, 47, 48).

A central tenet of ET theory is the Franck-Condon principle, which states that because electrons move much faster than nuclei, the nuclei remain fixed during the actual reaction; therefore, the transition state of the reaction must be in a nuclear-configuration space where the reactant and product states are degenerate (in Figure 1.3, where the two energy curves intersect) (49, 50). Thus, the kinetics of the reaction are dependent on the activation barrier ΔG^\ddagger .

According to Marcus theory, the activation barrier for adiabatic electron transfer reactions depends on the driving force (ΔG^0) and reorganization free energy (λ).

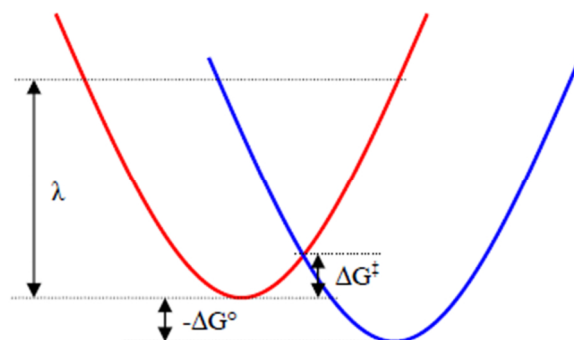


Figure 1.3. Potential energy curves. Representation of reactant (red) and product (blue) potential energy curves, with activation barrier (ΔG^\ddagger), driving force ($-\Delta G^\circ$), and reorganization energy (λ) noted.

The latter comprises inner-sphere (ligand) and outer-sphere (solvent) nuclear rearrangements that accompany ET, which should be small when high ET rates are required (40). ET processes occur over distances well above the van der Waals contact, with the protein matrix providing a non-adiabatic weak donor–acceptor coupling, resulting in an ET mechanism described by the Marcus semi-classical expression (49, 50).

$$k_{ET} = \frac{2\pi}{h} \frac{H_{DA}^2}{\sqrt{4\pi\lambda RT}} e^{-\frac{(\Delta G^0 + \lambda)^2}{4\lambda RT}} \quad (3)$$

This equation shows that the ET rate, k_{ET} , is governed by the driving force of the reaction (ΔG^0), the nuclear reorganisation energy (λ) and the electronic coupling (H_{DA}) between electron donor (D) and acceptor (A) at the transition state.

1.4.2 Introduction to Fluorescence

Absorption of an ultraviolet or visible photon promotes a valence electron from its ground state to an excited state, in most cases with conservation of the electron's spin. Fluorescence occurs when a molecule in the lowest vibrational energy level of an excited electronic state returns to a lower energy electronic state by emitting a photon (51). The photophysical process responsible for the

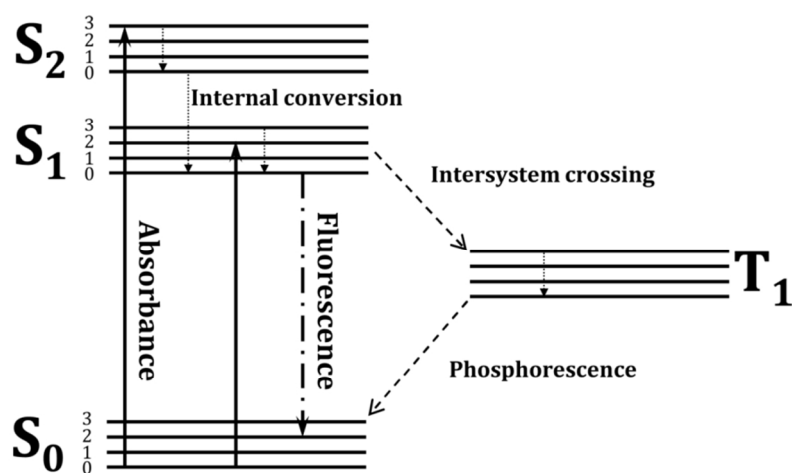


Figure 1.4. Jablonski diagram shows the electronic states of a molecule and the transitions between them. S_0 is the electronic ground state; S_1 and S_2 are the first and second excited electronic states of the molecule. The numbers 0,1,2,3 represent the vibrational states of each electronic state S . T_1 is the triplet state of the molecule. Absorption of a photon of correct energy excites the molecule to one of several vibrational energy levels in the excited state. Fluorescence occurs when a molecule in the lowest vibrational energy level of an excited electronic state returns to a lower energy electronic state by emitting a photon. Dotted arrows represent non-radiative energy dissipation.

fluorescence of fluorescent probes and other fluorophores is illustrated by a simple electronic-state diagram (Jablonski diagram) as shown in Figure 1.4.

The molecule initially occupies a vibrational level associated with the lowest-energy electron configuration, the so-called (singlet) electronic ground state labeled S_0 , which is shown in Figure 1.4. Absorption of a photon of correct energy excites the molecule to one of several vibrational energy levels in the first excited electronic state, S_1 , or the second electronic excited state, S_2 , both of which are singlet states. Relaxation to the ground state from these excited states occurs by a number of mechanisms that are either radiationless, *i.e.* no photons are emitted, or that involve the emission of a photon.

One form of radiationless deactivation is vibrational relaxation, in which a molecule in an excited vibrational energy level loses energy as it moves to a

lower vibrational energy level in the same electronic state. Vibrational relaxation is very rapid, with the molecule's average lifetime in an excited vibrational energy level being 10^{-12} s or less. As a consequence, molecules return quickly to thermal equilibrium of the vibrational population distribution in a given electronic state.

Another form of radiationless relaxation is internal conversion, in which a molecule in the vibrational level of an excited electronic state passes directly into a high vibrational energy level of a lower energy electronic state with conservation of the electron spin. By a combination of internal conversions and vibrational relaxations, a molecule in an excited electronic state may return to the ground electronic state without emitting a photon. A related form of radiationless relaxation is external conversion in which excess energy is transferred to the solvent or another component in the sample matrix.

Another form of radiationless relaxation is intersystem crossing in which a molecule in the vibrational energy level of an excited electronic state passes into a high vibrational energy level of a lower energy electronic energy state with a different spin state. The energy lost to the surroundings, due to vibrational relaxation and internal conversion, is one of the reasons why a Stokes shift is observed.

1.4.3 Fluorescence Resonance Energy Transfer (FRET)

In 1946, Theodor Förster (52) proposed a theory outlining the quantum-mechanical behavior of the transfer of electronic excitation energy between two molecules in close proximity. Förster resonance energy transfer (FRET) can take place when fluorescence emission spectrum of a donor molecule overlaps the absorption spectrum of an acceptor molecule. Quenching of the donor fluorescence results when the electric field of the transition dipole moment of the donor molecule interacts with that of an acceptor molecule at close range.

The efficiency of the non-radiative FRET process (E) depends on the inverse of the sixth power of the distance (r) between the donor and acceptor molecule:

$$E = \frac{R_0^6}{R_0^6 + r^6} \quad (4)$$

The distance at which energy transfer is 50% efficient is referred to as the Förster radius (R_0). Thus, FRET can be used as a *spectroscopic ruler* in the range of 10 – 70 Å by measuring the variations in transfer efficiency. R_0 is dependent on a number of factors, including the fluorescence quantum yield of the donor in the absence of acceptor (Φ_D), the refractive index of the solution (n), the dipole angular orientation of each molecule (κ^2), and the spectral overlap integral of the donor and acceptor ($J(\lambda)$):

$$R_0 = 0.211[\kappa^2 n^{-4} \Phi_D J(\lambda)]^{1/6} \quad (5)$$

Herein, the so-called overlap-integral, $J(\lambda)$ is defined as:

$$J(\lambda) = \frac{\int_0^\infty I_D(\lambda) \varepsilon_A(\lambda) \lambda^4 d\lambda}{\int_0^\infty I_D(\lambda) d\lambda} \quad (6)$$

where $I_D(\lambda)$ is the fluorescence intensity of the donor and $\varepsilon_A(\lambda)$ is the extinction coefficient of the acceptor as a function of the wavelength, λ . FRET is not only a useful tool to quantify molecular dynamics in biophysics and biochemistry, such as protein-protein interactions, protein–DNA interactions, and protein conformational changes. but it also is of great importance in the development of molecular devices and artificial photosynthesis (51, 53–55). FRET techniques and experimental methods have evolved over the years to become an invaluable tool in single molecule research (56–61).

1.4.4 FluRedox Principle applied to azurin

Typical biological and biochemical applications of FRET use the energy transfer

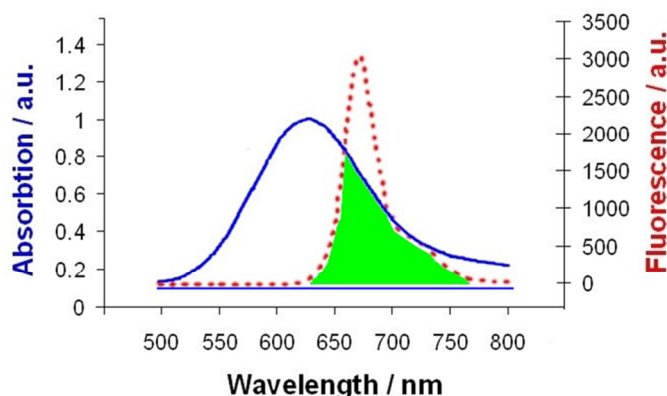


Figure 1.5. Illustration of FluRedox principle. Absorption of oxidized azurin (blue curve), overlaps with emission of Cy5 (red curve). The spectral overlap $J(\lambda)$ is shown in green. The reduced form of azurin does not have an absorbance.

efficiency as a ruler to monitor and measure conformational changes of a biomolecular system. In contrast, the FluRedox principle is based on the change of the overlap integral which is associated with a change in the optical properties of the redox-active center upon oxidation or reduction. This optical read-out responds exclusively to the redox state of the protein, which dramatically decreases the chance of spurious signals from other components in the system.

In this thesis, this FRET-based approach allowed us to monitor the redox-state-dependent change of the absorption spectrum of the metal cofactor in azurin via fluorescence detection: The emission spectrum of a covalently attached fluorescent dye molecule (donor) reflects the changes in metal cofactor (acceptor) absorbance. The FluRedox concept is illustrated in Figure 1.5: In particular, the oxidized form of azurin has a maximum absorbance around 650 nm (blue line) which overlaps with the Cy5 fluorescence emission (red line). The region of spectral overlap, contributing to $J(\lambda)$, is depicted by the green-colored area. The FRET efficiency is high in this case, and the fluorescence of the Cy5 label is strongly quenched. The absorption band is absent when azurin is reduced, and the FRET efficiency is then low. FRET does not only provide increased molecular sensitivity but also selectivity to the point where we can

observe the transfer of electrons one at a time. So far, the FluRedox principle has been successfully applied in biosensor applications (3, 18, 19) and single molecule enzymology (16, 20, 21).

1.5 Single molecule detection techniques in this thesis

1.5.1 Fluorescence-detected electrochemistry

The FluRedox principle can be used to combine electrochemical manipulation of redox proteins with fluorescence detection of their redox state. An artistic representation of fluorescence-detected electrochemistry, together with the FluRedox principle is shown in Figure 1.6. In this thesis, we have used inverted fluorescence microscopes to achieve spatial resolution, either in wide-field mode or in confocal mode (see Figure 1.7).

Wide-field epi-fluorescence detection with electrochemical potential control, so called Fluorescent Cyclic Voltammetry (FCV) (13–15), allowed us to investigate a full monolayer of proteins immobilized on the electrode surface (Chapter 2). To illuminate an area of a few tens of microns in diameter, the laser beam for excitation is focused onto the back-plane aperture of the microscope objective (Figure 1.7, left panel). Fluorescence emission is collected back through the same microscope objective, transmitted through a dichroic beam splitter, and imaged on a sensitive CCD camera (62). Residual laser excitation light is rejected by appropriate long pass filters.

Sample-scanning confocal microscope (SSCM) with electrochemical potential control is useful to monitor the surface confined redox reactions of a low-density sub-monolayer of protein with single molecule resolution (Chapter 3). SSCM offers several advantages over conventional epifluorescence detection, including the ability to control depth of field, elimination or reduction of background information away from the focal plane and the capability to point by point illumination of the sample. The confocal principle in epifluorescence sample scanning

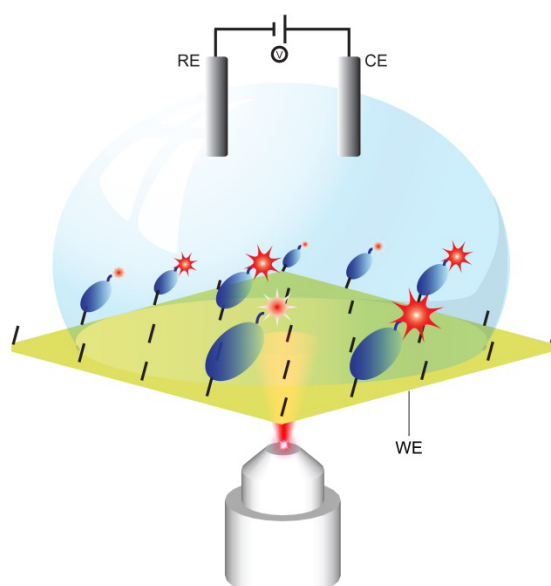


Figure 1.6. An artistic representation of a fluorescence electrochemistry setup. Reference electrode (RE, SCE) and counter electrode (CE, Pt wire) were inserted from top of the confocal objective where the working electrode (WE, 10 nm Au) was used simultaneously as a microscopic slide (optically transparent electrode, OTE). Azurin labeled with Cy5 appropriately attached to the Au electrode through a self-assembly monolayer of octanethiol. According to the FluoRedox principle, when the protein is oxidized FRET occurs between the metal-cofactor and attached fluorophore and results in quenched fluorescence. In the reduced form of protein, only emission of the fluorophore can be seen.

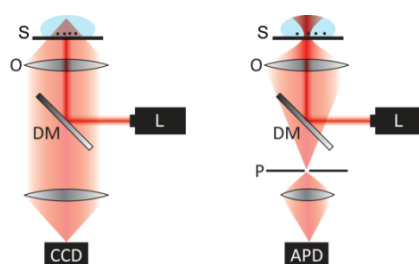


Figure 1.7. Comparison of epi-fluorescence (left) and sample scanning confocal microscopy (SSCM) (right) setups. Both microscope types are using epi-fluorescence excitation of the sample (S) via a dichroic mirror (DM) and an objective lens (O). In epi-fluorescence imaging, a large sample area is imaged onto a CCD, whereas in confocal microscopy the fluorescence of a diffraction limited spot is detected by a point detector like an avalanche-photodiode (APD). With SSCM, the image is reconstructed by scanning the sample with respect to the laser beam while measuring the fluorescence intensity. A better signal-to-background ratio is obtained than in wide-field imaging because of the rejection of out-of-focus light by a pinhole (P).

microscope is illustrated in Figure 1.7 (right panel). Having the same working principle as in the epifluorescence detection, the basic key to the confocal approach is the use of a pinhole to eliminate out-of-focus light arriving from the sample (62, 63).

1.5.2 Chemically-induced SM fluorescence spectroscopy

Another method to manipulate a protein's redox state is by control of the chemical composition of the sample, i.e. by adding reducing or oxidizing reagents (Figure 1.8). The effective redox potential is then given by the Nernst equation, and can be measured directly. Depending on the redox potential, individual redox proteins will switch continuously between the oxidized and the reduced state. Redox-switching can be monitored in real time using the FluRedox principle: fluorescence emission from a suitably labeled, single redox protein is recorded using time-correlated single-photon counting (TCSPC) techniques. TCSPC is based on the time-resolved detection of emitted photons upon excitation by a short flash of light, typically a laser pulse (64). Main applications of TCSPC imaging are fluorescence lifetime measurements (16, 17, 65), fluorescence quenching and FRET (16). The fluorescence lifetime is a direct, quantitative indicator of the FRET rate from the excited molecules to the local environment or to other fluorophores or fluorescence quenchers (51). This also applies to, e.g., fluorescently labeled azurin: the oxidized and reduced state of an individual redox protein or enzyme can be distinguished by the difference in fluorescence lifetime (Chapter 4).

Lifetimes are defined by the average time a fluorophore spends in its excited state. The fluorescence intensity decays of individual molecules were analyzed as the sum of mono-exponential decays:

$$I(t) = \sum_{i=1}^n \alpha_i e^{(-t/\tau_i)} \quad (7)$$

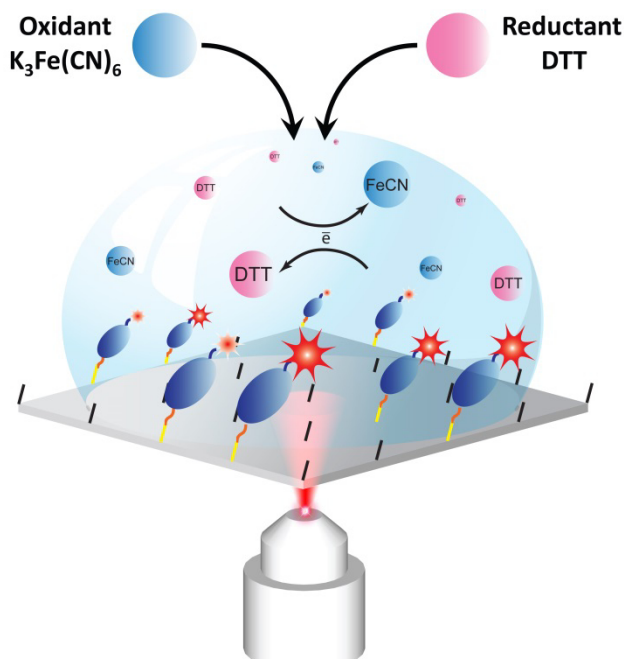


Figure 1.8. Chemically-induced single molecule fluorescence spectroscopy setup. The redox state of the protein on immobilized glass surface was monitored using a mixture of DTT and $K_3(FeCN)_6$ as reductant and oxidant in the buffer solution. The redox potential of the solution was determined with reference electrode (SCE) and counter electrode (platinum wire) connected to a multimeter.

where τ_i are the decay times and α_i are the amplitudes. The values of τ_i and α_i were determined using the PicoQuant SymPho-Time software. The data are fitted with a convolution of the instrument response function (IRF) and exponential decay (66) according to a sum-of-least-squares criterion (67):

$$\chi^2 = \sum_{k=1}^n \frac{1}{\sigma_k^2} [N(t_k) - N_c(t_k)]^2 \quad (8)$$

The goodness-of-fit parameter of χ^2 is the sum of the squared deviations between the measured decay values $N(t_k)$ and the expected decay values $N_c(t_k)$, each divided by squared deviations (σ_k^2) expected for the number of detected photons (51).

1.6 Scope of this thesis

In **Chapter 2**, we report fluorescence-detected cyclic voltammetry (FCV) to investigate kinetic and thermodynamic dispersion within a population of electrode-confined protein molecules. In summary, we have demonstrated that the redox states of appropriately tagged surface immobilized blue copper proteins can be optically sampled down to levels of a few hundred molecules, a sensitivity which is unprecedented for electrochemistry on a macroscopic surface. It is shown that thermodynamic midpoint potential spans tens of millivolts wide within a given population while the standard electron-transfer rate constant by more than a factor of 100.

In **Chapter 3**, we report the results of fluorescence-detected electrochemistry of individual azurin molecules adsorbed on an octanethiol monolayer which is deposited on an optically transparent gold electrode. Heterogeneity of the system can be quantified and related to thermodynamic dispersion. The distribution of optically-determined midpoint potentials of individual azurins gave a maximum value at 45.7 ± 0.5 mV with fwhm of 15 mV (vs SCE).

In **Chapter 4**, we report the results of measurements on single azurin molecules which are labeled with Cy5 and covalently immobilized on glass substrate through a mixture of silanes. The fluorescence intensity of single azurin molecules as a function of time shows an on-off switching behavior which depends on the redox conditions in solution. Using change point analyses of the fluorescence time traces from individual azurin molecules, reaction kinetics and redox parameters were determined as a function of the redox potential.

References

1. Holm RH, Kennepohl P, and Solomon EI. 1996. Structural and Functional Aspects of Metal Sites in Biology. *Chemical reviews* 96(7):2239–2314.
2. Dennison C. 2005. Investigating the structure and function of cupredoxins. *Coordination Chemistry Reviews* 249(24):3025–3054.

3. Strianese M, Zauner G, Tepper AWJW, Bubacco L, Breukink E, Aartsma TJ, Canters GW, and Tabares LC. 2009. A protein-based oxygen biosensor for high-throughput monitoring of cell growth and cell viability. *Analytical biochemistry* 385(2):242–8. Elsevier Inc.
4. Jonkheijm P, Weinrich D, Schröder H, Niemeyer CM, and Waldmann H. 2008. Chemical strategies for generating protein biochips. *Angewandte Chemie (International ed. in English)* 47(50):9618–47.
5. Choi J-W, Oh B-K, Kim YJ, and Min J. 2007. Protein-based biomemory device consisting of the cysteine-modified azurin. *Applied Physics Letters* 91(26):263902.
6. Armstrong FA, Heering HA, and Hirst J. 1997. Reaction of complex metalloproteins studied by protein-film voltammetry. *Chemical Society Reviews* 26(3):169.
7. Wijma HJ, Jeuken LJC, Verbeet MP, Armstrong FA, and Canters GW. 2007. Protein film voltammetry of copper-containing nitrite reductase reveals reversible inactivation. *Journal of the American Chemical Society* 129(27):8557–65. American Chemical Society.
8. Léger C, Elliott SJ, Hoke KR, Jeuken LJC, Jones AK, and Armstrong FA. 2003. Enzyme electrokinetics: using protein film voltammetry to investigate redox enzymes and their mechanisms. *Biochemistry* 42(29):8653–62. American Chemical Society.
9. Jeuken LC, Camba R, Armstrong F a, and Canters GW. 2002. The pH-dependent redox inactivation of amicyanin from *Paracoccus versutus* as studied by rapid protein-film voltammetry. *Journal of biological inorganic chemistry: JBIC: a publication of the Society of Biological Inorganic Chemistry* 7(1-2):94–100.
10. Schmauder R, Alagaratnam S, Chan C, Schmidt T, Canters GW, and Aartsma TJ. 2005. Sensitive detection of the redox state of copper proteins using fluorescence. *Journal of biological inorganic chemistry: JBIC: a publication of the Society of Biological Inorganic Chemistry* 10(6):683–7.
11. Kuznetsova S, Zauner G, Schmauder R, Mayboroda O a, Deelder AM, Aartsma TJ, and Canters GW. 2006. A Förster-resonance-energy transfer-based method for fluorescence detection of the protein redox state. *Analytical biochemistry* 350(1):52–60.
12. Nar H, Messerschmidt A, Huber R, Van de Kamp M, and Canters GW. 1991. Crystal structure analysis of oxidized *Pseudomonas aeruginosa* azurin at pH 5.5 and pH 9.0. A pH-induced conformational transition involves a peptide bond flip. *Journal of Molecular Biology* 221(3):765–72.
13. Salverda JM, Patil A V., Mizzon G, Kuznetsova S, Zauner G, Akkilic N, Canters GW, Davis JJ, Heering HA, and Aartsma TJ. 2010. Fluorescent cyclic voltammetry of immobilized azurin: direct observation of thermodynamic and kinetic heterogeneity. *Angewandte Chemie (International ed. in English)* 49(33):5912–5915.
14. Patil AV and Davis JJ. 2010. Visualizing and tuning thermodynamic dispersion in metalloprotein monolayers. *Journal of the American Chemical Society* 132(47):16938–44.
15. Davis JJ, Burgess H, Zauner G, Kuznetsova S, Salverda J, Aartsma T, and Canters GW. 2006. Monitoring interfacial bioelectrochemistry using a FRET switch. *The journal of physical chemistry. B* 110(41):20649–54.
16. Tabares LC, Kostrz D, Elmalk A, Andreoni A, Dennison C, Aartsma TJ, and Canters GW. 2011. Fluorescence lifetime analysis of nitrite reductase from *Alcaligenes xylosoxidans* at the single-molecule level reveals the enzyme mechanism. *Chemistry A European Journal* 17(43):12015–9.
17. Elmalk AT, Salverda JM, Tabares LC, Canters GW, and Aartsma TJ. 2012. Probing redox proteins on a gold surface by single molecule fluorescence spectroscopy. *The Journal of chemical physics* 136(23):235101.

Introduction

18. Zauner G, Lonardi E, Bubacco L, Aartsma TJ, Canters GW, and Tepper AWJW. 2007. Tryptophan-to-dye fluorescence energy transfer applied to oxygen sensing by using type-3 copper proteins. *Chemistry-A European Journal* 13(25):7085–90.
19. Gustiananda M, Andreoni A, Tabares LC, Tepper AWJW, Fortunato L, Aartsma TJ, and Canters GW. 2012. Sensitive detection of histamine using fluorescently labeled oxido-reductases. *Biosensors & Bioelectronics* 31(1):419–25.
20. Kuznetsova S, Zauner G, Aartsma TJ, Engelkamp H, Hatzakis N, Rowan AE, Nolte RJM, Christianen PCM, and Canters GW. 2008. The enzyme mechanism of nitrite reductase studied at single-molecule level. *Proceedings of the National Academy of Sciences of the United States of America* 105(9):3250–5.
21. Goldsmith RH, Tabares LC, Kostrz D, Dennison C, Aartsma TJ, Canters GW, and Moerner WE. 2011. Redox cycling and kinetic analysis of single molecules of solution-phase nitrite reductase. *Proceedings of the National Academy of Sciences of the United States of America* 108(42):17269–74.
22. Wilson TD, Yu Y, and Lu Y. 2012. Understanding copper-thiolate containing electron transfer centers by incorporation of unnatural amino acids and the CuA center into the type 1 copper protein azurin. *Coordination Chemistry Reviews* 257(1):1–17.
23. Den Blaauwen T and Canters GW. 1993. Creation of type-1 and type-2 copper sites by addition of exogenous ligands to the *Pseudomonas aeruginosa* azurin His117Gly mutant. *Journal of the American Chemical Society* 115(3):1121–1129. American Chemical Society.
24. Jeuken LJC, P Van Vliet, Verbeet MPH, Camba R, McEvoy JP, Armstrong FA and CG. 2000. Role of the surface-exposed and copper-coordinating histidine in blue copper proteins: The electron-transfer and redox-coupled ligand binding properties of His117Gly azurin. *Journal of the American Chemical Society*(11):12186–12194.
25. Alagaratnam S, Meeuwenoord NJ, Navarro JA, Hervás M, De la Rosa MA, Hoffmann M, Einsle O, Ubbink M, and Canters GW. 2011. Probing the reactivity of different forms of azurin by flavin photoreduction. *The FEBS journal* 278(9):1506–21.
26. Solomon E and Hare J. 1980. Spectroscopic studies of stellacyanin, plastocyanin, and azurin. Electronic structure of the blue copper sites. *Journal of the American Chemical Society* 102(1):168–178.
27. Garner DK, Vaughan MD, Hwang HJ, Savelieff MG, Berry SM, Honek JF, and Lu Y. 2006. Reduction potential tuning of the blue copper center in *Pseudomonas aeruginosa* azurin by the axial methionine as probed by unnatural amino acids. *Journal of the American Chemical Society* 128(49):15608–17. American Chemical Society.
28. Yanagisawa S and Dennison C. 2005. Reduction potential tuning at a type 1 copper site does not compromise electron transfer reactivity. *Journal of the American Chemical Society* 127(47):16453–9. American Chemical Society.
29. Vijgenboom E, Busch JE, and Canters GW. 1997. In vivo studies disprove an obligatory role of azurin in denitrification in *Pseudomonas aeruginosa* and show that *azu* expression is under control of *rpoS* and ANR. *Microbiology (Reading, England)* 143 (Pt 9(1 997):2853–63.
30. Van de Kamp M, Silvestrini MC, Brunori M, Van Beeumen J, Hali FC, and Canters GW. 1990. Involvement of the hydrophobic patch of azurin in the electron-transfer reactions with cytochrome C551 and nitrite reductase. *European journal of biochemistry / FEBS* 194(1):109–18.
31. Simon J and Klotz MG. 2012. Diversity and evolution of bioenergetic systems involved in microbial nitrogen compound transformations. *Biochimica et biophysica acta*: Elsevier B.V.

32. Farver O, Brunori M, Cutruzzolà F, Rinaldo S, Wherland S, and Pecht I. 2009. Intramolecular electron transfer in *Pseudomonas aeruginosa* cd(1) nitrite reductase: thermodynamics and kinetics. *Biophysical journal* 96(7):2849–56. Biophysical Society.
33. Tepper AWJW. 2010. Electrical contacting of an assembly of pseudoazurin and nitrite reductase using DNA-directed immobilization. *Journal of the American Chemical Society* 132(18):6550–7.
34. Bizzarri AR. 2011. Steered molecular dynamics simulations of the electron transfer complex between azurin and cytochrome c551. *The journal of physical chemistry. B* 115(5):1211–9.
35. Yang D, Miao X, Ye Z, and Feng J. 2005. Bacterial redox protein azurin induce apoptosis in human osteosarcoma U2OS cells. *Pharmacological Research* 52:413–421.
36. Yamada T, Hiraoka Y, Ikehata M, Kimbara K, Avner BS, Das Gupta TK, and Chakrabarty AM. 2004. Apoptosis or growth arrest: Modulation of tumor suppressor p53's specificity by bacterial redox protein azurin. *Proceedings of the National Academy of Sciences of the United States of America* 101(14):4770–5.
37. Shleev S, Wetterö J, Magnusson K-E, and Ruzgas T. 2006. Electrochemical characterization and application of azurin-modified gold electrodes for detection of superoxide. *Biosensors & bioelectronics* 22(2):213–9.
38. Bard AJ and Faulkner LR. 2000. *Electrochemical Methods: Fundamentals and Applications*. 856. Wiley.
39. Zehnder A and Stumm W. 1988. Geochemistry and biogeochemistry of anaerobic habitats. 1–38.
40. Cascella M, Magistrato A, Tavernelli I, Carloni P, and Rothlisberger U. 2006. Role of protein frame and solvent for the redox properties of azurin from *Pseudomonas aeruginosa*. *Proceedings of the National Academy of Sciences of the United States of America* 103(52):19641–6.
41. Gray HB, Malmström BG, and Williams RJ. 2000. Copper coordination in blue proteins. *Journal of biological inorganic chemistry: JBIC: a publication of the Society of Biological Inorganic Chemistry* 5(5):551–9.
42. Solomon EI, Szilagyi RK, DeBeer George S, and Basumallick L. 2004. Electronic structures of metal sites in proteins and models: contributions to function in blue copper proteins. *Chemical reviews* 104(2):419–58.
43. Warren JJ, Lancaster KM, Richards JH, and Gray HB. 2012. Inner- and outer-sphere metal coordination in blue copper proteins. *Journal of inorganic biochemistry* 115:119–26.
44. Machczynski MC, Gray HB, and Richards JH. 2002. An outer-sphere hydrogen-bond network constrains copper coordination in blue proteins. *Journal of Inorganic Biochemistry* 88(3-4):375–380.
45. Lancaster KM, Sproules S, Palmer JH, Richards JH, and Gray HB. 2010. Outer-sphere effects on reduction potentials of copper sites in proteins: the curious case of high potential type 2 C112D/M121E *Pseudomonas aeruginosa* azurin. *Journal of the American Chemical Society* 132(41):14590–5. American Chemical Society.
46. Olsson MHM, Hong G, and Warshel A. 2003. Frozen density functional free energy simulations of redox proteins: computational studies of the reduction potential of plastocyanin and rusticyanin. *Journal of the American Chemical Society* 125(17):5025–39.
47. Davidson VL. 2000. What controls the rates of interprotein electron-transfer reactions. *Accounts of chemical research* 33(2):87–93.
48. Farver O and Pecht I. 2011. Electron transfer in blue copper proteins. *Coordination Chemistry Reviews* 255(7-8):757–773. Elsevier B.V.

Introduction

49. Marcus R and Sutin N. 1985. Electron transfers in chemistry and biology. *Biochimica et biophysica acta* 811:265–322.
50. Marcus RA. 1993. Electron Transfer Reactions in Chemistry: Theory and Experiment (Nobel Lecture). *Angewandte Chemie International Edition in English* 32(8):1111–1121.
51. Lakowicz JR. 2006. *Principles of Fluorescence Spectroscopy*. 980. Springer.
52. Forster T. 1946. Energiewanderung und Fluoreszenz. *Die Naturwissenschaften* 33(6):166–175.
53. Selvin PR. 2000. The renaissance of fluorescence resonance energy transfer. *Nature structural biology* 7(9):730–4.
54. Parsons M, Vojnovic B, and Ameer-Beg S. 2004. Imaging protein-protein interactions in cell motility using fluorescence resonance energy transfer (FRET). *Biochemical Society transactions* 32(Pt3):431–3.
55. Willard DM, Carillo LL, Jung J, and Van Orden A. 2001. CdSe–ZnS Quantum Dots as Resonance Energy Transfer Donors in a Model Protein–Protein Binding Assay. *Nano Letters* 1(9):469–474. American Chemical Society.
56. Roy R, Hohng S, and Ha T. 2008. A practical guide to single-molecule FRET. *Nature Methods* 5(6):507–516.
57. Di Fiori N and Meller A. 2010. The Effect of dye-dye interactions on the spatial resolution of single-molecule FRET measurements in nucleic acids. *Biophysical journal* 98(10):2265–72. Biophysical Society.
58. Stein IH, Steinhauer C, and Tinnefeld P. 2011. Single-molecule four-color FRET visualizes energy-transfer paths on DNA origami. *Journal of the American Chemical Society* 133(12):4193–5.
59. Goldsmith RH and Moerner WE. 2010. Watching conformational- and photo-dynamics of single fluorescent proteins in solution. *Nature chemistry* 2(3):179–86. Nature Publishing Group.
60. Roeffaers MBJ, De Cremer G, Uji-i H, Muls B, Sels BF, Jacobs P a, De Schryver FC, De Vos DE, and Hofkens J. 2007. Single-molecule fluorescence spectroscopy in (bio)catalysis. *Proceedings of the National Academy of Sciences of the United States of America* 104(31):12603–9.
61. Blank K, De Cremer G, and Hofkens J. 2009. Fluorescence-based analysis of enzymes at the single-molecule level. *Biotechnology journal* 4(4):465–79.
62. Pawley J. 2006. *Handbook of Biological Confocal Microscopy*. 1016. Springer.
63. Mueller M. 2005. *Introduction to Confocal Fluorescence Microscopy, Second Edition (SPIE Tutorial Texts in Optical Engineering Vol. TT69)*. 138. SPIE Publications.
64. Becker W, Bergmann A, Hink MA, König K, Benndorf K, and Biskup C. 2004. Fluorescence lifetime imaging by time-correlated single-photon counting. *Microscopy research and technique* 63(1):58–66.
65. Tinnefeld P and Buschmann, V Dirk-Peter Herten, Kyung-Tae Han SM. 2000. Confocal fluorescence lifetime imaging microscopy (FLIM) at the single molecule level. *Single Molecules* 1:215–223.
66. Ford G and Weber W. 1984. Electromagnetic interactions of molecules with metal surfaces. *Physics Reports* 113(4):195–287.
67. Ray K, Zhang J, and Lakowicz J. 2008. Fluorescence lifetime correlation spectroscopic study of fluorophore-labeled silver nanoparticles. *Analytical chemistry* 80(19):7313–7318.

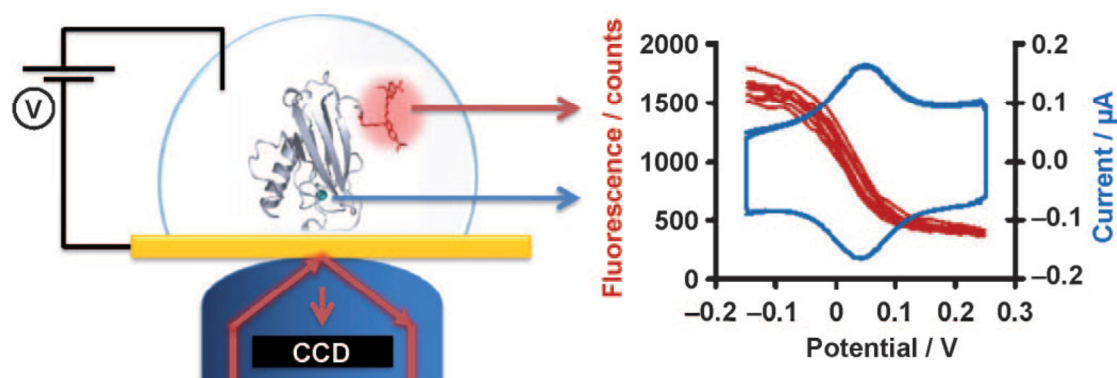
Chapter 2

Fluorescent Cyclic Voltammetry of Immobilized Azurin: Direct Observation of Thermodynamic and Kinetic Heterogeneity[#]

[#] Salverda JM, Patil A V., Mizzon G, Kuznetsova S, Zauner G, Akkilic N, Canters GW, Davis JJ, Heering HA, and Aartsma TJ. 2010. Fluorescent cyclic voltammetry of immobilized azurin: direct observation of thermodynamic and kinetic heterogeneity. *Angewandte Chemie (International ed.)* 49(33):5912–5915.

Abstract

We report on the direct resolution of dispersion in formal electrochemical potential (E_0) and electron transfer rate (k_0) of the blue copper protein azurin. Using a new method, fluorescent cyclic voltammetry (FCV), we could resolve the properties of 100-1000 proteins. On this scale, we have established the presence of large dispersion in both E_0 and k_0 , and we can differentiate between several forms of heterogeneity.



2.1 Introduction

The electrochemical analysis of surface-confined metalloproteins has resulted in a significant advance in our knowledge of the kinetic and thermodynamic nuances of biological electron transfer (1). Surface confinement on a carefully engineered or appropriately modified electrode surface removes diffusion limitations in cyclic voltammetry, facilitates direct imaging or spectroscopic analyses, and requires small quantities of material. However, the associated voltammetric responses are typically nonideal, with broad voltammetric peaks and experiment-to-experiment variation (2, 3). Such observations have been loosely ascribed to kinetic and thermodynamic dispersion across the surface (4–9). A range of causes may contribute to this variation, from lateral molecular interaction, variation in redox-site/electrode electronic coupling, to microenvironmental variance in properties such as surface charge or molecular orientation.

This dispersion can be studied by taking advantage of the enhanced sensitivity of a newly developed method for monitoring redox-state transitions by fluorescence detection (10–14). Herein, we have used azurin, a well-characterized 14 kDa large protein from *P. aeruginosa* with a single Cu-ion as the redox-active center (see Figure A.2.1 in the Appendix) (15–23). In its oxidized (Cu^{2+}) form, the protein displays a strong absorption at 630 nm, which is absent in the reduced state. This redox-dependent absorbance change can be monitored in the fluorescence domain by means of a Förster resonance energy transfer (FRET) donor–acceptor pair, whereby the redox site is the energy acceptor and an externally linked dye label is the fluorescent donor.

2.2 Results and Discussion

We applied fluorescence-detected cyclic voltammetry (FCV) to investigate both a full monolayer of protein (using epifluorescence detection) and a dilute sub-

monolayer (using total internal reflection-excited fluorescence; TIRF). Figure 2.1 shows the conventional cyclic voltammogram and the simultaneously recorded FCV of Cy5-labeled wild-type (wt) azurin adsorbed on gold covered with a hexanethiol self-assembled monolayer (SAM), using epifluorescent detection, at a scan rate of 100 mVs^{-1} . Both signals have the shape expected for an immobilized protein at slow voltage scan rate (see sections 2.4.1–2.4.3 in the Appendix for details). A control analysis with Cy5-labeled redox-inactive Zn-azurin (see Appendix, section 2.4.4) confirmed that the fluorescence switching of labeled Cu-azurin is due to the redox transition.

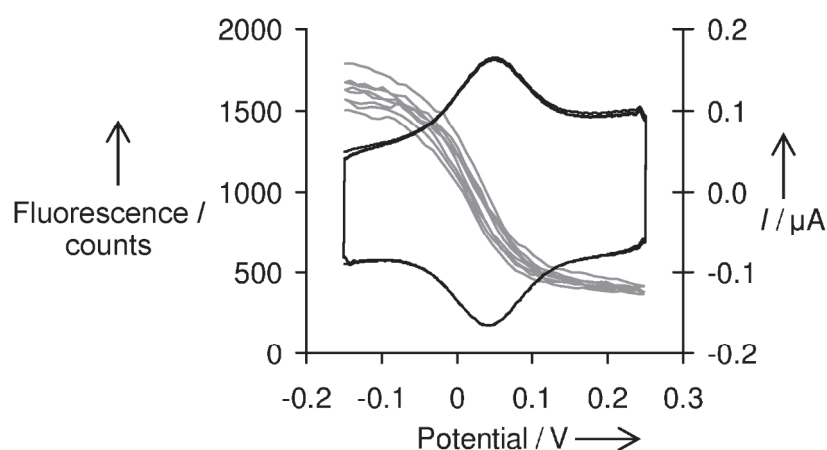


Figure 2.1. Cyclic voltammogram (black) and successive epifluorescent cyclic voltammograms (gray) of Cy5-labeled wt azurin at 100 mVs^{-1} scan rate (4 cycles). The fluorescence change in FCV reflects the change in redox state of the labeled azurin.

FCVs measured at three different scan rates (Figure 2.2) show that the separation between oxidizing and reducing curves increases with scan rate, which is the same behavior as that for the peak separation in cyclic voltammetry (CV) experiments. The data points in these FCV curves were fitted by Butler–Volmer analysis (sections 2.4.5 – 2.4.7 in the Appendix, adapted from Heering et al (24)).

From the scan-rate dependence of both CV and FCV, values for the midpoint potential E_0 , electron-transfer rate constant k_0 , and unusual quasi-reversibility UQR (25) were thus obtained (section 2.4.5 in the Appendix; Table A.2.1).

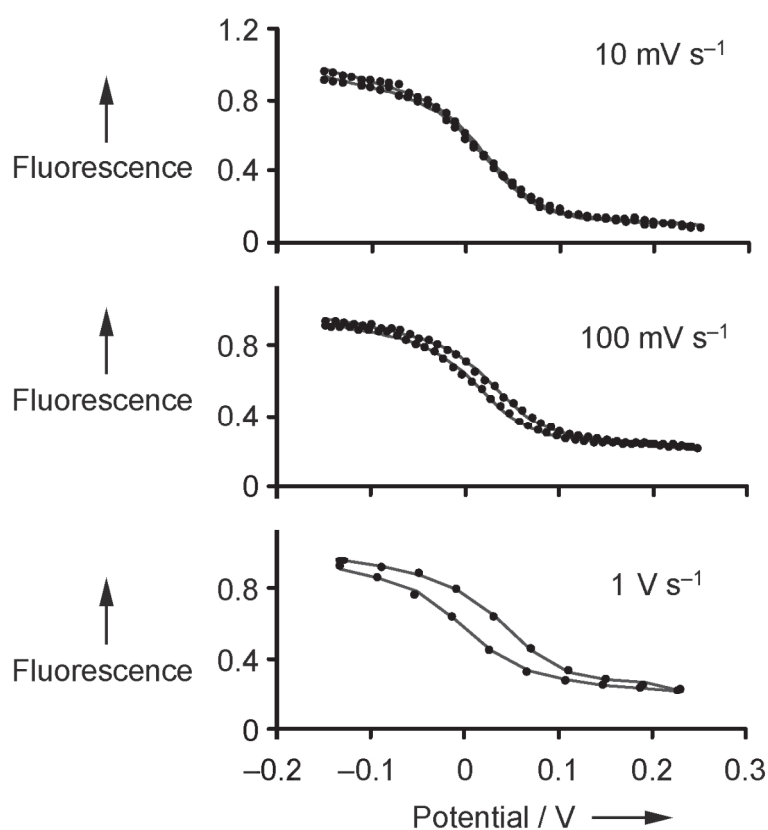


Figure 2.2. FCV curves measured at 10 mVs⁻¹, 100 mVs⁻¹, and 1 Vs⁻¹ showing scan-rate dependence.

The kinetics of electron transfer determined by FCV are in reasonable agreement with those determined by CV (20–22). The observed differences in k_0 values can be explained by the presence of heterogeneity in the electron-transfer rate. Owing to the bias of fluorescence detection towards proteins that are more weakly electronically coupled to the electrode (where fluorescence emission is less quenched), such heterogeneity results in a lower average rate in the optical sampling relative to the purely voltammetric results.

Heterogeneity is evident in the variance in fluorescence intensity across the surface (Figure 2.3a), which is typical for monolayer coverage. At low coverage, this variance is even more pronounced (section 2.4.2 in the Appendix). In Figure 2.3b, three FCV cycles of diffraction-limited spots (region-of-interest, or ROI, size ≈ 300 nm) show a large dispersion in the separation between the reducing and oxidizing curves, which is an observation diagnostic of a large dispersion in interfacial electron-transfer kinetics.

Table 2.1. Fit parameters E_0 , k_0 , and UQR for CV and FCV.

Dataset	E_0 [mV] [a]	k_0 [s ⁻¹] [b]	UQR [c]
CV	44	67	9.7 (1.0)
FCV	28	21	9.7(fixed)

[a] Midpoint potential vs. SCE. [b] Standard electron-transfer rate constant. [c] Unusual quasi reversibility.

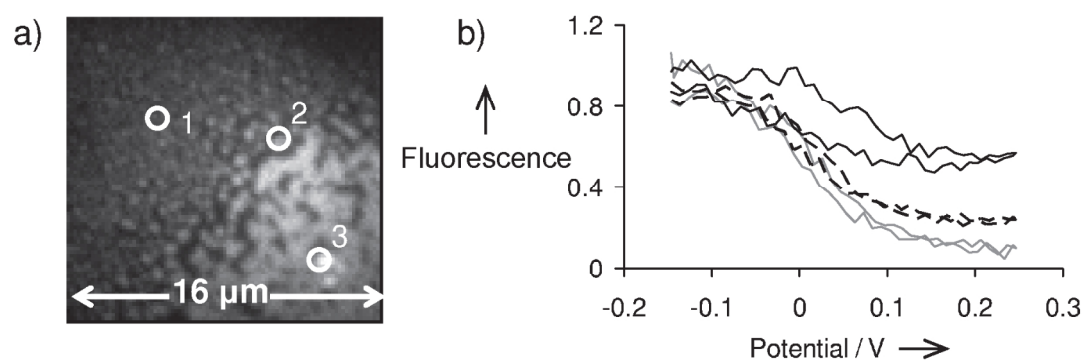


Figure 2.3. a) Image from the epifluorescence movie measured at 200 mVs⁻¹ scan rate on wt azurin at monolayer coverage. b) Epifluorescent voltammograms for three ROIs of 1.5 pixel radius, selected from the image in (a): ROI 1 = gray line, ROI 2 = black dashed line, ROI 3 = black line.

We quantified the kinetic and thermodynamic dispersion by constructing FCV cycles for over 200 such diffraction limited ROIs at a range of scan rates. A ROI contains 500–3000 and 100–450 fluorescently labeled proteins for high coverage and low-coverage samples, respectively (calculations in section 2.4.8 of

the Appendix), which demonstrates an unprecedented molecular-scale electrochemical analysis. The results of fitting all ROI FCV cycles with Butler-Volmer curves are summarized in the histograms in Figure 2.4a-d (see also sections 2.4.5 and 2.4.6 in the Appendix).

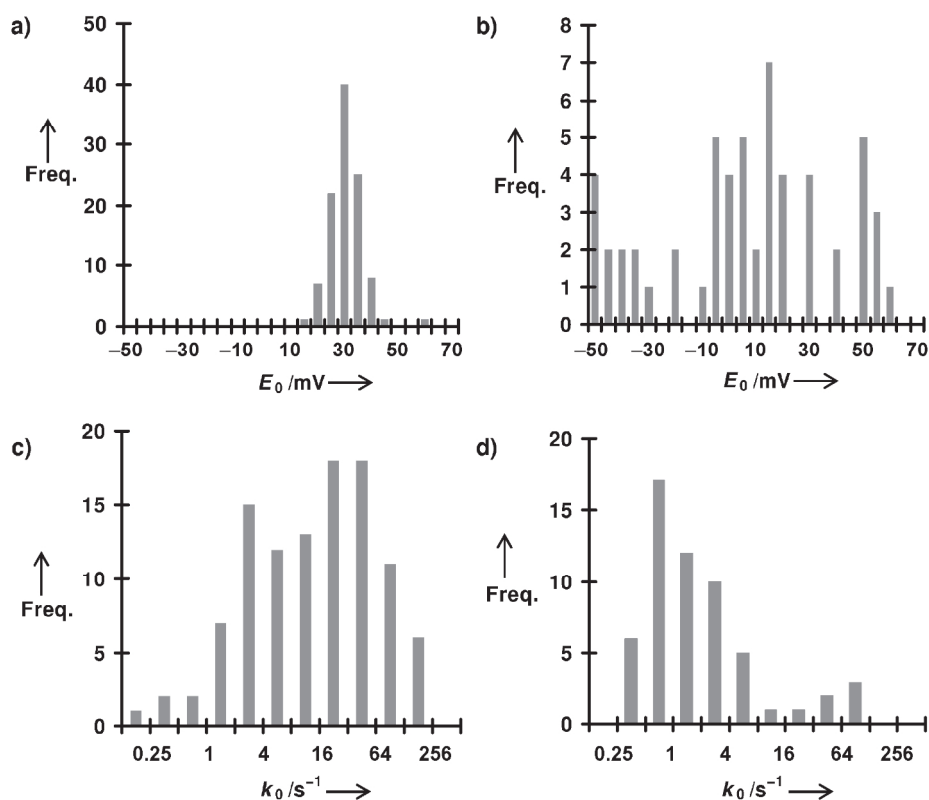


Figure 2.4. a) Histogram of midpoint potential values $E_0 = (E_{p,ox} + E_{p,red})/2$ obtained from all epifluorescence ROI FCV curves showing a 14 mV spread (FWHM) around an average of 28 mV. Bin values on the x axis refer to the upper limit of the bin range for all histograms shown. b) Histogram of midpoint potential values E_0 obtained from all TIRF ROI FCV curves showing a 70 mV spread (FWHM) around an average of 16 mV. c) Histogram of standard electron-transfer rate constants k_0 obtained from all epifluorescence ROI FCV curves showing values ranging from 0.1 s^{-1} to 200 s^{-1} . d) Histogram of standard electron-transfer rate constants k_0 obtained from all TIRF ROI FCV curves showing values clustering between 0.5 and 2 s^{-1} with a high- k_0 tail up to 100 s^{-1} .

The dispersions of E_0 and k_0 values are different for high and low protein coverage. In the former, we find a small spread in E_0 values (Figure 2.4a), which is dominated by noise (see section 2.4.9 in the Appendix), whereas significant

dispersion is evident in the low-coverage data. The k_0 distributions show a high dispersion in both datasets (Figure 2.4c,d), but there is a qualitative difference between them. The low-coverage distribution is more asymmetric and contains a larger contribution from low electron-transfer rates (which is consistent with a data bias towards weakly coupled proteins).

The large k_0 dispersion at low coverage may be due to variation in the orientation of the protein with respect to the surface as well as to microscopic variation in the Au surface properties (local surface charges etc., that is, “microenvironmental variance” (5)). At these coverages, AFM and confocal analyses are consistent with significant molecular aggregation (data not shown). We propose that the analyzed kinetic distribution becomes biased towards faster k_0 values as surface coverage and film order increases (and there is a reduced weighting of the contribution from the aggregated forms, where k_0 is likely to be lower; Figure 2.4c,d).

As for E_0 , at low coverage, the microenvironmental variance will strongly affect the midpoint potential and therefore the observed dispersion in E_0 values. At high molecular coverage, the effect of microenvironmental variance will be damped by sampling more molecules per ROI.

It is of interest to compare the present results with what is known from bulk measurements on electron transfer (ET) within protein–protein complexes and on ET between proteins and SAM-coated electrodes. As for the thermodynamics of the ET process, it is known that protein–protein or protein–electrode interactions can lead to significant modulation in the expressed half-wave potential within a range of 100 mV (26–29). Haehnel and co-workers (29) have, for example, convincingly argued that the electric field exerted by a protein at the site of the redox-active cofactor of the partner protein may account for the observed variations in the midpoint potential.

Immobilization of a protein on a SAM-covered Au electrode may lead to changes of the same order of magnitude. Murgida and Hildebrandt (30) have shown that the electric field at the boundary between solvent and SAM may be in the order of 10–100 mVÅ⁻¹ and may lead to similar changes in the midpoint potential of a redox protein that becomes immobilized on the SAM. In addition, the dielectric constant of the ET medium may be affected by the expulsion of water from the interface, and this may also influence the value of E_0 (29–31). The dispersion in the values of E_0 that we observe for the low-coverage data has a similar range (70 mV full width at half maximum; FWHM) as the mentioned values (29, 30). This result is ascribed to variations in the electric field that result from discontinuities or imperfections in the SAM or the underlying Au surface.

The kinetics of ET are strikingly similar between protein–protein and protein/Au–SAM data. It has been argued that ET within productive protein ET complexes occurs in the Marcus non-adiabatic limit and requires the formation of a specific complex (32–34). The encounter complex between two proteins, however, may require mutual reorientation of the partners to reach the ET-competent configuration. Depending on the details of the protein surfaces and the protein–protein energy landscape (35–37), this step may become rate limiting (30, 32–34).

The rate of electron transfer between an ET protein and a SAM-coated Au electrode has been investigated as a function of the SAM thickness. At large distances, the non-adiabatic regime applies with an exponential $-(\beta R)$ distance dependence for the ET rate. At shorter distances, the rate becomes independent of SAM thickness (20, 22, 38–41), either because the adiabatic limit now applies and the ET becomes friction controlled or because the protein has to reorient to reach an alignment with respect to the Au–SAM surface that is conducive for ET to or from the electrode (30, 42).

From studies on azurin and cytochrome *c* immobilized on a Au/hexanethiol SAM, the ET was found to be gated by protein reorientation (22, 43). In our

experiments, we found that from one ROI to another there is appreciable variation in the value of k_0 . This variation most likely reflects inhomogeneity of the tunneling barrier as a result of orientational flexibility. This must depend on parameters other than the electric field variation, which is responsible for the variation in E_0 , since its value is averaged out at higher coverage. It is conceivable that differences in solvation and also in (local) coverage and orientation-dependent lateral protein–protein interactions are critical in this respect.

In summary, we have demonstrated that the redox states of appropriately tagged surface immobilized blue copper proteins can be optically sampled down to levels of a few hundred molecules, a sensitivity which is unprecedented for electrochemistry on a macroscopic surface. The thermodynamic midpoint potential was found to vary by tens of millivolts across the electrode surface, and the standard electron-transfer rate constant by more than a factor of 100. Furthermore, evidence for different types of heterogeneity was obtained by comparing high- and low-coverage data. To the best of our knowledge, the analysis herein constitutes the first direct observation of both kinetic and thermodynamic dispersion in a protein film on an electrode surface at a molecular scale of sampling.

2.3 Experimental Section

2.3.1. Sample preparation: Preparation and purification of wild-type and N42C azurin were carried out as previously described (44). Wild-type (wt) azurin and zinc-reconstituted wt azurin were labeled on the N terminus as described by Kuznetsova et al (12). The labeling ratio was 0.16. N42C azurin was prepared similarly (see section 2.4.10 in the Appendix). The labeling ratio for the N42C sample used was 0.55.

2.3.2. Sample immobilization and electrode preparation: The working electrode consisted of a semitransparent gold layer of 10 nm thickness deposited on a glass coverslip [1 inch (25.4 mm) diameter, thickness 0.14–0.17 mm (#1), Menzel]. Thin gold films were prepared either by RF sputtering (ATC 1800F, AJA International) or evaporation (Edward Auto 306 cryo evaporator). Sputtering was performed as described by van Baarle et al (45). Azurin was immobilized on the working electrode through a self-assembling monolayer (SAM) of 1-hexanethiol (wt azurin) or 1-octanethiol (zinc azurin and N42C). For more details see section 2.4.11 in the Appendix.

2.3.3. Fluorescent electrochemistry setup: Measurements on wt azurin were performed with a wide-field epifluorescence microscopy setup (Zeiss Axiovert 200, Plan Apo 100X oil). A total internal reflection fluorescence (TIRF) setup (Nikon 2000-E, TIRF 100x Plan Apo oil) was used to perform FCV of immobilized N42C azurin at a surface coverage below the classical CV detection limit. Cy5 excitation was provided by a red diode laser (639 nm, Power Technology Inc., IQ1A30) for epifluorescence and by a HeNe laser (Model 1135, 20 mW, 633 nm, JD Uniphase) for TIRF. Fluorescence was detected with a Peltier-cooled CCD camera (Cascade 512 X, Roper Scientific) or a back illuminated iCCD camera (iXon 885 EMCCD, Andor, Belfast, Northern Ireland), respectively. In both cases, fluorescence was measured in a series of images (a “movie”) at fixed potential intervals (more details and a setup scheme in section 2.4.12 of the Appendix).

2.3.4. Electrochemistry: A copper wire connected the working electrode to a potentiostat (CH Instruments, model Chi832b, for epifluorescence, μ -Autolab, Eco Chemie, for TIRF). A Pt wire or Pt gauze counter electrode and saturated calomel (SCE) reference electrode (Radiometer Analytical/BASI) were inserted into a buffer droplet of approximately 100 μ L on top of the immobilized protein film. CV scans were measured at rates of 10 mVs^{-1} to 10 Vs^{-1} , in potential steps of 1 mV. CV scanning was combined with epifluorescence detection up to 1 Vs^{-1}

scan rate. TIRF FCV was measured at scan rates between 25 mVs⁻¹ and 600 mVs⁻¹.

2.4 Appendix

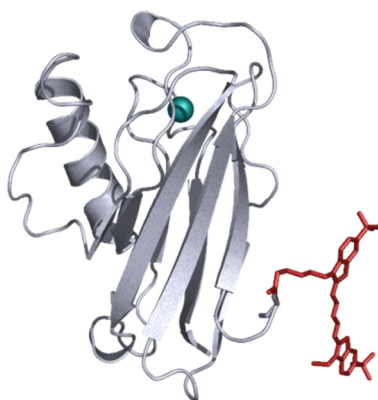


Figure A.2.1. Model of Cy5 labeled wt azurin based on the crystal structure of wt azurin by Nar et al. [1] (4AZU.pdb). The label has been attached to the protein at the N-terminus via a covalent (amide) bond to the carboxylate group on the dye molecule.

2.4.1. Cyclic and fluorescent voltammetry. The cyclic voltammogram in Figure 2.1 has the shape expected for an immobilized protein (17) at slow voltage scan rate, with the reductive and oxidative peaks at nearly the same potential (within 10 mV). The midpoint potential is 45 ± 5 mV vs. SCE, in agreement with literature values at this pH (46–49). The FCV (grey line) in Figure 2.1 is as expected for a signal that reflects the conversion from reduced to oxidized protein. The fluorescence decrease with increasing potential has a sigmoidal shape, with the fastest change in the 0–50 mV range, i.e. around the midpoint potential of azurin as determined by conventional CV. At potentials well above the midpoint (above about 100 mV), the fluorescence is low, and at low potential (< -50 mV) it is high, in agreement with expectations for FRET-based detection of the azurin redox state. The full transition width is about 150 mV, very similar to the full width of the corresponding CV peak.

2.4.2. Fluorescence time traces and switching ratio. From each image of an epifluorescence movie, the average intensity over all pixels was calculated so that a full-image time trace of the intensity and potential could be constructed. TIRF imaging analyses were carried out on sub-monolayer protein films where emission was typically observed in widely separated fluorescent features, see Figure A.2.2, therefore full-image analysis was not performed. A time trace of the fluorescence corresponding to the CV and FCV in Figure 2.1 is shown in Figure A.2.3a (100 mV/s scan rate). An equivalent bleaching corrected TIRF time trace of a single cluster of proteins, i.e. of a Region of Interest (ROI), (scan rate 100 mV/s) is shown in Figure A.2.3b.

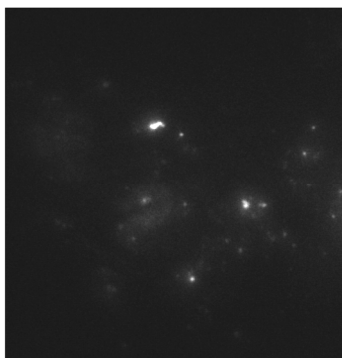


Figure A.2.2. N42C azurin TIRF fluorescence image (345×355 pixels). N42C was immobilized on gold with an octanethiol SAM (100 mM phosphate buffer, pH 7, room temperature).

From the maxima I_{max} and minima I_{min} of the epifluorescence traces we calculate the switching (or quenching) ratio SR , defined (10, 50) as

$$SR = (I_{max} - I_{min})/I_{max}, \quad (A1)$$

and find a scan-rate averaged value of 75%. This agrees well with the value of 80% we have reported previously for chemically induced solution phase redox switching of this labeled protein (12). We have demonstrated the consistency of this value with the dipolar coupling expected between the appended dye and the copper center in earlier work (17, 23). Noticeable variation (about 20%) in SR

across the surface is observed when comparing data taken from different surface areas (not shown).

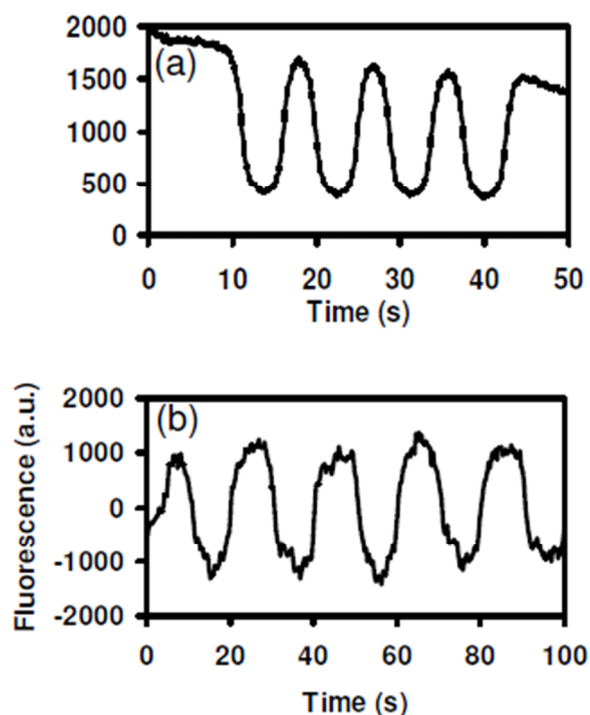


Figure A.2.3. a) WT azurin epifluorescence as a function of time for 100 mV/s scan rate, showing fluorescence switching. Azurin was immobilized on gold with a hexanethiol SAM (500 mM phosphate buffer, pH 7.0, room temperature, sample size $\sim 2 \times 10^6$ fluorescent proteins). b) N42C azurin TIRF fluorescence (after bleaching correction) as a function of time for 100 mV/s scan rate, showing fluorescence switching. The shown trace was taken over a ROI of 8×8 pixels (or 4 times the diffraction limit) in size containing $4 (\pm 2) \times 10^3$ fluorescent molecules. N42C was immobilized on gold with an octanethiol SAM (100 mM phosphate buffer, pH 7.1, room temperature).

2.4.3. Fluorescent cyclic voltammograms and scan rate dependence. In Figure A.2.4, FCVs for all the measured scan rates from 10 mV/s to 1 V/s are shown. A TIRF ROI FCV for 100 mV/s scan rate is shown in Figure A.2.5. To reduce noise as much as possible, TIRF data were averaged over multiple cycles (4 to 10 depending on the particular dataset).

In conventional CV, the peak separation between forward (red \rightarrow ox) and backward (ox \rightarrow red) scans is known to depend on the voltage scan rate. At low

scan rates the peaks (almost) coincide, whereas at higher scan rates the electron transfer between protein and electrode can no longer keep up with the potential change and the peaks start to separate (51, 52). Equivalently, the forward and backward FCV curves are on top of each other for low scan rates and start to separate at higher scan speeds (see Figure A.2.4). In both CV and FCV the increase of peak separation starts above 100 mV/s scan rate and reaches the value of 40 mV at 1V/s. Peak heights in CV scale linearly with the scan rate as expected for an immobilized protein.

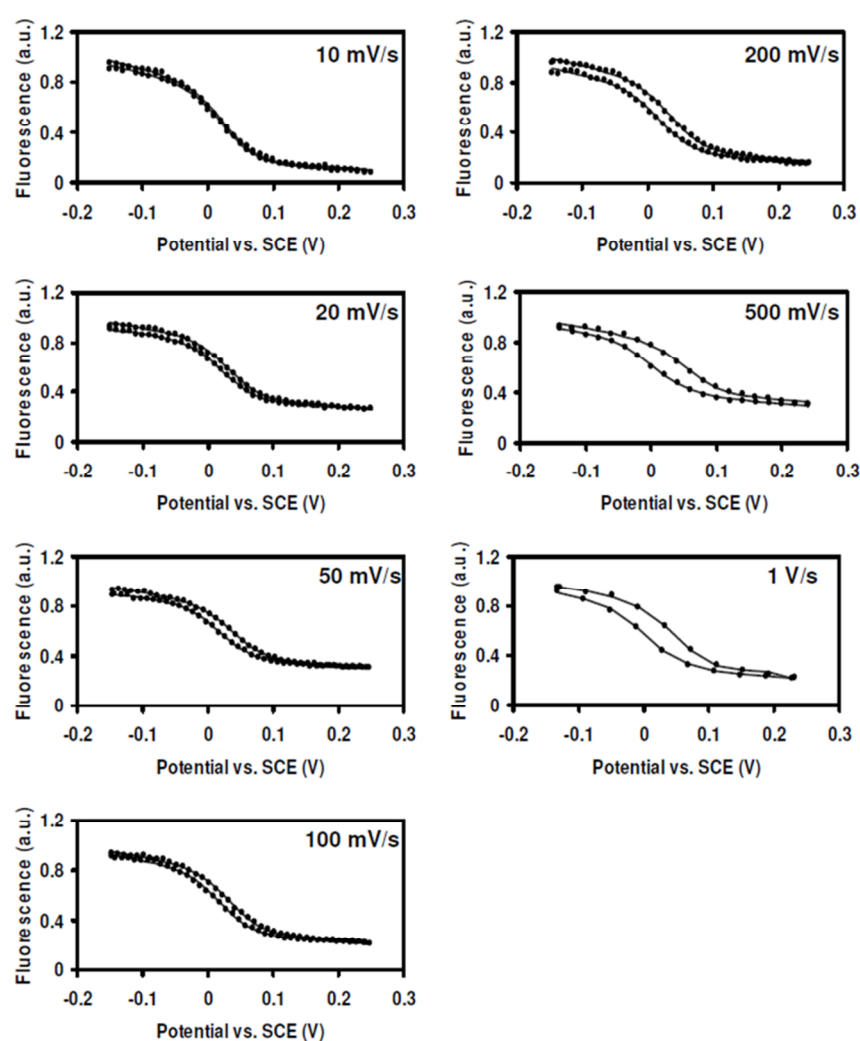


Figure A.2.4. Epifluorescent voltammograms (dots) of WT azurin for all measured scan rates 10, 20, 50, 100, 200, 500 and 1000 mV/s together with Butler-Volmer theory based simulations (lines).

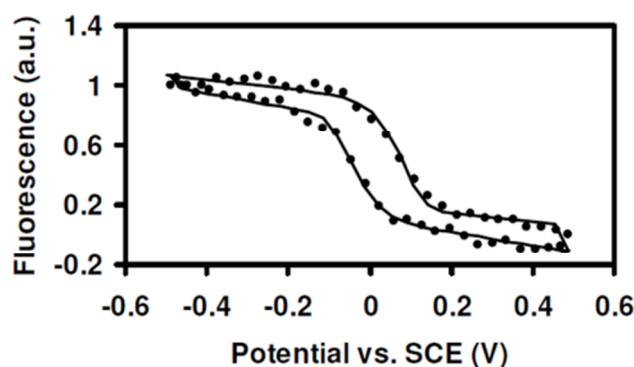


Figure A.2.5. TIRF voltammogram (solid circles) of N42C azurin for 100 mV/s scan rate measured in 100 mM phosphate buffer, pH 7.1, room temperature, together with Butler-Volmer theory based fit (grey lines). This FCV was taken from the same 8×8 pixel ROI as the trace in Figure A.2.3b (sample size $2\text{--}6 \times 10^3$ proteins). Four potential cycles were binned using the original step interval of 69 mV as bin size.

2.4.4. Non FRET coupled emission changes. In control analyses with a Cy5 labeled non redox active Zn azurin fluorescence emission is observed to show a small modulation with surface potential of $< 20\%$ of the total signal amplitude, compared to 75% with the Cu form (Figure A.2.6). This is observed to disappear at high scan rates (above 200 mV/s) and is also reduced at higher ionic strength.

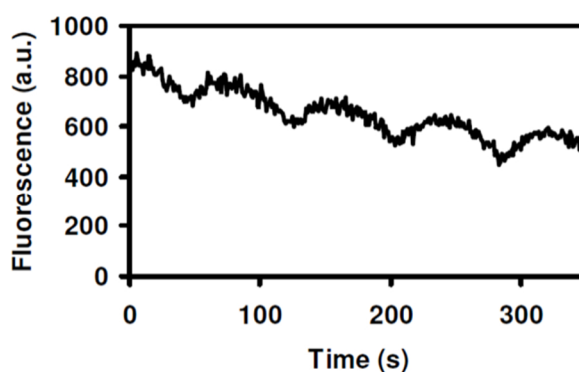


Figure A.2.6. Zinc azurin epifluorescence time trace for 10 mV/s scan rate. Zinc azurin was immobilized on gold with an octanethiol SAM (500 mM phosphate buffer, pH 7, room temperature).

This non-redox effect is conceivably associated with surface-potential-induced changes in protein fold or orientation on the surface. In a labeled protein such changes may be expected to influence the efficacy of nonradiative energy

transfer between the fluorophore and underlying gold surface (53–56). The effects of high ionic strength are fully consistent with these being double layer (electric field) in origin. It is highly likely that the same non-redox related potential modulations in fluorescence emission occur with the redox active Cu protein, and a small change of the signal with potential is indeed observed in the FCV curves outside of the redox transition region superposed on the redox transition sigmoid (see Figure 2.1, Figures A.2.4 and A.2.5: a negative slope is seen at both sweep ends, where the protein is either fully reduced or fully oxidized). In the quantitative analysis of the data (Section 2.4.6) a correction term for this ‘field effect’ is included.

2.4.5. Analyzing the cyclic voltammetry data with Butler-Volmer theory. CV peak potentials were determined by fitting a Gaussian peak profile (standard CHI software option) to raw data. The associated midpoint potentials E_0 , and peak separations ΔE are given in Table A.2.1. In Figure A.2.7 (open squares), the CV peak separation increases with scan rate as expected. Note that the peak separation is constant at low scan rates (<100 mV/s) but not zero. This residual midpoint separation is due to “unusual quasi-reversibility” (*UQR*) as described first by Feldberg and Rubinstein (57), and is commonly observed in the electrochemistry of immobilized proteins (58, 59). The data points in Figure A.2.7 can be fitted to Butler-Volmer theory. The numerical implementation was developed by Heering et al. (60) for staircase digital voltammetry.

For interfacial electron transfer Butler-Volmer theory gives the reduction and oxidation rate constants k_f and k_b at a given potential E :

$$k_f(E) = k_0 e^{(-\alpha n F (E - E_0) / RT)}, \quad (\text{A2})$$

$$k_b(E) = k_0 e^{((1-\alpha) n F (E - E_0) / RT)}, \quad (\text{A3})$$

with k_0 the standard electron transfer rate constant at $E = E_0$, α the so-called symmetry parameter for the reduced and oxidized potential wells, E_0 the midpoint potential, n the number of electrons involved in the electron transfer

reaction (equal to 1 for azurin), R the gas constant ($8.31447 \text{ J mol}^{-1} \text{ K}^{-1}$), T the temperature (K) and F the Faraday constant ($9.6485309 \times 10^4 \text{ C mol}^{-1}$).

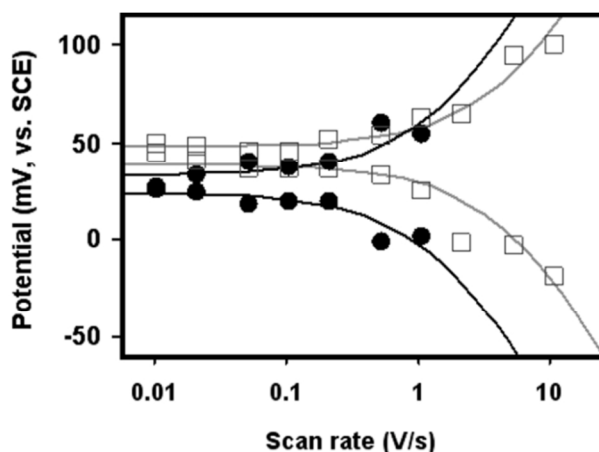


Figure A.2.7. Trumpet plot showing, respectively, the scan rate dependence of the peak separation in CV and of the separation between the reducing and oxidizing curves (at maximum slope) in FCV. CV peak potentials (open squares) were fit (grey line) with a standard electron transfer rate constant k_0 of $67 \pm 7 \text{ s}^{-1}$, a midpoint potential E_0 of $44 \pm 1 \text{ mV}$ (vs. SCE), and an UQR value of 9.7 mV . FCV maximum slope potentials (black diamonds - see text for more details) were fit with a standard electron transfer rate constant k_0 of $21 \pm 6 \text{ s}^{-1}$ with $E_0 = 29 \pm 1 \text{ mV}$, and UQR = 9.7 mV taken from CV fit.

To calculate the current as a function of potential during a scan, the potential is modeled as increasing stepwise from the starting point. The change in reduced and oxidized populations after each step will be determined by the rate constants in Eq. A2 and A3, by the values of these populations at the beginning of the step and by the time $t - t_{0,i}$ since the start of the step at time $t_{0,i}$. The time since the start of the step is generally written as a relative time $\tau = (t - t_{0,i})/t_{step}$, with t_{step} the time duration of the potential step between points i and $i+1$. The populations at $\tau = 0$ are equal to those at $\tau = 1$ at the end of the previous step $i-1$. This leads to the following equation for the oxidized population $N_{ox}(E_i, \tau)$:

$$N_{ox}(E_i, \tau) = \frac{N_{tot} \left(((k_{f,i} + k_{b,i}) \bar{N}_{ox}(E_i, \tau=0)) e^{-(k_{f,i} + k_{b,i}) t_{step} \tau} + k_{b,i} \right)}{(k_{f,i} + k_{b,i})}, \quad (\text{A4})$$

with N_{tot} the total population of redox-active proteins, e the electron charge and \bar{N}_{ox} the *relative* population of oxidized proteins. The step time t_{step} can be calculated from the potential step (which is always 1 mV in our case) divided by the scan rate v .

The current $I(E_i, \tau)$ at time τ is proportional to the change in oxidized population dN_{ox}/dt at time τ :

$$I(E_i, \tau) = neN_{tot} \cdot \left((k_{f,i} + k_{b,i})\bar{N}_{ox}(E_i, \tau = 0) - k_{b,i} \right) \left(e^{-(k_{f,i} + k_{b,i})t_{step} \cdot \tau} - 1 \right), \quad (\text{A5})$$

with e the electron charge ($1.60217646 \times 10^{-19}\text{C}$). In the simulation, the measured current $I(E_i)$ is taken to be averaged ('integrated current mode' of staircase voltammetry) over the full step interval from $\tau = 0$ to 1:

$$I(E_i) = \frac{neN_{tot} \cdot \left((k_{f,i} + k_{b,i})\bar{N}_{ox}(E_i, \tau = 0) - k_{b,i} \right) \left(e^{-(k_{f,i} + k_{b,i})t_{step} \cdot \tau} - 1 \right)}{\left((k_{f,i} + k_{b,i})t_{step} \right)}, \quad (\text{A6})$$

Using redox equilibrium to calculate \bar{N}_{ox} at the starting potential, the current during the voltage sweep can now be calculated from Eqs. A2–A6 for a given scan rate, k_0 and E_0 .

The current versus potential can be calculated from Eq. A6 for a given k_0 and E_0 , and the peak potential can be localized. A fitting table for the trumpet plot is then calculated for a large range of scan rates v using $k_0 = 1 \text{ s}^{-1}$ and $E_0 = 0 \text{ mV}$. The shape of the trumpet curve which corresponds to the table depends only on the ratio of v/k_0 , so the location of the fit w.r.t the scan rate (x) axis can be scaled by scaling with k_0 until the fitted peak separation matches the observed values. The location of the peaks on the potential (y) axis is fitted using both the midpoint potential E_0 and an additional UQR term to account for the nonzero separation at low scan rate.

2.4.6. Analyzing the FCV data. Fitting fluorescent cyclic voltammograms. In analyzing the change in fluorescence with potential two contributions are

considered. First, a redox-state dependent component which is proportional to the number of reduced proteins. Second, a small ‘field effect component’ which is linear with the potential, and applies to all proteins, whether reduced, oxidized or inactive.

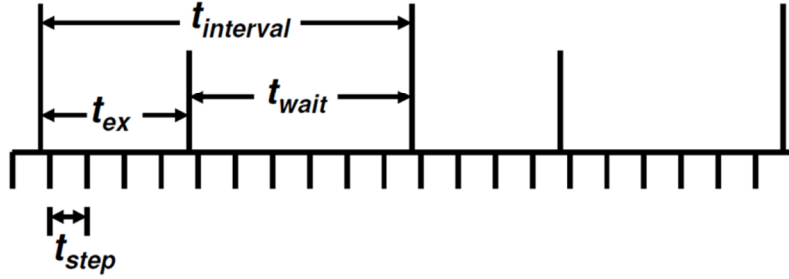


Figure A.2.8. Schematic representation of FCV measurement during a CV scan. An FCV potential sampling interval takes a time $t_{interval}$ which consists of an exposure time t_{exp} during which the fluorescence is measured, and a waiting time t_{wait} without fluorescence detection. Example shows the 200 mV/s epifluorescence case with a 20 ms exposure time corresponding to four steps of 1 mV, each taking a time t_{step} of 5 ms, and a waiting time t_{wait} of 30 ms which equals six 1-mV steps. Note that the exposure may start (and end) at any time during a potential step, as in this example.

The redox component is described by the Butler-Volmer theory for electron transfer kinetics applied to staircase CV as discussed above. The fluorescence is related to the amount of reduced protein N_{red} and reflects the average value of this population during camera exposure. To calculate this average, N_{ox} and N_{red} must be integrated over the potential step. Given k_f and k_b from Eqs. A2 and A3 and $N_{ox}(E_i)$ from Eq. A4, the full step integral for the populations N_{red} and N_{ox} for each potential E_i can be calculated:

$$N_{ox}(E_i) = \frac{N_{tot} \left(\left((k_{b,i} + k_{f,i}) N_{ox}(E_i, \tau=0) \right) e^{-(k_{f,i} + k_{b,i}) t_{step} \tau} + k_{b,i} \right)}{(k_{f,i} + k_{b,i})}, \quad (A7)$$

$$N_{red}(E_i) = N_{tot} - N_{ox}(E_i), \quad (A8)$$

with N_{tot} , \bar{N}_{ox} and t_{step} as defined above. As mentioned in the Methods section, the underlying step size applied to the sample is always the 1 mV potential step of the CV and that is the value which should be used to calculate t_{step} .

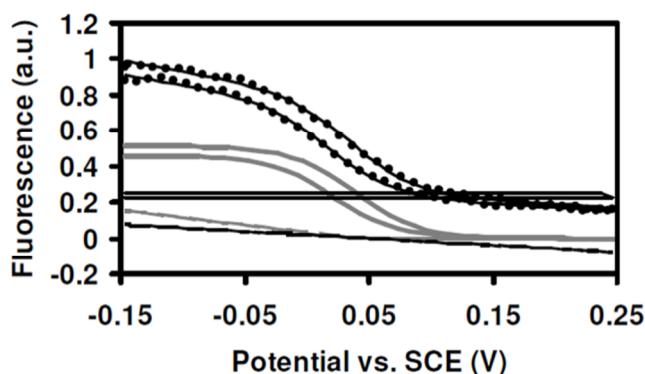


Figure A.2.9. Butler-Volmer theory based fit (see Eq. A10) of epifluorescent voltammogram measured at 200 mV/s scan rate. Full fit (thick black solid) is compared with data (dots). Separate fit contributions are also shown ($AN_{red}(E_j)$ - grey solid; B - thin black line); $AN_{red}(E_j) \cdot C(E_j - E_c)$ - grey dash, $BC(E_j - E_c)$ - black dots). See text for more details.

In general, an FCV measurement datapoint represent an average over several CV potential steps as illustrated in Figure A.2.8. The number of steps over which FCV is averaged is calculated from t_{exp}/t_{step} with t_{exp} the FCV exposure time (which is 20 ms in the epifluorescence measurements, and 300 ms in the TIRF measurements). Also, it is taken into account that some steps of Eqs. A7 and A8 are skipped by the fluorescence measurement during the waiting time t_{wait} between two image exposures (see also Figure A.2.8) and that fluorescence detection may start or end during a potential step (then a partial integral form of Eq. A7 from τ_{start} to $\tau = 1$ or from $\tau = 0$ to τ_{end} is used, not shown). We have calculated that such averaging allows preservation of the sigmoidal shape of FCV curves (within 1% error) as long as it is done over less than 30 mV. Moreover, any broadening of the fluorescence curves which may result from averaging over larger potential ranges is also reproduced in the simulations.

After averaging over t_{exp} , the following fluorescence intensity profile P is obtained for the redox component:

$$P(E_j) = AN_{red}(E_j) + B, \quad (A9)$$

with A the increase in fluorescence amplitude for the reduced protein (compared to oxidized), and B the fluorescence contribution from the active proteins when these are fully oxidized together with a contribution from the inactive proteins. To account for the 'field effect' the two contributions to $P(E_j)$ are multiplied with a factor $1 + C \cdot (E_j - E_c)$, where E_c is the potential in the center of the sweep range (which is 0.05 V in the epifluorescence experiments, 0V in TIRF). This gives:

$$P(E_j) = AN_{red}(E_j) + AN_{red}(E_j) \cdot C(E_j - E_c) + B + BC(E_j - E_c). \quad (A10)$$

Note that C is always negative, as the fluorescence change due to the field effect is negative with increasing potential.

For the epifluorescence data, a correction for the unusual quasi-reversibility was applied to E_0 by adding or subtracting $0.5 \cdot UQR$ for the oxidation and reduction traces, respectively. All in all, the fit parameters used are k_0 , E_0 , UQR , A_{ox} , A_{red} , B_{ox} , B_{red} , C_{ox} and C_{red} . The separation ΔE between the cathodic and anodic maximum slope potentials $E_{p,red}$ and $E_{p,ox}$ was quantified by considering the derivative of the first term in Eq. A10 (i.e. the term $AN_{red}(E_j)$), see also the grey curve in Figure A.2.9. The derivative was calculated from a 20 ms forward smoothed average of the 1 mV step interval form of $N_{red}(E_j)$ from Eq. A8 versus the also averaged potential. This way the curve with E_j with relatively few points was replaced by a curve with points at every 1 mV but similar averaging conditions. The maximum slope potentials could be determined from the derivative with an uncertainty of 1 mV connected with the step size.

In the fits to individual curves the values of UQR and k_0 are to some extent interdependent as the scan rate dependence cannot be used to determine UQR . Therefore UQR was fixed at the value of 9.7 mV as obtained from the CV fit, unless the total forward-backward separation in the curve was clearly smaller than this. For these latter curves, UQR was included as a fit parameter. The resulting separation ΔE in maximum slope potential was then used to repeat the fit with UQR as close to ΔE as possible. This choice yields an upper limit for the value of k_0 for that particular curve. For the TIRF data, no UQR was included in the Butler-Volmer fits, because including a UQR did not improve the fit to the rather scattered full image FCV trumpet plots (and no conventional CV could be measured due to the extremely low coverage).

We observed that 40% of the FCV traces from the TIRF data display very broad sigmoids that could not be reproduced or fitted to Butler-Volmer simulations and were therefore excluded from the analysis. Fits to quasi-Nernst curves of these traces yield an average apparent n of 0.2 ± 0.1 (note that n should be 1 for a reversible 1-electron redox process). A possible explanation for such broad curves could be inhomogeneity of the surface/molecule interactions *within* one ROI (51). Occasionally, even multiple waves are observed in the TIRF FCV data. When the electrical double layer is thicker than the protein adsorbate layer, both broadening and wave-doubling were predicted by Smith and White (61). The absence of such effects in the epifluorescence data could be due to the high ionic strength used.

In Figures 2.2 and A.2.4, the full-image epifluorescent FCVs are shown together with their Butler-Volmer fits (Eqs. A2-A10). All curves were first normalized to the maximum intensity at the start of the time trace. The fits reproduce the data very well, including the slight difference in slope at the negative and positive ends of the curve. When the relative amplitudes are compared, the signal is found to be dominated by the contribution from the redox transition (AN_{red}) and the constant fraction (B). The two 'field effect components' account for approximately 20% of the total signal. This aligns closely with the 20%

modulation which was observed for Zn-azurin at low scan rates (see Figure A.2.6). The four components of the fit corresponding to the four terms in the right-hand side of Eq. A10 are shown in Figure A.2.9 for the 200 mV/s FCV scan.

2.4.7. Comparison between conventional CV and full-image FCV data. The values obtained from fitting Eq. A10 to the full-image epifluorescent FCV data are given in Table A.2.1 in column 4 (E_0), column 5 (the peak separation ΔE , which is given by the separation between the cathodic and anodic maximum slope potentials $E_{p,red}$ and $E_{p,ox}$ ¹ and column 6 (k_0). In Table A.2.2, the E_0 , ΔE , k_0 and SR results are collected from the Butler-Volmer fits to the diffraction-limited epifluorescence ROI FCV curves at 200 mV/s scan rate.

The maximum slope potentials $E_{p,red}$ and $E_{p,ox}$ for the full-image FCV data are also shown in the trumpet plot in Figure A.2.7 (filled circles). The scan rate dependence of ΔE was fitted to a table in the same way as described above for the CV (Section 2.4.5). From this fit, a standard electron transfer rate constant of $k_0 = 21 \pm 6 \text{ s}^{-1}$ and a midpoint potential of $E_0 = 29 \pm 1 \text{ mV}$ were obtained. The value of UQR for the FCV fit was fixed at the value of 9.7 mV obtained from the fit to the CV trumpet plot. If UQR is included as a fit parameter, a value of 12 mV is obtained, but E_0 and k_0 are not significantly altered. This justifies the use of the CV value for the UQR in the FCV trumpet plot as well as for the individual fits.

¹ Due to asymmetry of the sigmoidal reduction (/oxidation) wave at less-than-infinite electron transfer rates, the FCV half wave potential is in general not equal to the potential of maximum FCV slope. The simulations show that the potential of the FCV maximum slope does correspond to the current peak potential of the CV, hence the notation E_p . The full details of the calculation of $E_{p,ox}$ and $E_{p,red}$ are given in the Appendix.

Table A.2.1. Comparison of CV and full-image epifluorescence FCV midpoint potentials and peak/maximum slope point separations, together with FCV-based values for the standard rate constant.

Scan rate,	E_0 , mV ^a	ΔE , mV ^b	E_0 , mV ^c	ΔE , mV ^d	k_0 (s ⁻¹) ^e
mV/s	CV	CV	FCV	FCV	FCV
10	48	5	27	1	22
20	45	8	28	9	11
50	42	9	29	22	6.2
100	42	9	28	18	19
200	44	15	30	21	26
500	43	21	30	62	12
1000	44	38	28	53	30
2000	32	67			
5000	46	98			
10000	41	119			

^a CV midpoint potential. All midpoint potentials are vs. SCE. CV values were determined with Gaussian peak fits, FCV values with Butler-Volmer theory based fits (Eq. A10). See text for more details.

^b CV peak separation.

^c FCV midpoint potential (average of cathodic and anodic maximum slope potentials) from 'CV' contribution (term $AN_{red}(E_j)$ to Eq. A10).

^d FCV maximum slope point separation from 'CV' contribution (term $AN_{red}(E_j)$ to Eq. A10).

^e Standard electron transfer rate constant k_0 from FCV fit (Eq. A10).

FCV of azurin

Table A.2.2. Epifluorescent FCV parameters of all ROIs measured at 200 mV/s (image shown in Figure 2.3).

ROI #	E_0 , mV ^a	ΔE , mV ^b	k_0 (s ⁻¹) ^c	SR ^d	I ^e , a.u.
1	30	19	30	0.90	0.38
2	25	16	48	0.74	0.68
3	28	104	2.1	0.42	0.82
4	33	20	30	0.86	0.41
5	26	12	185	0.84	0.50
6	35	14	72	0.79	0.58
7	34	33	12	0.86	0.26
8	29	12	112	0.72	0.88
9	26	48	6.9	0.49	1.0
10	22	71	3.9	0.36	0.73
11	28	65	4.4	0.45	1.0
12	33	48	7.0	0.62	0.55
13	34	70	3.9	0.37	0.84
14	12	121	1.7	0.41	0.53

^a Midpoint potential (average of maximum slope points vs. SCE). Midpoint potentials, maximum slope point separations and electron transfer rate constants were obtained from 'CV' contribution of Butler-Volmer fits (first term of Eq. A10, $AN_{red}(E_j)$). Switching ratio was obtained from the full fit (all contributions to Eq. A10).

^b Maximum slope point separation.

^c Standard electron transfer rate constant.

^d Switching ratio.

^e Integrated ROI intensity, relative to the intensity of the brightest ROI.

2.4.8. Sample Size. Integrated CV peak areas (see, e.g., Figure 2.1, black curve) from epifluorescence samples are constant with scan rate and correspond to a charge transfer of $9(\pm 1) \times 10^{-8}$ C, or $6(\pm 1) \times 10^{11}$ electrons. For an electrode area of 0.20 cm^2 this corresponds to a molecular density of approximately $3(\pm 0.5) \times 10^{12}$ electroactive proteins (5 pmol) per cm^2 , a value comparable to other reports (13, 20, 62). From this, the population sampled in this configuration can be estimated, with images of 100×100 pixels ($\sim 16 \times 16$ microns), to be 8×10^6 proteins. With the labeling ratio of 16% for the Cu azurin sample used, less than 2×10^6 proteins are typically monitored through fluorescence from a full image. A further 5,000-fold decrease in sample size is attainable through examining FCVs from diffraction-limited spots (ROIs); with a diameter of 300 nm, these each contain as few as 500 fluorescently labeled proteins.

The variation in intensity in the epifluorescence images suggests a variation in surface coverage. The magnitude of this variation can be determined from the fluorescence images, assuming that the brightness scales directly with the surface coverage. A single pixel in the image represents a surface area of $160 \times 160 \text{ nm}$. On average, such a pixel contains 800 electroactive proteins given the surface coverage of $3(\pm 0.5) \times 10^{12} \text{ cm}^{-2}$ calculated above. For a typical bright spot of ~ 2 times the average fluorescence intensity, the total protein density becomes ~ 1600 proteins per pixel. This corresponds to near-monolayer coverage if a protein footprint of $\sim 10 \text{ nm}^2$ is assumed. The presence of even brighter spots (which can be 5 times the average or more) indicates the presence of protein aggregates.

The lower surface coverage used in TIRF experiments prohibits the acquisition of Faradaic responses above noise. Extensive AFM analyses of these samples enabled the range of molecular density to be resolved directly. We estimate a value of $5(\pm 3) \times 10^{11} \text{ molecules/cm}^2$ to be representative of the ROIs sampled in these measurements. The large dispersion here is indicative of the heterogeneity observed on these scales and is equivalent to the brightness variation seen in

epifluorescence. A diffraction limited ROI then contains 110–450 fluorescently tagged molecules.

2.4.9. Width calculations of E_0 and k_0 histograms. The Butler-Volmer fit of the FCV for each ROI i yields a midpoint potential E_0 with a noise-induced standard deviation $\sigma_{E_0}(i)$. The noise contribution $\sigma_{E_0}(i)$ is calculated from the dimensionless sum of squared differences (χ^2), divided by the number of datapoints N , of the fit as follows:

$$\sigma_{E_0} = \sqrt{\chi^2/N} / A \times (4RT/nF), \quad (\text{A11})$$

with A the amplitude of the fit contribution that corresponds to the redox transition (first term of Eq. A10, AN_{red}) as only this term determines E_0 . The term $4RT/nF$ is calculated using $n = 0.86$, which is the average between $n = 1$ for ideal reversible electron transfer and 0.71 for the lowest n compatible with Butler-Volmer kinetics. With $T = 295$ K this gives $4RT/nF = 118$ mV. The total standard deviation of the histogram σ_T is the resultant of noise and intrinsic dispersion, i.e. $\sigma_T^2 = \sigma_N^2 + \sigma_{disp}^2$, where $\sigma_N^2 = (1/N) \sum \sigma_{E_0}(i)^2$ is the average contribution of the noise of N ROIs to the histogram, and the standard deviation σ_{disp} is the measure of the true thermodynamic dispersion. For the epifluorescence data (Figure 2.4a), the mean midpoint potential is 28 mV with $\sigma_T = 6$ mV, and $\sigma_N = 6$ mV, yielding a dispersion $\sigma_{disp} \leq 1$ mV. For the TIRF data (Figure 2.4b), the mean midpoint potential is 4 mV with $\sigma_T = 39$ mV, and $\sigma_N = 25$ mV, yielding a dispersion $\sigma_{disp} = 30$ mV.

In the same manner as for E_0 , the intrinsic kinetic dispersion can be obtained from the histograms of $\log(k_0)$ and the sum of the standard deviations of the fitted $\log(k_0)$ for each ROI i . The individual fit uncertainty $\sigma_{\log(k_0)}(i)$ is calculated as:

$$\sigma_{\log(k_0)} = \sqrt{\chi^2/N} / A \times (4/n(\log 10)), \quad (\text{A12})$$

with A and n the same as above (Eq. A11). The overall standard deviation of the histogram σ_T thus is given by $\sigma_T^2 = \sigma_N^2 + \sigma_{disp}^2$, where $\sigma_N^2 = (1/N) \sum \sigma_{\log(k_0)}(i)^2$ is the average contribution of noise from N ROIs, and standard deviation σ_{disp} is the measure of the kinetic dispersion. For the epifluorescence data (Figure 2.4c) the mean $\log(k_0) = 1.2$ (corresponding to a k_0 of 15 s^{-1}), $\sigma_T = 0.7$, and $\sigma_N = 0.1$, yielding a dispersion $\sigma_{disp} = 0.7$ which is almost equal to the total width. For the TIRF data (Figure 2.4d) the mean is $\log(k_0) = 0.2$ corresponding to a k_0 of 1.5 s^{-1} . The width of the histogram is $\sigma_T = 0.7$ and the noise contribution $\sigma_N = 0.4$, yielding a dispersion σ_{disp} of 0.5.

2.4.10. Sample preparation. Preparation and purification of wild-type and N42C azurin were carried out as previously described (19, 44, 63). Wild-type (wt) azurin was labeled on the N-terminus (Figure A.2.1) following the protocol described by Kuznetsova et al. (12), using 20 mM Hepes buffer at pH 8.3, 1 h incubation of dye and protein in 1:5 ratio and size exclusion chromatography (Centrispin 10, Princeton separations) to separate the labeled protein from free dye. The labeling ratio is kept well below 1, with a value of 0.16 for the particular wt azurin experiment discussed here. To check for possible non-redox-dependent contributions to the fluorescence, zinc-reconstituted wt azurin was used as a control sample. This was purified and labeled in the same way as the native Cu azurin. N42C azurin was labeled on the N-terminus by incubating dye and protein in a ratio of 1:2 in 20 mM Hepes buffer, pH 9.1, for 2 h at room temperature, followed by centrifugal filtration (Microcon YM-3, Millipore, UK), and dilution with 20 mM potassium phosphate buffer at pH 7.1. The labeling ratio for the used N42C sample was 0.55.

2.4.11. Sample immobilization and electrode preparation. The working electrode was prepared in-house and consisted of a semi-transparent gold layer

of 10 nm thickness which was deposited on a glass coverslip (1" diameter, thickness 0.14-0.17 mm (#1), Menzel). Prior to gold deposition, the slide was cleaned by several seconds of sonication in isopropanol, followed by short sonication in milliQ water. The cleaned coverslips were blown dry with nitrogen gas and used for gold coating immediately. Thin gold films were prepared either by RF sputtering (ATC 1800F, AJA International) or with a resistive heating evaporator (Edward Auto 306 cryo evaporator). Sputtering was performed according to the protocol described by van Baarle et al. (45). Good adhesion of the gold layer to the glass was ensured by first sputtering a layer of molybdenum-germanium (MoGe) of ~2nm thickness under 100% argon pressure. During subsequent gold sputtering, 5% partial oxygen pressure was added to increase surface flatness (45). The sputtered gold surface was polycrystalline, i.e. not atomically flat, but homogeneous (roughness of approximately 3 Å RMS over a range of tens of microns). For the coverslips prepared by thermal evaporation, 10 nm of chromium was used as an adhesion layer. These electrodes had a roughness of ~1 nm (measured over tens of microns). The conductance and optical transmission characteristics of both types of electrodes were comparable.

To immobilize azurin on transparent gold electrodes, a self-assembling monolayer (SAM) of alkanethiol was used as an intermediate layer. Due to the hydrophobic patch on the protein surface, which is close to the azurin copper center, the molecule is expected to orient with its redox center towards the hydrophobic alkanethiol head groups, a favorable orientation for electron transfer (22, 62, 64, 65). To enable good SAM formation, transparent gold electrodes were first cleaned by putting them in freshly prepared Piranha solution (1:3 mixture of 30% H₂O₂:conc. H₂SO₄) for 5 minutes (note that this solution is highly corrosive and should be handled with considerable care!). The slides were then rinsed with copious amounts of milliQ water, blown dry with nitrogen and soaked overnight (12-15 hrs) in alkanethiol solution. For the wt azurin experiments, SAMs were prepared by incubating the gold surface with 1-

hexanethiol (10 mM ethanolic solution). Zinc azurin and N42C were immobilized on a 1-octanethiol SAM (equivalently prepared).

Before protein incubation, SAM-soaked gold electrodes were rinsed with ethanol, blown dry, rinsed with milliQ water and blown dry again. The dry coverslip was then turned into a working electrode by depositing a small ring of silicon paste to contain a droplet of 50-100 μ l. For epifluorescence experiments on wt azurin, a droplet of \sim 1 μ M azurin solution was placed inside the ring and left to incubate for \sim 15 minutes at room temperature. For the immobilization step, a degassed *low*-salt (10 mM) potassium phosphate buffer was used to minimize aggregation of azurin on the surface. After incubation, unbound protein was removed by rinsing 3 or 4 times with fresh buffer. The buffer which was used during the measurements had a *high* salt concentration (500 mM phosphate, degassed) to limit the 'field effect' described in Section 2.4.4. For TIRF measurements, Cy5-labeled N42C (200 nM in 20 mM potassium phosphate pH 7.1) was left to incubate on SAM-coated transparent gold electrodes for 2 hours at 2-4 $^{\circ}$ C. The measurement buffer had a concentration of 100 mM. All TIRF and epifluorescence measurements were performed at a pH of 7.0.

2.4.12. Fluorescent electrochemistry setup. Epifluorescence was observed with an inverted microscope (Zeiss Axiovert 200 with Plan Apo 100X oil objective). Cy5 excitation was provided by a red diode laser (wavelength 639 nm, Power Technology Inc., IQ1A30). Typical excitation power was 1 mW in a beam diameter with gaussian FWHM of about 20 micron, corresponding to an average intensity of 0.3 kW/cm². A 660 nm long pass dichroic mirror (Chroma Q660LP) and 700 nm bandpass emission filter (Chroma HQ700/75) with additional glass filter (Itos RG665) ensured the removal of scattered laser light from the emission path. Cy5 fluorescence was detected with a Peltier-cooled CCD camera (Cascade 512 X, Roper Scientific). Fluorescence was measured in a series of images (a 'movie'), with a camera exposure time of 20 ms per image ('frame'). Admission of excitation light to the sample was limited to the camera exposure time, restricting sample bleaching in between image recordings. This was achieved by

placing an acousto-optical transmission filter (AOTF) in the excitation beam path. A home-written Labview application controlled both the AOTF and the CCD camera.

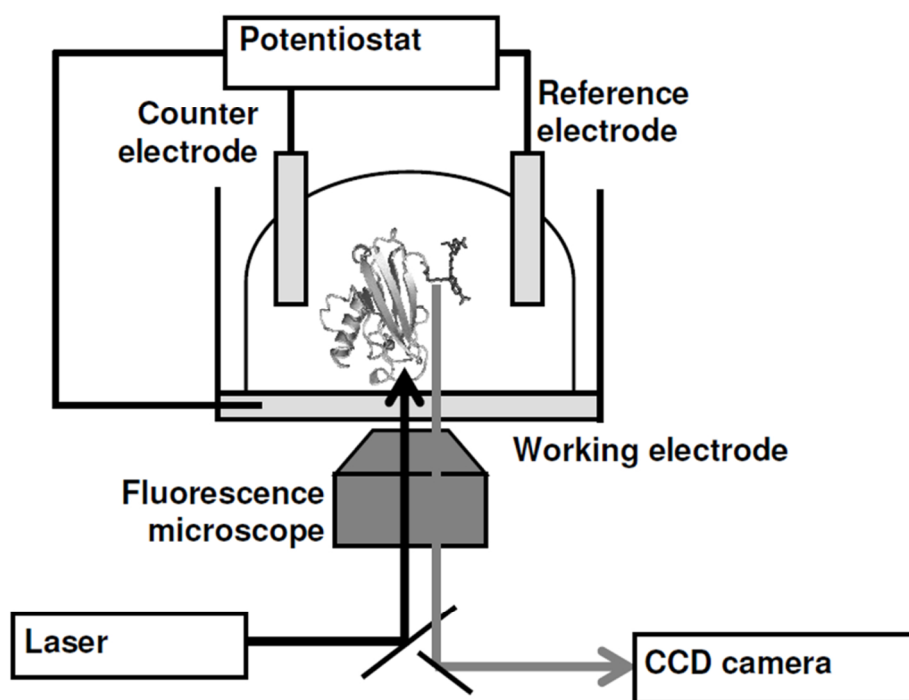


Figure A.2.10. Fluorescent cyclic voltammetry setup, consisting of a fluorescence microscope with an electrochemical sample cell. The glass coverslip is coated with a 10 nm gold layer which functions as working electrode.

TIRF measurements were carried out using a Nikon TE2000-E microscope equipped with a TIRF module (with intermediate magnification of 1.5x). Samples were excited with a 20 mW 633nm CW laser (model 1135, JD Uniphase) through an oil immersion 100x Nikon Plan Apo TIRF objective. Emitted fluorescence light was filtered through a dichroic mirror (660 nm LP) and a (700/75 nm) band pass filter and was recorded with a back illuminated iCCD camera (Andor, Belfast, Northern Ireland). A schematic representation of the combined electrochemistry and epifluorescence/TIRF setup is shown in Figure A.2.10.

TIRF measurements were performed at low surface coverage (well below 10^{12} proteins/cm², see Section 2.4.8) to minimize sampling size. The necessary long

exposure times (typically 300 ms) were accompanied by a 5–20% decrease in fluorescence intensity through photobleaching in the course of an FCV scan. This was compensated for by fitting a third order polynomial to the decay peak amplitudes of the observed periodic variations in fluorescence intensity.

Conventional staircase CV scans were measured at rates ranging from 10 mV/s to 10 V/s, in potential steps of 1 mV. CV scanning was combined with fluorescence detection up to 1 V/s scan rate (scan range -0.15 to $+0.25$ V vs. SCE for epifluorescence, -0.5 to $+0.5$ V vs. SCE for TIRF). For epifluorescent FCV scans, the sampling interval between frames was 10 mV for scan rates ranging from 10 mV/s to 200 mV/s, and 20 mV and 40 mV for scan rates of 0.5 V/s and 1 V/s, respectively. For TIRF scans, the sampling intervals were larger (from 18 mV to 120 mV depending on the scan rate) due to the necessarily longer exposure time. TIRF FCV was measured at scan rates between 25 mV/s and 600 mV/s. To construct the epifluorescence FCV, the potential of the working electrode was read out from the analog signal output of the potentiostat which was connected to the analog input of a data-acquisition (DAQ) card (National Instruments, PCI-MIO-16XE-10). The DAQ-card input was processed by the home-written Labview application and the working electrode potential was stored with each image frame. TIRF FCV traces were constructed by averaging the applied potentials during each sampling interval, after synchronizing the initial potential jump from 0 to -0.5 V with the resulting fluorescence jump.

References

1. P.Yeh TK. 1977. Reversible Electrode Reaction of Cytochrome C. *Chemistry Letters* 6(10):1145–1148.
2. Brown AP and Anson FC. 1977. Cyclic and differential pulse voltammetric behavior of reactants confined to the electrode surface. *Analytical Chemistry* 49(11):1589–1595. American Chemical Society.
3. Smith DF, Willman K, Kuo K, and Murray RW. 1979. Chemically modified electrodes. *Journal of Electroanalytical Chemistry and Interfacial Electrochemistry* 95(2):217–227.

4. Rowe GK, Carter MT, Richardson JN, and Murray RW. 1995. Consequences of Kinetic Dispersion on the Electrochemistry of an Adsorbed Redox-Active Monolayer. *Langmuir* 11(5):1797–1806. American Chemical Society.
5. Clark RA and Bowden EF. 1997. Voltammetric Peak Broadening for Cytochrome c /Alkanethiolate Monolayer Structures: Dispersion of Formal Potentials. *Langmuir* 13(3):559–565. American Chemical Society.
6. Zhang Z and Rusling JF. 1997. Electron transfer between myoglobin and electrodes in thin films of phosphatidylcholines and dihexadecylphosphate. *Biophysical Chemistry* 63(2-3):133–146.
7. Hirst J and Armstrong FA. 1998. Fast-Scan Cyclic Voltammetry of Protein Films on Pyrolytic Graphite Edge Electrodes: Characteristics of Electron Exchange. *Analytical Chemistry* 70(23):5062–5071. American Chemical Society.
8. Jeuken LJC and Armstrong FA. 2001. Electrochemical Origin of Hysteresis in the Electron-Transfer Reactions of Adsorbed Proteins : Contrasting Behavior of the “ Blue ” Copper Protein , Azurin , Adsorbed on Pyrolytic Graphite and Modified Gold Electrodes. *Journal of Physical Chemistry B* 105:5271–5282.
9. Léger C, Jones AK, Albracht SPJ, and Armstrong FA. 2002. Effect of a Dispersion of Interfacial Electron Transfer Rates on Steady State Catalytic Electron Transport in [NiFe]-hydrogenase and Other Enzymes. *The Journal of Physical Chemistry B* 106(50):13058–13063. American Chemical Society.
10. Schmauder R, Alagaratnam S, Chan C, Schmidt T, Canters GW, and Aartsma TJ. 2005. Sensitive detection of the redox state of copper proteins using fluorescence. *Journal of biological inorganic chemistry : JBIC : a publication of the Society of Biological Inorganic Chemistry* 10(6):683–7.
11. Schmauder R, Librizzi F, Canters GW, Schmidt T, and Aartsma TJ. 2005. The oxidation state of a protein observed molecule-by-molecule. *Chemphyschem : a European journal of chemical physics and physical chemistry* 6(7):1381–6.
12. Kuznetsova S, Zauner G, Schmauder R, Mayboroda O a, Deelder AM, Aartsma TJ, and Canters GW. 2006. A Förster-resonance-energy transfer-based method for fluorescence detection of the protein redox state. *Analytical biochemistry* 350(1):52–60.
13. Davis JJ, Burgess H, Zauner G, Kuznetsova S, Salverda J, Aartsma T, and Canters GW. 2006. Monitoring interfacial bioelectrochemistry using a FRET switch. *The journal of physical chemistry. B* 110(41):20649–54.
14. Kuznetsova S, Zauner G, Aartsma TJ, Engelkamp H, Hatzakis N, Rowan AE, Nolte RJM, Christianen PCM, and Canters GW. 2008. The enzyme mechanism of nitrite reductase studied at single-molecule level. *Proceedings of the National Academy of Sciences of the United States of America* 105(9):3250–5.
15. Groeneveld CM and Canters GW. 1988. NMR study of structure and electron transfer mechanism of *Pseudomonas aeruginosa* azurin. *J. Biol. Chem.* 263(1):167–173.
16. Kamp M Van de and Floris R. 1990. Site-directed mutagenesis reveals that the hydrophobic patch of azurin mediates electron transfer. *Journal of the American Chemical Society* 112(20):907–908.
17. Nar H, Messerschmidt A, Huber R, Van de Kamp M, and Canters GW. 1991. Crystal structure analysis of oxidized *Pseudomonas aeruginosa* azurin at pH 5.5 and pH 9.0. A pH-induced conformational transition involves a peptide bond flip. *Journal of Molecular Biology* 221(3):765–72.

18. Armstrong FA, Heering HA, and Hirst J. 1997. Reaction of complex metalloproteins studied by protein-film voltammetry. *Chemical Society Reviews* 26(3):169. The Royal Society of Chemistry.
19. Van Amsterdam IMC, Ubbink M, Einsle O, Messerschmidt A, Merli A, Cavazzini D, Rossi GL, and Canters GW. 2002. Dramatic modulation of electron transfer in protein complexes by crosslinking. *Nature structural biology* 9(1):48–52.
20. Davis JJ, Bruce D, Canters GW, Crozier J, and Hill HAO. 2003. Genetic modulation of metalloprotein electron transfer at bare gold. *Chemical Communications*(5):576–577. The Royal Society of Chemistry.
21. Zhang J, Guo S-X, Bond AM, Honeychurch MJ, and Oldham KB. 2005. Novel kinetic and background current selectivity in the even harmonic components of fourier transformed square-wave voltammograms of surface-confined azurin. *The journal of physical chemistry. B* 109(18):8935–47. American Chemical Society.
22. Chi Q, Farver O, and Ulstrup J. 2005. Long-range protein electron transfer observed at the single-molecule level: In situ mapping of redox-gated tunneling resonance. *Proceedings of the National Academy of Sciences of the United States of America* 102(45):16203–8.
23. Messerschmidt A, Huber R, Poulas T, Wieghardt K, Cygler M, and Bode W, ed. 2006. *Handbook of Metalloproteins*. Chichester: John Wiley & Sons, Ltd.
24. Heering HA, Mondal MS, and Armstrong FA. 1999. Using the pulsed nature of staircase cyclic voltammetry to determine interfacial electron-transfer rates of adsorbed species. *Analytical chemistry* 71(1):174–82. American Chemical Society.
25. Feldberg SW and Rubinstein I. 1988. Unusual quasi-reversibility (UQR) or apparent non-kinetic hysteresis in cyclic voltammetry. *Journal of Electroanalytical Chemistry and Interfacial Electrochemistry* 240(1-2):1–15.
26. Smith JMM, Smith WH, and Knaff DB. 1981. Electrochemical titrations of a ferredoxin-ferredoxin:NADP⁺ oxidoreductase complex. *Biochimica et biophysica acta* 635(2):405–11.
27. Batie CJ and Kamin H. 1981. The relation of pH and oxidation-reduction potential to the association state of the ferredoxin . ferredoxin:NADP⁺ reductase complex. *J. Biol. Chem.* 256(15):7756–7763.
28. Gray K, Davidson V, and Knaff D. 1988. Complex formation between methylamine dehydrogenase and amicyanin from *Paracoccus denitrificans*. *Journal of Biological Chemistry* 263(28):13987–13990.
29. Drepper F, Hippler M, Nitschke W, and Haehnel W. 1996. Binding dynamics and electron transfer between plastocyanin and photosystem I. *Biochemistry* 35(4):1282–95. American Chemical Society.
30. Murgida DH and Hildebrandt P. 2008. Disentangling interfacial redox processes of proteins by SERR spectroscopy. *Chemical Society reviews* 37(5):937–45. The Royal Society of Chemistry.
31. Rivas L, Soares CM, Baptista AM, Simaan J, Di Paolo RE, Murgida DH, and Hildebrandt P. 2005. Electric-field-induced redox potential shifts of tetraheme cytochromes c3 immobilized on self-assembled monolayers: surface-enhanced resonance Raman spectroscopy and simulation studies. *Biophysical journal* 88(6):4188–99.

32. Crowley PB and Ubbink M. 2003. Close encounters of the transient kind: protein interactions in the photosynthetic redox chain investigated by NMR spectroscopy. *Accounts of chemical research* 36(10):723–30. American Chemical Society.
33. Crowley PB and Carrondo MA. 2004. The architecture of the binding site in redox protein complexes: implications for fast dissociation. *Proteins* 55(3):603–12.
34. Prudêncio M and Ubbink M. Transient complexes of redox proteins: structural and dynamic details from NMR studies. *Journal of molecular recognition : JMR* 17(6):524–39.
35. Hoffman BM, Celis LM, Cull DA, Patel AD, Seifert JL, Wheeler KE, Wang J, Yao J, Kurnikov I V, and Nocek JM. 2005. Differential influence of dynamic processes on forward and reverse electron transfer across a protein-protein interface. *Proceedings of the National Academy of Sciences of the United States of America* 102(10):3564–9.
36. Wheeler KE, Nocek JM, Cull DA, Yatsunyk LA, Rosenzweig AC, and Hoffman BM. 2007. Dynamic docking of cytochrome b5 with myoglobin and alpha-hemoglobin: heme-neutralization “squares” and the binding of electron-transfer-reactive configurations. *Journal of the American Chemical Society* 129(13):3906–17. American Chemical Society.
37. Xiong P, Nocek JM, Griffin AKK, Wang J, and Hoffman BM. 2009. Electrostatic redesign of the [myoglobin, cytochrome b5] interface to create a well-defined docked complex with rapid interprotein electron transfer. *Journal of the American Chemical Society* 131(20):6938–9. American Chemical Society.
38. Qiang Feng Z, Imabayashi S, Kakiuchi T, and Niki K. 1997. Long-range electron-transfer reaction rates to cytochrome c across long- and short-chain alkanethiol self-assembled monolayers: Electroreflectance studies. *Journal of the Chemical Society, Faraday Transactions* 93(7):1367–1370. The Royal Society of Chemistry.
39. Avila A, Gregory BW, Niki K, and Cotton TM. 2000. An Electrochemical Approach to Investigate Gated Electron Transfer Using a Physiological Model System: Cytochrome c Immobilized on Carboxylic Acid-Terminated Alkanethiol Self-Assembled Monolayers on Gold Electrodes. *The Journal of Physical Chemistry B* 104(12):2759–2766. American Chemical Society.
40. Fujita K, Nakamura N, and Ohno H. 2004. Mimicking protein-protein electron transfer: Voltammetry of *Pseudomonas aeruginosa* azurin and the *Thermus thermophilus* CuA domain at ω -derivatized self-assembled-monolayer gold electrodes. *Journal of the American Chemical Society* 126(4):13954–13961.
41. Yue H, Khoshtariya D, Waldeck DH, Grochol J, Hildebrandt P, and Murgida DH. 2006. On the electron transfer mechanism between cytochrome C and metal electrodes. Evidence for dynamic control at short distances. *The journal of physical chemistry. B* 110(40):19906–13. American Chemical Society.
42. Khoshtariya DE, Dolidze TD, Shushanyan M, Davis KL, Waldeck DH, and Van Eldik R. 2010. Fundamental signatures of short- and long-range electron transfer for the blue copper protein azurin at Au/SAM junctions. *Proceedings of the National Academy of Sciences of the United States of America* 107(7):2757–62.
43. Murgida DH and Hildebrandt P. 2004. Electron-transfer processes of cytochrome C at interfaces. New insights by surface-enhanced resonance Raman spectroscopy. *Accounts of chemical research* 37(11):854–61. American Chemical Society.
44. Van de Kamp M, Hali FC, Rosato N, Agro a F, and Canters GW. 1990. Purification and characterization of a non-reconstitutable azurin, obtained by heterologous expression of the *Pseudomonas aeruginosa* azu gene in *Escherichia coli*. *Biochimica et biophysica acta* 1019(3):283–92.

45. Van Baarle GJC, Troianovski a. M, Nishizaki T, Kes PH, and Aarts J. 2003. Imaging of vortex configurations in thin films by scanning-tunneling microscopy. *Applied Physics Letters* 82(7):1081.
46. Pettigrew GW, Leitch FA, and Moore GR. 1983. The effect of iron-hexacyanide binding on the determination of redox potentials of cytochromes and copper proteins. *Biochimica et Biophysica Acta (BBA) - Bioenergetics* 725(3):409–416.
47. Clair CS, Ellis W, and Gray H. 1992. Spectroelectrochemistry of blue copper proteins: pH and temperature dependences of the reduction potentials of five azurins. *Inorganica chimica acta* 191:149–155.
48. Van de Kamp M, Canters GW, Andrew CR, Sanders-Loehr J, Bender CJ, and Peisach J. 1993. Effect of lysine ionization on the structure and electrochemical behaviour of the Met44-->Lys mutant of the blue-copper protein azurin from *Pseudomonas aeruginosa*. *European journal of biochemistry / FEBS* 218(1):229–38.
49. Van Pouderoyen G, Mazumdar S, Hunt NI, Hill AO, and Canters GW. 1994. The introduction of a negative charge into the hydrophobic patch of *Pseudomonas aeruginosa* azurin affects the electron self-exchange rate and the electrochemistry. *European journal of biochemistry / FEBS* 222(2):583–8.
50. Zauner G, Lonardi E, Bubacco L, Aartsma TJ, Canters GW, and Tepper AWJW. 2007. Tryptophan-to-dye fluorescence energy transfer applied to oxygen sensing by using type-3 copper proteins. *Chemistry-A European Journal* 13(25):7085–90.
51. Laviron E. 1979. General expression of the linear potential sweep voltammogram in the case of diffusionless electrochemical systems. *Journal of Electroanalytical Chemistry and Interfacial Electrochemistry* 101(1):19–28.
52. Bard AJ and Faulkner LR. 2000. *Electrochemical Methods: Fundamentals and Applications*. 856. Wiley.
53. Enderlein J. 2000. A Theoretical Investigation of Single-Molecule Fluorescence Detection on Thin Metallic Layers. *Biophysical Journal* 78(4):2151–2158.
54. Dulkeith E, Ringler M, Klar TA, Feldmann J, Muñoz Javier A, and Parak WJ. 2005. Gold nanoparticles quench fluorescence by phase induced radiative rate suppression. *Nano letters* 5(4):585–9. American Chemical Society.
55. Vasilev K, Stefani FD, Jacobsen V, Knoll W, and Kreiter M. 2004. Reduced photobleaching of chromophores close to a metal surface. *The Journal of chemical physics* 120(14):6701–4.
56. Stefani F, Vasilev K, Bocchio N, Stoyanova N, and Kreiter M. 2005. Surface-Plasmon-Mediated Single-Molecule Fluorescence Through a Thin Metallic Film. *Physical Review Letters* 94(2):023005. American Physical Society.
57. Feldberg SW and Rubinstein I. 1988. Unusual quasi-reversibility (UQR) or apparent non-kinetic hysteresis in cyclic voltammetry. *Journal of Electroanalytical Chemistry and Interfacial Electrochemistry* 240(1-2):1–15.
58. Armstrong FA, Camba R, Heering HA, Hirst J, Jeuken LJ, Jones AK, Léger C, and McEvoy JP. 2000. Fast voltammetric studies of the kinetics and energetics of coupled electron-transfer reactions in proteins. *Faraday discussions*(116):191–203; discussion 257–68.
59. Heering HA, Wiertz FGM, Dekker C, and De Vries S. 2004. Direct immobilization of native yeast iso-1 cytochrome C on bare gold: fast electron relay to redox enzymes and zeptomole protein-film voltammetry. *Journal of the American Chemical Society* 126(35):11103–12.

60. Heering HA, Mondal MS, and Armstrong FA. 1999. Using the pulsed nature of staircase cyclic voltammetry to determine interfacial electron-transfer rates of adsorbed species. *Analytical chemistry* 71(1):174–82. American Chemical Society.
61. Smith CP and Dwhite HS. 1992. Theory of the interfacial potential distribution and reversible voltammetric response of electrodes coated with electroactive molecular films. *Analytical chemistry* 64(20):2398–405. American Chemical Society.
62. Chi Q and Zhang J. 2001. Ordered assembly and controlled electron transfer of the blue copper protein azurin at gold (111) single-crystal substrates. *Journal of Physical Chemistry B* 105(11):4669–4679.
63. Van Amsterdam IM, Ubbink M, Jeuken LJ, Verbeet MP, Einsle O, Messerschmidt A, and Canters GW. 2001. Effects of dimerization on protein electron transfer. *Chemistry (Weinheim an der Bergstrasse, Germany)* 7(11):2398–406.
64. Zhang J, Chi Q, Kuznetsov a. M, Hansen a. G, Wackerbarth H, Christensen HEM, Andersen JET, and Ulstrup J. 2002. Electronic Properties of Functional Biomolecules at Metal/Aqueous Solution Interfaces. *The Journal of Physical Chemistry B* 106(6):1131–1152.
65. Yokoyama K, Leigh BS, Sheng Y, Niki K, Nakamura N, Ohno H, Winkler JR, Gray HB, and Richards JH. 2008. Electron Tunneling through *Pseudomonas aeruginosa* Azurins on SAM Gold Electrodes. *Inorganica chimica acta* 361(4):1095–1099.

Chapter 3

Fluorescence-detected electrochemistry of single redox proteins reveals the thermodynamic dispersion[#]

[#] Namik Akkilić, Jante M. Salverda, Gerard W. Canters, Thijs J. Aartsma. 2013. to be submitted.

Abstract

There are several parameters that can influence molecular electron transfer such as protein folding, electric field drop, and molecular orientation. Classical electrochemistry and spectroscopy are not sufficient to control and solve such influences at the molecular level. Redox-active metalloproteins tagged with a FRET-coupled organic fluorophore can be used to study electron transfer to a transparent conductive electrode in an optical configuration. Herein, we show that we can observe redox switching under potentiostatic control of individual, wild-type (wt) azurin molecules, tagged with Cy5 and immobilized on a semi-transparent gold electrode via an octanethiol self-assembled monolayer. The distribution of optically-determined midpoint potentials of individual azurin molecules gave a maximum value at 45.7 ± 0.5 mV with and fwhm of 15 mV (vs. SCE). The work presented here, shows direct measurement of controlled electron-switching, one electron at a time, of an individual redox protein, and its thermodynamic dispersion.

3.1 Introduction

The development of redox-gated (bio)molecular electronic devices and protein biochips is critically dependent on the electron transfer (ET) across the molecule-substrate interfaces (1–4). Such devices may incorporate metalloproteins which are at the central core of numerous chemical and biological processes and which have a remarkable ability to drive ET reactions in e.g., photosynthesis, cellular respiration and signaling (5, 6). Interfacial electrochemical ET has been extensively studied to investigate thermodynamic properties and quantitative electronic parameters of redox-active biomolecules, as well as their structure and distance dependence when adsorbed on conductive substrates (7–13).

It is considered a great challenge to increase the sensitivity of detection in the field of bioelectrochemistry, which drives the development of new methods and techniques. For example, electrochemical tunneling microscopy (ECSTM) has been used to map the tunneling resonance of single redox proteins (14–16), and to measure their electron transfer distance decay constants (16, 17). Furthermore, the miniaturization of the electrode construction (18) has been pursued, while another approach takes advantage of redox cycling in so-called nanogap transducers (19).

Being based on amperometric detection, these methods are inherently limited by the sensitivity of electric current measurements, requiring at least a 1000 electrons/s or so to obtain a measurable signal. In recent years, an enhanced sensitivity was achieved with spectroelectrochemistry which combines spectroscopy and electrochemistry. It takes advantage of the fact that the electronic energy transitions of many redox proteins exhibit an absorbance change in the UV-Vis region upon oxidation or reduction. It has been successfully applied to cytochrome c (20–22), blue copper proteins (21, 23) and redox enzymes (24, 25). Single-molecule sensitivity of spectroelectrochemistry at the

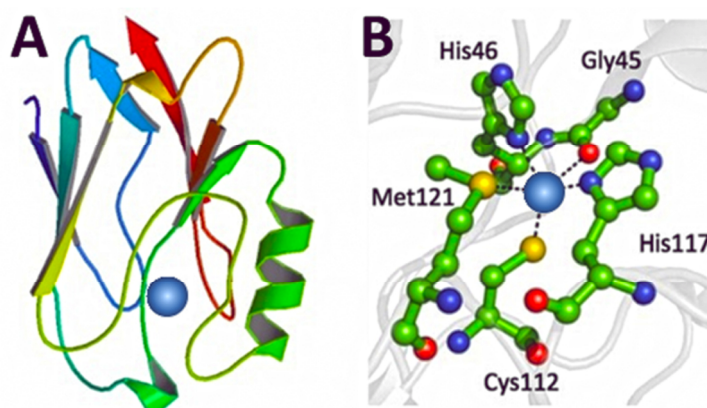


Figure 3.1. (A) Crystal structure of wt azurin by Nar et al. (28) (4AZU.pdb). Shown is a cartoon of the protein in ribbon representation. (B) The zoom shows the copper-binding site. The copper is shown as a blue sphere and the three strong ligands (His46, His117, Cys112) and 2 axial ligands (Met121, Gly45) are highlighted.

molecule-metal interface has been demonstrated by surface-enhanced Raman spectroscopy (26, 27).

In this chapter, we will show that individual electron transfer events under electrochemical control can be observed, and that the redox properties and thermodynamics of individual biomolecules can be accurately measured. The approach is based on the FluRedox method, described in Chapter 1, by which electron transfer events in redox proteins can be monitored by fluorescence detection which offers a dramatic increase in detection sensitivity. Proof of principle will be demonstrated by measurements on azurin.

Azurin is an electron-shuttling T1 type metalloprotein, with many interesting features which include applications in sensor technology and integration into nano-array devices (14, 29, 30). Azurin, from *Pseudomonas aeruginosa*, has a molecular weight of 14 kDa and contains one copper (Cu) ion which is the redox center that is located in the so-called northern region of the protein, buried in a hydrophobic patch at 7 Å distance from the surface (Figure 3.1A). The penta-coordinated Cu center, surrounded by its ligands His46, His117, Cys112, Met121 and Gly45, shows a distorted trigonal bipyramidal geometry (28) (Figure 3.1B).

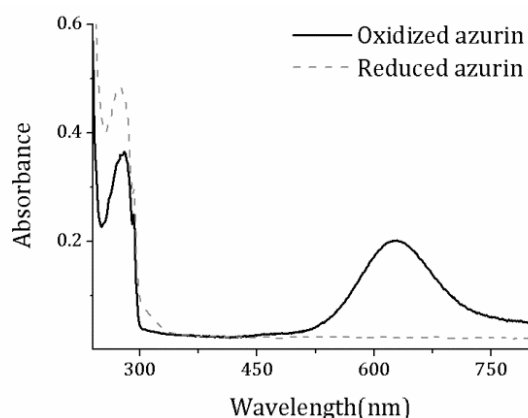


Figure 3.2. Absorption spectra of Cu-Az in its oxidized (solid line) and reduced (dash line) form. Az absorption spectrum was measured at room temperature on 50 μM of Az in 20 mM Hepes buffer solution. The absorption spectrum of oxidized Cu-Az shows two main peaks at 280 nm and 628 nm (Cu^{2+} absorption). Reduced Cu-Az shows only the 280 nm band.

The geometrical arrangement of ligands around the redox center affects the spectroscopic properties as well as the thermodynamic and kinetic features of azurin (31). Canters and coworkers, for example, rearranged the protein backbone by replacing His117 with glycine thus created a "hole" in the azurin coordination sphere. Addition of ligands such as imidazole rescues the T1 Cu center while anionic ligands induce a T2-character (32–34). ET reactions from azurin to its physiological partners occur through the aforementioned hydrophobic patch, along a pathway that involves His117 (33). Azurin in its oxidized state (Cu^{2+}) displays an intense ($\epsilon = 5700 \text{ M}^{-1}\text{cm}^{-1}$) ligand-to-metal-charge-transfer transition in the visible region of $\sim 600 \text{ nm}$ which gives rise to its fascinating blue color (35). Three strong ligands (His46, His117, Cys112) determine its main spectroscopic properties and are responsible for the very small Cu hyperfine coupling of T1 Cu contrary to T2 type proteins (36, 37). The optical absorption almost disappears when the protein is reduced to the Cu^+ state (see Figure 3.2).

In the so-called FluRedox principle, this spectroscopic feature of azurin has been combined with fluorescence resonance energy transfer (FRET) as a means to monitor redox changes of the Cu site (the energy acceptor) with an

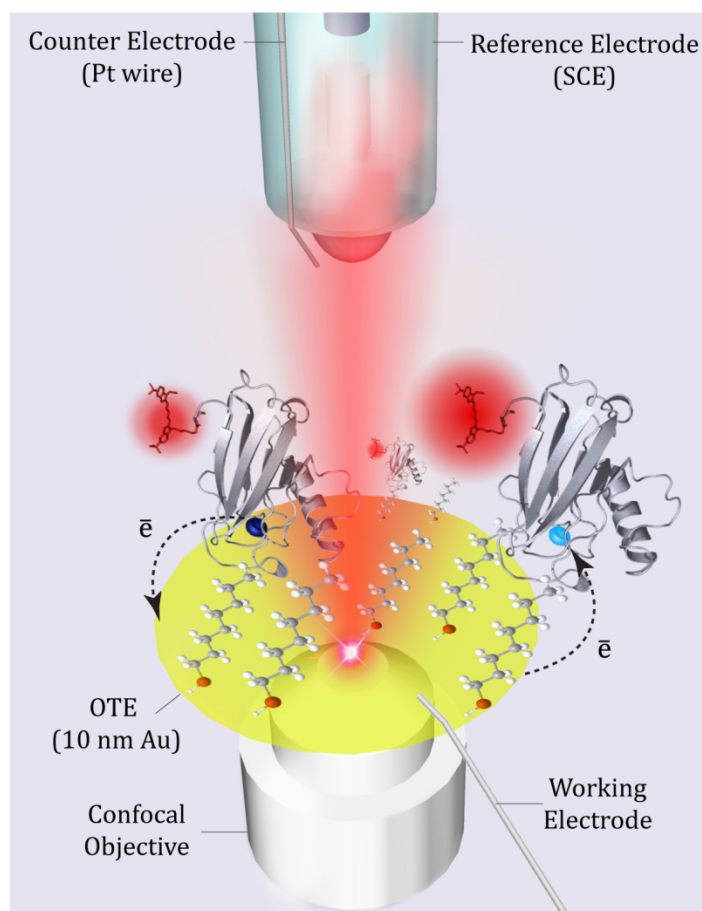


Figure 3.3. An artistic representation of the fluorescence electrochemistry assembly combined with a fluorescence microscopy. A reference electrode (SCE) and counter electrode (Pt wire) were inserted in the sample solution which was contained in a sealed holder with a glass cover slip at the bottom. The cover slip was coated with a 10-12 nm thick gold layer which functioned as the optically transparent working electrode (OTE). Azurin labeled with Cy5 is adsorbed on the self-assembled monolayer of octanethiol which was deposited on the gold film. Azurin molecules are oriented (by hydrophobic interaction) with the copper center facing the electrode surface. According to the FluRedox principle, fluorescence of the dye label is quenched when the protein is oxidized because of FRET from the attached fluorophore to the metal-cofactor (dark blue sphere). In the reduced form of the protein (light blue sphere), quenching does not occur and emission of the fluorophore is uninhibited.

externally tagged dye label (the fluorescent donor) (38–40). For this, the absorption band of the protein has to overlap with the emission band of the dye in the FRET pair. The FluRedox principle has been successfully applied in biosensor technology (41–43) and single molecule enzymology (44–46).

Earlier we demonstrated the feasibility of fluorescence-detected cyclic voltammetry (FCV), i.e. a combination of the FluRedox method with potentiostatic control of the redox state of fluorescently labeled azurin (40). Azurin was adsorbed on a thiolalkane monolayer deposited on an optically transparent gold film (40). FCV allowed us to reveal kinetic and thermodynamic heterogeneity of azurin at a detection limit of a few hundred protein molecules. A mathematically rigorous, modified Butler-Volmer theory (47) was used for the analysis of fluorescent-detected voltammograms. The midpoint potential determined with FCV spans a range of tens of millivolts which was attributed to micro-environmental variance, protein-substrate and protein-protein interactions, or local electric field effects on the metal cofactor buried in the metalloprotein. In addition, Patil and Davis (48) reported a stepwise decrease of the spread of the midpoint potential (from 17 mV to 12 mV) with increasing alkanethiol chain length (hexanethiol to dodecanethiol). They suggest that the inhomogeneity of the interfacial alkanethiol monolayer on the gold electrode contributes to the thermodynamic dispersion.

In a follow-up on these experiments, we have improved the detection sensitivity by switching to a confocal fluorescence microscope equipped with an avalanche photodiode detector, where before we used a wide-field fluorescence microscope with a CCD imaging detector. Because of the improved signal-to-noise ratio, we could readily achieve single-molecule sensitivity. We report in this chapter direct monitoring of redox-gated and voltage-controlled fluorescence switching of individual wt-azurin molecules tagged with Cy5 on an octanethiol-modified optically transparent gold (Au) electrode (OTE) as illustrated in Figure 3.3. We uncover the dispersion in midpoint potential of azurin by analysis of fluorescence-detected voltammograms of individual azurin molecules which are immobilized on a gold-surface. The results shown in this work constitute the first direct observation of single-molecule fluorescence-electrochemistry and of thermodynamic dispersion in a protein film by measuring one molecule at a time.

3.2 Experimental Section

3.2.1 Sample preparation

Wild type azurin from *Pseudomonas aeruginosa* was expressed in *E. coli* and purified as previously described (49). Protein labeling was performed using a modified version of a previously described protocol (39). In short, wt (Cu) Azurin was incubated in a molar ratio of 1:1 with the NHS-ester of the fluorescent label Cy5 (GE Healthcare, UK) in 20 mM HEPES buffer pH 8.3, for 2 hours at room temperature. Before labeling, the Cy5-NHS ester was dissolved in Dimethyl sulfoxide (DMSO) (Amersham Biosciences). Following the incubation step the unreacted label was removed using a 5 ml HiTrap desalting column (GE Healthcare). During the desalting step a buffer exchange to 5 mM TRIS/HCl at pH 8.5 was performed, required for the purification step (see below). To check for possible non-redox-dependent contributions to the fluorescence, zinc-reconstituted wt azurin was used as a control sample. This was purified and labeled in the same way as the native Cu azurin.

Purification step: labeling with the Cy5-NHS ester is not 100%, while the label can also attach to exposed lysines, although the N-terminus is assumed to be the preferred labeling site. To obtain a homogenous, 100% labeled sample, ion exchange chromatography (IEC) of the labeled protein species was performed on a 1 ml MonoQ column (GE Healthcare) using an Äkta Purifier (GE Healthcare) system (50). Before the labeled azurin fraction was loaded, the column was equilibrated with 5mM TRIS at pH 8.5. Subsequently, protein species were eluted with a gradient from 0 to 100 mM NaCl in 5mM TRIS pH 8.5 in 30 column volumes at a flow rate of 1 ml/min as recommended by the manufacturer. The elution process was followed by monitoring absorbance at 280 nm (azurin) and 650 nm (characteristic absorption of Cy5) (Figure 3.4A).

The fractions corresponding to each elution peak were then collected and checked by means of UV/Vis spectroscopy to confirm the presence of protein

(Figure 3.4B). Absorption spectra were measured using a Lambda 800 spectrophotometer (Perkin Elmer Inc., USA) with a slit width equivalent to a bandwidth of 2 nm.

3.2.2 Fluorescence time courses in bulk

To verify redox switching in bulk solution, reduction and oxidation of Cy5-labeled azurin was performed by adding reductant (dithiotreitol, DTT) and oxidant (potassium ferricyanide, $K_3(FeCN)_6$) from freshly prepared, concentrated stock solutions (2-20 mM) directly into an optical cuvette to a final concentration of 5-20 μ M, i.e. in 50 to 200-fold excess. In these experiments the fluorescence was monitored using a Cary Eclipse Spectrophotometer (Varian Inc., Agilent Technologies, USA). Fluorescence time courses of the labeled protein upon addition of oxidant or reductant were recorded by exciting the sample at 650 nm and monitoring the emission at 685 nm at room temperature in a 3-windows quartz ultra-micro cell with 100 μ l total sample volume (Hellma Analytics, Müllheim, Germany). In order to minimize second order diffraction effects of the monochromator gratings suitable optical filters were placed, both, in the excitation and the emission path. The excitation/emission slits were set to 5 nm band-pass. The concentration of labeled protein was 50-100 nM in 100 mM phosphate buffer solution at pH 7.0.

3.2.3 Azurin immobilization on gold

The working electrode was prepared in-house and consisted of a semi-transparent gold layer of about 10 nm thickness which was deposited on a microscope slide (1" diameter glass coverslip, thickness 0.14-0.17 mm (#1), Menzel). Prior to gold deposition all glass slides were sonicated in spectrometer grade acetone (45 min) and stored in methanol. In between these steps, the slides were thoroughly rinsed and sonicated in deionized water (MilliQ). Before use the cover slips were blow-dried under a gentle nitrogen flow and then

ozone-cleaned (UVP PR-100 UV-ozone photoreactor) for 1 h and used for gold coating immediately.

The thin gold films were prepared by RF sputtering (ATC 1800F, AJA International) according to the protocol described by van Baarle et al (51). Good adhesion of the gold layer to the glass was ensured by first sputtering a layer of Molybdenum-Germanium (MoGe) of ~ 2 nm thickness under 100% argon pressure. During subsequent gold sputtering, 5% partial oxygen pressure was added which helps to increase surface flatness (51).

The gold-coated slide was covered with a self-assembling monolayer (SAM) of 1-octanethiol (C8, for short) which serves as an intermediate layer. Freshly sputtered Au films were soaked overnight (15-18 h) in 1 mM solution of C8 in ethanol. A hydrophobic patch on the protein surface which is close to the azurin Cu center is believed to orient towards the hydrophobic alkanethiol head groups, leading to a favorable orientation for electron transfer (13, 16). The Cu lies only ~ 7 Å beneath the protein surface at this hydrophobic patch (28).

Before incubation with azurin, the alkane-thiol/gold coated slide was rinsed with ethanol, blown dry, rinsed with milliQ water and blown dry again. The dry SAM-coated slide was then turned into a working electrode. For the confocal experiments on wt azurin, about 300 μL of a 100 pM azurin solution was put on the modified Au electrode and left to incubate overnight at 4 °C. This gave reproducible results of specifically immobilized wt-azurin without protein aggregation at the surface. For the immobilization step, a degassed 10 mM *low-salt* potassium phosphate buffer ($\text{K}_3(\text{PO}_4)$) at pH 7 was used to minimize aggregation of azurin on the surface. After incubation, unbound azurin was removed by rinsing 4 or 5 times with fresh buffer. The pH 7 buffer which was used to cover the surface layer during the measurements had a potassium phosphate concentration of 100 mM. All the measurements were performed in anaerobic conditions in a sealed sample-holder under continuous argon flow.

3.2.4. Surface characterization

The roughness of the bare 10 nm semi-transparent Au layer and azurin adsorbed substrates was determined by tapping mode atomic force microscopy (AFM) with a Digital Instrument multimode microscope (Veeco) equipped with a Nanoscope IIIa controller. Cantilevers with a resonance frequency of 70 kHz and a spring constant of 2 N/m (Olympus Corp.) were used for ex-situ imaging of the functionalized gold surfaces. Before imaging, the substrates with adsorbed proteins were rinsed with protein-free buffer to ensure the removal of loosely bound proteins and then imaged dry. For image analysis, WSxM 4.0 Develop 12.4 (Nanotec Electronica S.L.) scanning probe microscopy software was used (52).

3.2.5. Fluorescent electrochemistry setup

Fluorescently labeled, immobilized wt azurin was monitored with a confocal microscopy setup for simultaneous electrochemical and fluorescence intensity measurements.

Single molecule imaging. The sample-scanning confocal microscope was equipped with Time-Correlated Single-Photon Counting (TCSPC) capabilities. For fluorescence excitation a pulsed picosecond diode laser with 40 MHz repetition rate (PDL 800-B, PicoQuant GmbH) with an output wavelength of 639 nm was sent through a narrow-band clean-up filter (LD01-640/8-25, Semrock, USA), coupled into a single-mode optical fiber, the output of which was collimated using a telescope system made of two achromatic lenses (+60 mm and +40 mm focal lengths, respectively). The collimated beam was directed into the back entrance of an Axiovert 100 microscope (Zeiss), reflected by a dichroic mirror (Z 532/633 M, Chroma technology, USA) to a high numerical aperture (NA) oil objective (100× oil, NA 1.4, Zeiss, Germany) and then focused to a diffraction-limited spot on the sample surface. Epi-fluorescence from the labeled azurin was filtered with an emission filter (D 675/50 M, Chroma technology, USA) and focused with a +80 mm focal length achromatic lens on to the active area of a

single photon avalanche photodiode (Perkin-Elmer SPCM-AQR-14). The data acquisition was performed by the TimeHarp 200 TCSPC PC-board (PicoQuant, GmbH) operating in the special Time-Tagged Time-Resolved (T3R) mode, which stores the arrival time of each individual photon event in a file that we refer to as a fluorescence time trace. Samples were mounted onto a Physik Instrumente P-517 nanopositioner. Scanning, accurate positioning, data collection were performed by the Picoquant SymPho-Time software (PicoQuant GmbH).

A 10 by 10 μm area of the thiolalkane SAM-modified gold surface, covered with sparsely distributed, Cy5-labeled single azurin molecules, was scanned with a step size of 100 nm and a dwell time of 2 ms per point. A characteristic fluorescence intensity image corresponding to such a region is shown in Figure 3.9A. After imaging, the coordinates of the molecules in a scanned area were registered and an automatic recording procedure was started. During this procedure the scanner successively moves each selected molecule into the laser focus and at each position a fluorescence time trace was recorded for a duration of up to 300 seconds as a function of experimental conditions. The data were further elaborated off-line.

Electrochemistry. Azurin was immobilized on the semi-transparent gold working electrode as described in section 3.2.4. The working electrode was connected via a copper wire to a potentiostat (CH Instruments, model Chi832b). The counter electrode, consisting of a Pt wire, and the saturated calomel (SCE) reference electrode (Radiometer Analytical/BASI) were inserted into the 5 mL volume of buffer solution (100 mM $\text{K}_3(\text{PO}_4)$ at pH 7.0) which covers the working electrode with the immobilized Cy5-azurin. Conventional staircase cyclic voltammetry (CV) was applied at scan rates of 10 mV/s to 5 V/s, scanning the applied potential from -0.10 to $+0.20$ V vs. SCE in potential steps of 1 mV. Alternatively, the chronoamperometric mode was used, in which a square potential waveform was applied, switching the potential between -0.10 to $+0.20$ V at a rate of 0.1 to 4 s^{-1} . The fluorescence rate of single, Cy5-labeled azurin

molecules was measured as a function of the applied potential, which results in a fluorescence-detected voltammogram.

The potential of the working electrode was recorded by one of the analog inputs of a data-acquisition (DAQ) card (National Instruments, PCI-MIO-16XE-10) which was connected to a microcomputer for control and for storing the data. A fluorescence time trace was recorded in synchrony with the potential scan. The two data files were processed by a home-written Labview application, which ties each photon emission event to a specific potential.

3.3 Results

3.3.1 Purification of Az-Cy5

We have purified azurin after labeling with Cy5 (NHS-ester) in order to get more homogenous species for the surface immobilization. The sample was fractionated using high resolution anion exchange chromatography (Figure 3.4A), recording both overall protein absorbance (280 nm) as well as the specific absorbance of Cy5 (650 nm). In the chromatographic separation we have observed multiple peaks because of the variety of labeling sites (exposed lysines) on the azurin surface. From the UV-vis spectral analysis of the eluting species (Figure 3.4B), one sees that fraction I shows the same spectrum as the oxidized azurin, which is, therefore, ascribed to unlabeled protein. In this case the band around 628 nm is solely due to the absorption of the Cu^{2+} center, the ratio $\text{Abs}_{628\text{nm}}/\text{Abs}_{280\text{nm}} \sim 0.57$ being the same as for the native, oxidized protein. The UV-vis spectra of fraction II-IV in Figure 3.4B display features of the protein as well as the label and are ascribed to singly labeled protein fractions. The spectra show an intense peak around 650 nm accompanied by a shoulder at 600 nm, which indicates the presence of label in the sample. The presence of protein is inferred from two spectral characteristics: the absorption at 280 nm and the

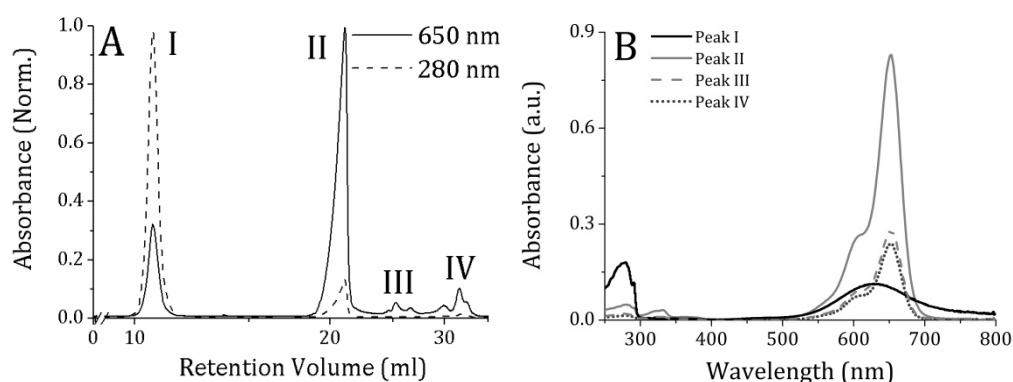


Figure 3.4. (A) Azurin was labeled with Cy5 and the resulting species were separated with anion exchange chromatography, recording both overall protein absorbance at 280 nm and the specific absorbance of the Cy5 label at 650 nm. (B) Display of the spectra corresponding to the peaks I-IV. The spectra of peak III and IV strongly overlap, and are almost indistinguishable. The absorbance spectrum of Peak I has the same shape as the UV-Vis absorption spectrum of wt Cu-azurin from *Ps. aeruginosa* in the oxidized form. The band around 628 nm in this case is attributed to the absorption of the Cu^{2+} center of unlabeled azurin in the sample, corroborated by the fact that the ratio $\text{Abs}_{628\text{nm}}/\text{Abs}_{280\text{nm}} \sim 0.57$ is the same as for wt azurin. The presence of protein is inferred from two spectral characteristics: the absorption at 280 nm and the typical sharp peak at 291 nm due to the only tryptophan in the sequence.

typical sharp peak at 291 nm due to the only tryptophan in the sequence. Since we got the highest concentration of the label in fraction II, we used this fraction in all the single molecule experiments. Thus, we avoided immobilization of unlabeled or heterogeneously labeled species.

3.3.2 Fluorescence switching ratio (SR) in bulk

It is very well known for all the type-1 Cu centres that, while an absorption band is present at 590-630 nm in the Cu^{2+} state, this band is absent in the Cu^+ state. Thus, one also expects to see a significant resonance energy transfer from the fluorophore to the Cu center in the oxidized but not in the reduced state of azurin. For instance in Figure 3.5 (black trace), upon initial addition of oxidant ($\text{K}_3(\text{FeCN})_6$), the fluorescence intensity drops due to FRET between the attached

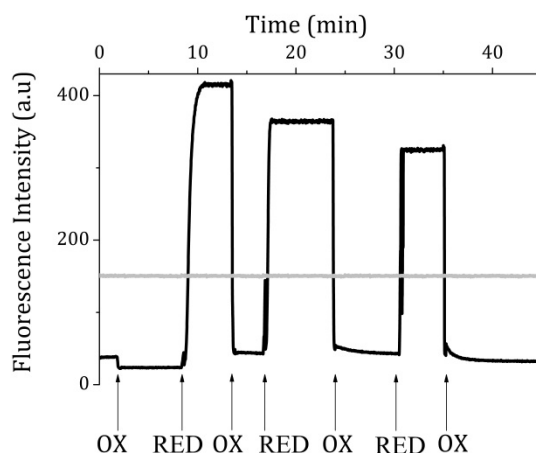


Figure 3.5. FRET-based on-off switching in bulk. A 100 nM Cy5-labeled Cu-azurin sample was titrated with aliquots of DTT and $K_3(FeCN)_6$ (2 mM) in 100 mM phosphate buffer at pH 7.0. We observed a large, reversible change of the fluorescence intensity of Cy5 labeled azurin upon addition of oxidant or reductant. The fluorescence intensity in the oxidized state is reduced by about a factor of 10 compared to that in the reduced state. Zn-azurin labeled with Cy5 (grey line) was used as a control and did not show any fluorescence switch.

fluorophore and the non-fluorescent Cu-center. Subsequent addition of reductant (DTT) produces an increase in the fluorescence intensity. In principle, this redox cycle can be repeated indefinitely as previously reported (38, 39). In fact, the fluorescence intensity in the oxidized state is reduced by about a factor of 10 compared to that in the reduced state in bulk. As a result, we obtained about 90% for the fluorescence switching ratio (SR) of Az-Cy5. The SR is defined as follows:

$$SR = \frac{I_{RED} - I_{OX}}{I_{RED}} \times 100 \quad (1)$$

where I_{RED} and I_{OX} are the fluorescence intensity values in the reduced bright and oxidized dark state, respectively. Furthermore, Zn-azurin (a redox inactive form of wt azurin, reconstituted with Zn instead of Cu) labeled with Cy5 was used as a control. It did not show any fluorescence switching upon addition of oxidant or reductant (grey trace in Figure 3.5).

3.3.3 Topography of Az-Cy5-functionalized thin Au film

For epifluorescent microscope imaging of labeled proteins immobilized on a gold surface it is necessary to use an ultrathin Au-film deposited on transparent substrates. We used optically transparent Au films at a thickness of about 10 nm which are homogeneous, very flat and conductive over the full area of the microscope slide (47, 53). These properties make them perfectly suitable for use as a working electrode in electrochemical studies in combination with simultaneous fluorescence detection in an epifluorescent microscope (see Figure 3.3).

To verify the topology of the surface, electrodes were imaged with AFM. A typical AFM image of the sputtered gold surface (10 nm thick) modified with an C8-SAM is shown in Figure 3.6A. The gold surface was polycrystalline, i.e. not atomically flat, but very homogeneous with a roughness of approximately 3 Å RMS over a range of tens of microns. This value is consistent with the previously reported roughness of the bare 10 nm gold film (47, 53).

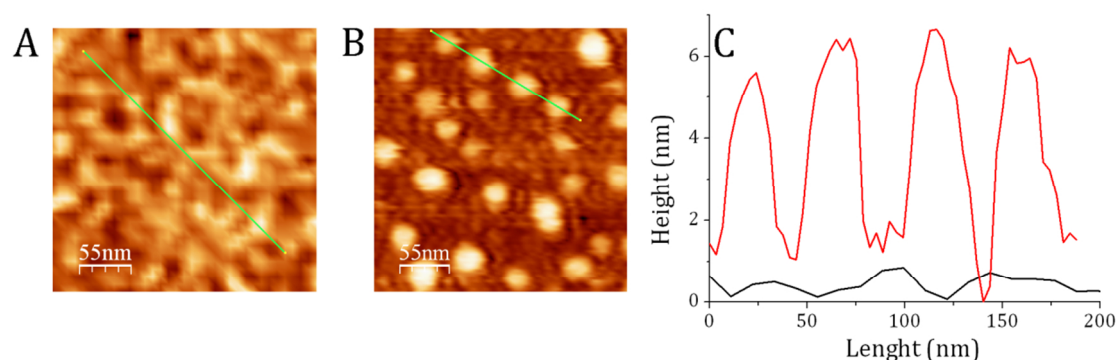


Figure 3.6. Tapping mode AFM images. A) octanethiol modified 10 nm semi-transparent Au surface. B) wt-azurin molecules immobilized on octanethiol modified 10 nm semi-transparent Au surface. SAM of octanethiol were formed during overnight incubation. A 10 nm thick gold layer, with MoGe attachment layer, was sputtered on a standard 1" microscope slide, thickness #1 (0.14–0.17 mm). C) Height profiles of the green lines in image A (black line) and image B (red line). Sections showed clear ~4 nm high features in image B, which indicates the presence of single azurin molecules adsorbed on the Au electrode.

A typical *ex-situ* tapping mode AFM image of Az-Cy5 adsorbed on an C8-SAM-covered Au film is shown in Figure 3.6B. The observed globular features that are clearly discerned in the AFM image indicate individual Az-Cy5 molecules adsorbed on the 1-octanethiol SAM-covered Au films. Section analysis in Figure 3.6C shows that these features are clearly distinguished from the background of SAM/Au substrate and are about 4 nm high which is the typical size (14, 53) of a single wt-azurin as determined by X-ray crystallography (28). The small height variations of the individual proteins across the Au film can be attributed, at least partially, to the small height variations of the underlying gold substrate (on the order of 0.1-0.3 nm). At the same time, the height and width distributions are relatively narrow which suggests the absence of aggregation and a uniform orientation with respect to the surface.

3.3.4 Electrochemical Measurements

Protein film voltammetry (PFV), developed by F. Armstrong and co-workers (10), is a method to observe direct electron transfer (DET) between redox proteins and electrodes. PFV can be achieved by immobilizing Az-Cy5 on an optically-transparent gold (~10 nm) electrode through adsorption on an intermediary C8-SAM (see in Figure 3.3; C8 is short-hand for 1-octanethiol). Adsorption of Az-Cy5 on the C8-SAM layer presumably occurs by hydrophobic interaction between the terminal methyl group of the SAM and the hydrophobic patch at the protein surface around the Cu-containing redox center. Previously, it has been shown that the rate constants for electron transfer between the electrode and the Cu center, across the alkanethiols, are significantly higher than of the protein in the direct adsorption mode (54). Thus, the molecular orientation of the azurin on the Au/alkanethiol surface is towards the aforementioned hydrophobic patch which is favorable for direct electrons transfer with the Cu center facing the electrode as illustrated in Figure 3.3).

Figure 3.7 shows typical cyclic voltammograms (CV) of wt azurin adsorbed on

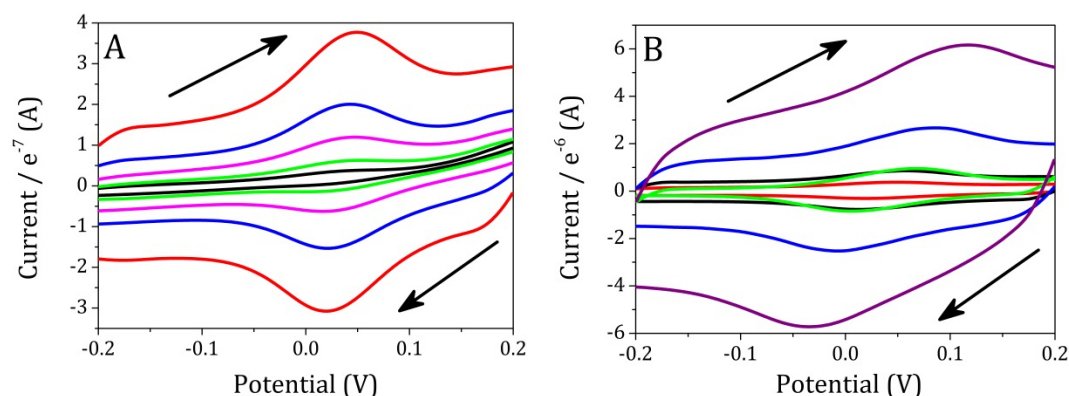


Figure 3.7. Typical background-subtracted cyclic voltammograms for wt azurin adsorbed on a semi-transparent gold electrode (working electrode, 10 nm) via an octanethiol SAM. Reference electrode SCE, counter electrode Pt gauze, electrolyte 100 mM phosphate buffer at pH 7.0. Incubation time for the 0.94 μM wt azurin labelled with Cy5 was 10 minutes. After rinsing the surface 5 times with the buffer, CV of immobilized protein was measured at a wide range of scan rates: A) 10-200 mV/s and B) 200-5000 mV/s (vs SCE). Arrows show the oxidation (forward) and reduction (reverse) cycles, respectively. Peak separation (ox-red) increases with scan rate.

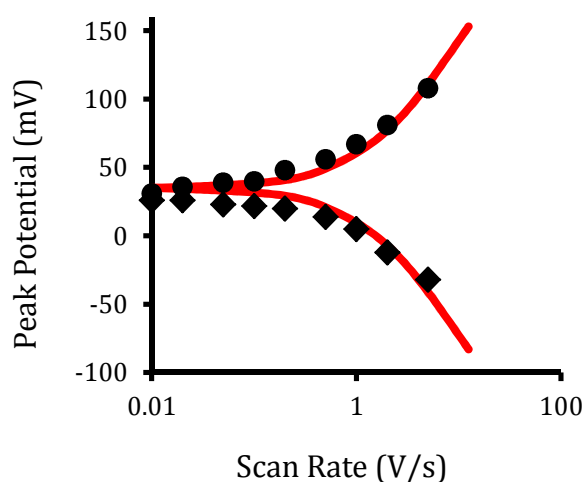


Figure 3.8. Trumpet plot showing the scan rate dependence of peak separation for CV. Sweep rates range between 10 and 1000 mV/s. CV peak potentials at the maximum for oxidative (round dots) and reductive (diamond) cycles were fitted (solid line) based on the Butler-Volmer theory (explained in chapter 2). The midpoint potential (35 mV vs SCE) was calculated from the trumpet plot fitting.

gold modified with the C8-SAM, at scan rates that range from 10 mV/s to 5000 mV/s. The CVs have the shape expected for an immobilized redox protein, with the reductive and oxidative peaks almost coinciding along the horizontal axis at slow scan rates. For an immobilised redox protein, the ability to observe electrocatalytic activity is a crucial indicator that the functionality of the protein has not been significantly perturbed by the electrode attachment. The electroactive coverage (Γ_{ea}) of azurin was calculated as 3.4 pmol cm⁻² as was determined from the anodic and cathodic charge of adsorbed protein:

$$\Gamma_{ea} = \frac{A}{nFvA_{RE}} \quad (2)$$

where A is the area of the observed CV peak, n is the number of electrons transferred ($n = 1$ for azurin), F is the Faraday constant, v is the potential scan rate and A_{RE} is the geometrical electrode area.

Figure 3.8 shows the resulting trumpet plot, in which the peak positions for oxidation and reduction potentials are plotted as a function of the logarithmic scan rate. This is a useful method of displaying and analyzing the characteristics of the PFV response over a wide time domain (13). Direct electron transfer of metalloproteins when immobilized on a conductive electrode can generate important information about their intrinsic thermodynamic, kinetic and mechanistic properties (10–12). At low scan rates, the potentials at the maximum of the oxidation and reduction peaks are close, and their average corresponds to the midpoint potential of the Cu site. As the scan rate increases, the oxidation and reduction peak potentials separate. Furthermore, the dashed lines in the trumpet plot show the Butler-Volmer based fit of the I-V curve (see chapter 2). As a result, the ET rate $k_0 = 26 \text{ s}^{-1}$ and the midpoint potential $E_0 = 35 \text{ mV vs SCE}$ as calculated from the trumpet plot fitting which corresponds well to previously reported data (47). Moreover, the surface coverage we obtained is consistent with a high retention of electroactivity on immobilization which is comparable with other results (47, 48, 53).

3.3.5 Fluorescence-electrochemistry on SM azurins

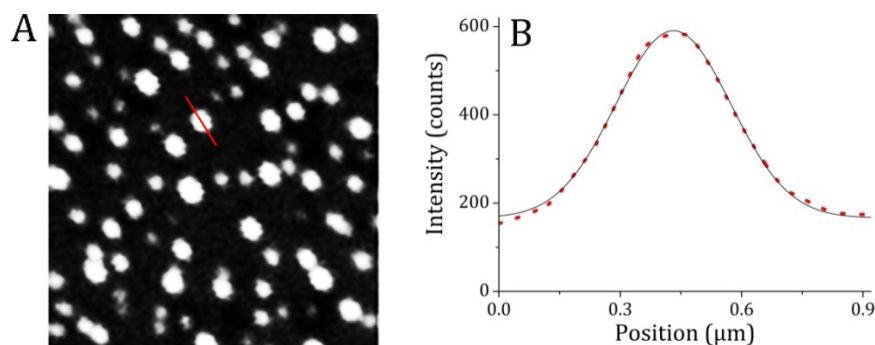


Figure 3.9. A) The fluorescence intensity image (left) of the individual azurin molecules immobilized on gold surface via 1-octanethiol SAM correspond to a region of $10 \times 10 \mu\text{m}^2$ with a dwell time of 2 ms per point. B) Intensity profile (red dots) taken along the center of a molecule (red line on the image) and fitted with a Gaussian (black solid line). The full-width-at-half-maximum (fwhm) is 335 nm, close to the diffraction limited resolution.

A typical fluorescence intensity image of individual azurin molecules is shown in Figure 3.9A. Wt azurin molecules labeled with Cy5 were immobilized on the gold electrode which is covered by a C8-SAM, as described above. The image shows a region of $10 \times 10 \mu\text{m}^2$ with a dwell time of 2 ms per point. An intensity profile taken along the center of a molecule in the image (red line in Fig. 3.9A) is shown in Figure 3.9B (red dots). The Gaussian fit of the intensity profile has a fwhm of 335 nm, very close to the diffraction-limited resolution (~ 280 nm) at the given excitation wavelength.

A reference electrode (standard calomel, SCE) and a counter electrode (a Pt wire) were inserted in the droplet of buffer solution that covered the functionalized gold layer which was configured as the working electrode. The three electrodes were wired to a potentiostat. The effect of the applied potential on the fluorescence of surface-immobilized, labeled azurin is shown in Figure 3.10A-D in which the working electrode is switched back and forth from a reducing potential (-0.2 V vs. SCE) to an oxidizing potential ($+0.2$ V). The bright-

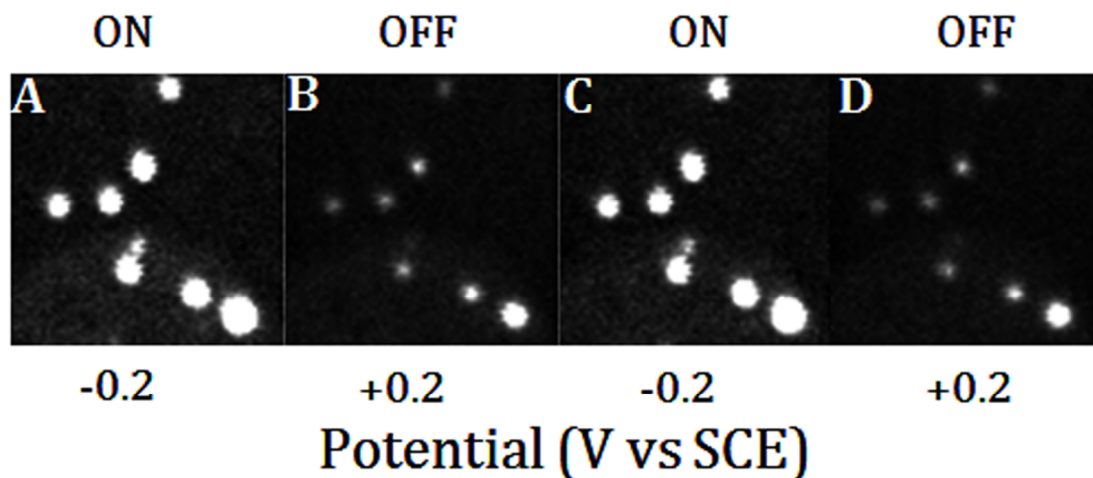


Figure 3.10. The fluorescence intensity images of the individual azurin molecules. SM azurins immobilized on gold surface via 1-octanethiol SAM, correspond to a region of $5 \times 5 \mu\text{m}^2$ with a dwell time of 2 ms per point. In images A and C, SM azurins were reduced by -0.2 V applied potential where the same molecules oxidized by $+0.2 \text{ V}$ (vs SCE) in images B and D.

ness of the spots in the image, which correspond to individual azurin molecules, varies by about a factor of 5 to 7: a high fluorescence intensity (ON) is observed in the reduced state, whereas it is weak (OFF) in the oxidized state. This is similar to what is observed in a bulk solution when labeled azurin is chemically oxidized and reduced (53) (See Discussion part for more details).

This ON/OFF switching behavior is more clearly demonstrated in Figure 3.11 by monitoring the fluorescence intensity of a single Cy5-azurin molecule as a function of time. This is achieved by adjusting the scanning stage to move and then hold one of the molecules in the focus of the laser beam. Subsequently, the fluorescence intensity (black, solid line) is monitored while the potential (black, dashed line) is switched in a square-wave pattern (so-called chronoamperometry, Fig. 3.11A) at a period of 5 s (54) or linearly swept in the forward and reverse directions at a scan rate of 100 mV/s (cyclic voltammetry, Fig. 3.11B). The data in Figure 3.11 show the fluorescence count rate with a bin-size of 10 ms, together with the applied voltage pattern (dashed line). The fluorescence time trace follows an on-off switching behavior which depends on

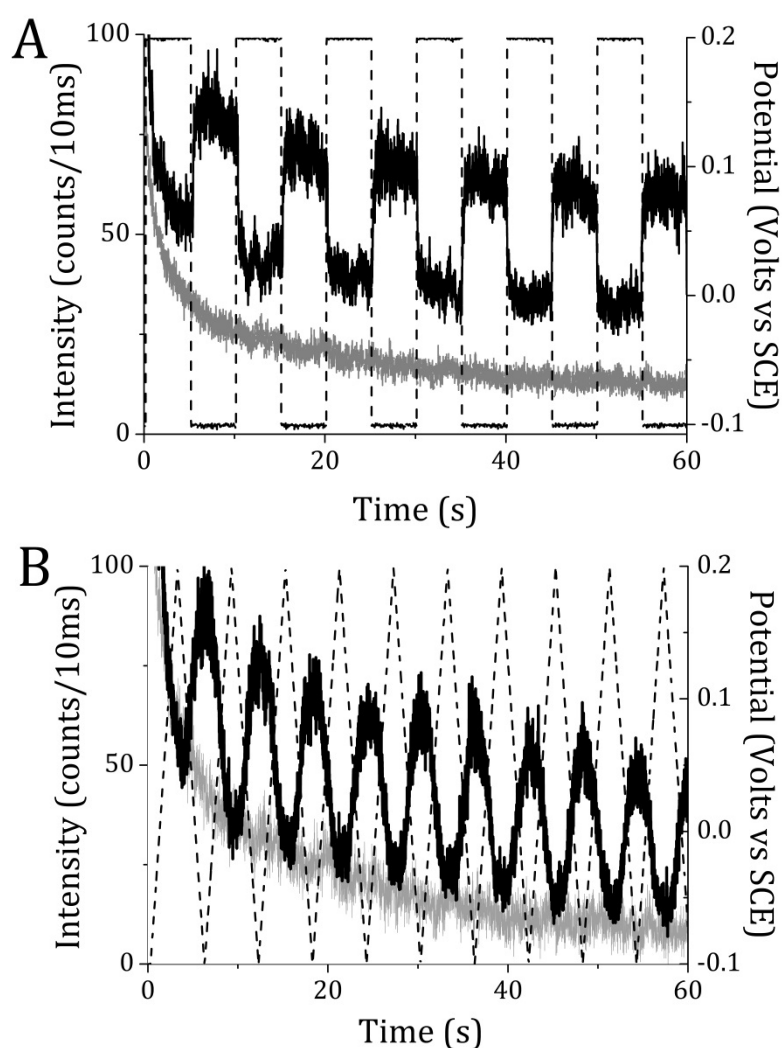


Figure 3.11. The real time fluorescence intensity time traces (10 ms bin size) showing FRET-gated emission of Cy5-labeled SM-Cu-Az (black, solid line) on an octanethiol-modified gold layer (10 nm) in response to an applied potential (black, dashed line). A) Chronoamperometric potential was cycled from 0.2 to -0.1 V with a 5 s pulse width. B) Cyclic voltammetry was applied at 100 mV/s scan rate. Counter electrode Pt gauze, electrolyte 100 mM phosphate buffer at pH 7.0. Zinc inactive form of the wild-type protein (grey line) was used as a control, and did not show any fluorescence switching with the same applied potential.

the applied potential. Fluorescently labeled zinc azurin, the redox inactive form of the wild-type protein, was used as a control. With zinc azurin no fluorescence switching was observed at the same applied potentials (grey line).

The more conventional method of cyclic voltammetry consists of ramping the potential up or down linearly in time. An example is shown in Figure 3.7, where amperometric detection is used to measure the current response of the azurin sample. The current has a maximum near the midpoint potential where the rate of the electrode reaction is largest, at least at slow scan rates when the electron transfer rate is not rate limiting. A similar result is obtained (see Fig. 3.11B) by monitoring the fluorescence intensity of labeled azurin on the working electrode as a function of the applied potential (similar to the measurements reported in Figs. 2.1, 2.2 and A.2.4.) In this case the shape of the curve will be sigmoidal since the fluorescence intensity follows the relative populations of the oxidized and reduced states (47, 48). The result of such a measurement is shown in more detail in Figure 3.12, which can be called an ‘‘optical voltammogram’’. It reflects the response of an individual azurin molecule, obtained by recording single electron transfer events. This is the first time that a fluorescent-detected voltammogram of a single redox protein has been obtained.

The relative population of the oxidized and the reduced state of the azurin is determined by a Boltzmann distribution. By fitting the fluorescence intensity (I) to a Boltzmann sigmoidal equation we can fit the fluorescence-detected voltammogram, and determine the midpoint potential (E_f^0) of an individual azurin. This will be equivalent to the potential at which the rate of change of the fluorescence intensity is maximum. Thus, by taking an average of optical peak potentials for a forward and backward sweep, the optical midpoint potential can be calculated as (48):

$$I = I_{min} + \frac{I_{max} - I_{min}}{1 + \exp\left(\frac{E - E_f^0}{d}\right)} \quad (3)$$

where I_{min} and I_{max} represents the fluorescence intensities when the protein is at the fully oxidized and reduced states, respectively, and $d = RT/F$. In fact, Equation 3 is just another representation of the Nernst equation (See Chapter

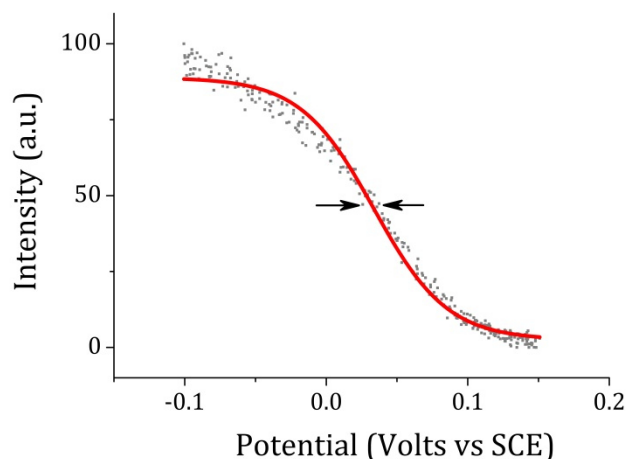


Figure 3.12. An optical voltammogram (dots) of an individual wt-azurin molecule for 100 mV/s scan rate in 100 mM phosphate buffer, pH 7.0 at room temperature. The red line represents the Boltzmann sigmoidal fit to the data according to Eq. (3). The optically determined midpoint potential (E_f^0) (arrows) is the calculated value from the sigmoidal fit ($E_f^0 = 33$ mV).

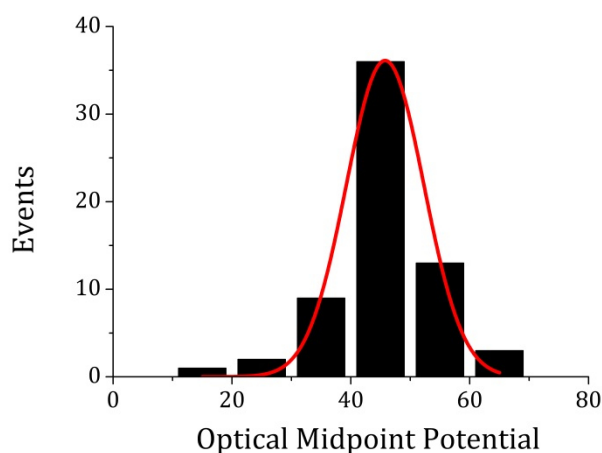


Figure 3.13. Histogram of optically determined midpoint potentials of 66 individual azurin molecules on an octanethiol-modified 10 nm Au at an applied potential (-0.1 to 0.15 V). The Gaussian fit is centered at 45.7 ± 0.5 mV with a fwhm of 15 mV.

1.4.1.2) with $n = 1$, where it is assumed that the increase in fluorescence intensity upon reduction is proportional to the concentration of reduced Cy5-azurin.

Figure 3.12 shows a typical optical voltammogram with the fit of the Boltzmann sigmoidal (red line) to the fluorescence intensity vs. applied potential. The optically determined midpoint potential (arrows) for this single azurin molecule is calculated as $E_f^0 = 33$ mV (vs SCE) from the sigmoidal fit, at which the rate of change of fluorescence is maximum.

The dispersion in the optically determined midpoint potential of 66 individual azurin molecules on C8-SAM-modified semi-transparent Au film is shown in Figure 3.13. The distribution of midpoint potentials was fitted to a Gaussian and gave a maximum value at 45.7 mV (± 0.5) with a fwhm of 15 mV (vs SCE).

3.4 Discussion

We have selectively immobilized individual, fluorescently labeled azurin molecules by stable adsorption on a self-assembled monolayer of thiolalkanes deposited on semi-transparent gold films (see Figure 3.3). This construct was incorporated as a functionalized working electrode in an electrochemical cell. It was shown that changes of the redox state of an individual azurin molecule by applying an external potential can be monitored in fluorescence using the FRET-based FluRedox principle (38–48, 53). This result implies a significant leap in sensitivity by which single-electron events at the working electrode can be monitored in real time with high time resolution.

It proved essential to include a purification step after labeling of azurin with the NHS-ester of the Cy5 dye molecule. It is generally assumed that the Cy5-NHS ester preferentially binds to the N-terminus at a pH of 8.3 (39). However, a recent, detailed mass-spectrometry analysis by Andreoni et al. (50) of Atto-655-labeled azurin has shown that this is not necessarily the case. A mixture of labeled species was obtained with the Atto-655-NHS ester, which included not only covalent binding of the label to the N-terminus, but also to lysines 24, 27, 122 and 128. Doubly labeled azurin molecules were also observed. This is problematic in single-molecule experiments, because the switching ratios of the

different azurin species differ significantly from one another. The analysis showed that Lys-122 was the preferred labeling position for the Atto-655-NHS ester at pH 8.3 (50) consistent with the nucleophilic character of this lysine residue.

Chromatographic purification of Cy5-labeled azurin also yielded a distribution of labeled species (see Fig. 3.4). The different species were not analysed further, and therefore it is not clear what the exact labeling positions are in this case. We have used peak II in Figure 3.4 for all the experiments described in this chapter. It turns out that this azurin-Cy5 species also has the largest switching ratio in solution of 90% (see Fig. 3.5). This is higher than values previously reported (40) but the latter were based on the average value of the mixture of azurin-Cy5 species immobilized on the gold electrode.

Cy5 is notorious not only for the role of the triplet state in the photophysical properties of this molecule, but also for conformational flexibility and its effect on their electronic structure (55, 56). It leads to pronounced blinking, and more importantly, an increased susceptibility for photobleaching. The presence of molecular oxygen, typically at a concentration of 0.5 mM (57) under ambient conditions in buffered solutions, has a large effect on the photostability of dye-molecules. Upon excitation, the dye molecule will every so often end up in the triplet state by intersystem crossing. Efficient energy transfer from the triplet state of the dye to molecular oxygen results in population of the O₂ singlet state which is highly reactive, and therefore -- directly or indirectly -- destructive of other molecular species in solution, including the fluorescent dye. Moreover, there is a possibility that the presence of oxygen will interfere with the electron transfer reactions at the electrode (25). For these reasons, the experiments were performed in a sealed container under oxygen-free conditions by purging the solution with argon beforehand, and by maintaining an argon flow over the solution during electrochemical measurements.

Under those conditions one would expect that the triplet life time of Cy5 and associated blinking events are extended into the ms-domain. This is, however, not observed. In control experiments with Cy5-labeled Zn-azurin, immobilized on a thiolalkane SAM-covered electrode, we do not observe any blinking at this time scale. Even more remarkable is the high photostability of the azurin-Cy5 construct under the conditions of the electrochemical measurements: photobleaching was virtually absent, and fluorescence time traces could readily be obtained for arbitrary duration. (For practical reasons, they were limited to several minutes.) This is in stark contrast with azurin-Cy5 immobilized on a gold (53) or glass surface (see Chapter 4) without potentiostatic control of the electrode potential, where time traces are limited to at most tens of seconds because of photobleaching, even under an argon atmosphere.

The absence of blinking (at least at ms-time scale and longer), and the strongly enhanced photostability of the azurin-Cy5 construct under conditions of cyclic voltammetry are observations that we cannot fully explain. It appears that the triplet state of the Cy5-label is strongly quenched. This could be due to interaction with the metal electrode, although the thickness of thiolalkane layer is probably too large for such a coupling. However, a local reorganization of the thiolalkane layer under cyclic voltammetry conditions might bring the azurin-Cy5 molecule in closer contact with the gold surface. An indication for such an effect is the gradual decrease of the fluorescence rate in the voltammetric time traces, superimposed on the electrochemically induced changes. This may be due to increased quenching of Cy5 fluorescence by the gold layer. This would be consistent with the fact that we observed a somewhat lower fluorescence switching ratio (60%, see Figures 3.10 and 3.11) of azurin-Cy5 upon electrochemical oxidation and reduction at the working electrode than with chemically-induced redox switching on glass (see Chapter 4). In the latter case the switching ratio is about 90%. Previously, Elmalk et al. (53) showed that K27C azurin immobilized on Au surface through the mixed SAMs depicts chemically-induced fluorescence intensity switching of about 70% which is similar to the

electrochemically obtained SR of single wt azurin molecules. Thus, the lower switching ratio may also signify partial quenching of Cy5 fluorescence by the gold layer.

The distribution of optically determined midpoint potentials (Figure 3.13) of single azurin molecules is centered at 45.7 ± 0.5 mV vs. SCE and the graphically determined width was found to be 15 mV. The average midpoint potential corresponds well with the value of 35 mV found using conventional CV (see Figures 3.7 and 3.8). The difference may be due to the higher packing density in the case of conventional CV, but could also be caused by small variations in the results of CV measurements, which are not uncommon.

The width of the distribution of midpoint potentials in Fig. 3.13 is in good agreement with the results obtained from the samples with high azurin surface coverage described in chapter 2 (see Figure 2.4). Moreover, the dispersion in the single-molecule data is also consistent with a recently published report by Patil and Davis (48) where a similar E_f^0 was calculated (~ 38 mV for about 1200 azurin molecules) with a fwhm of its distribution of 16 mV for wild-type azurin molecules tagged with Atto 655 and immobilized on a C8-SAM. The agreement among these different data sets suggest that the heterogeneity in ensembles of up to 1200 azurin molecules is the same as observed in the case of single molecules. This could mean that it is largely determined by the local environment at the scale of the region of interest (up to 600 x 600 nm) in chapter 2 and in ref. (48). It also follows that protein-protein interactions between azurin-molecules at the electrode surface have little effect on the observed midpoint potentials.

There are several parameters that can affect the reduction potential of copper proteins, such as electronic coupling, electric field drop or molecular orientation (58–61). The midpoint potential of azurin is particularly sensitive to outer sphere interactions which affect the redox site and its electronic structure through electrostatic interactions (59, 62, 63). It should be noted, however, that

the observed width of the midpoint potential distribution contains a thermal contribution as well, which is probably of the same order of magnitude (kT is about 25 meV at room temperature). The results in this chapter thus must be considered as an onset for a more detailed study of the heterogeneity in the azurin redox properties.

3.5 Conclusions

In this work, we have shown that it is indeed possible to control the redox state of individual wt azurin molecules immobilized on an electrode, by an applied voltage under potentiostatic control. The FRET-based electrochemical detection of individual azurin molecules reveals the heterogeneity of redox parameters in this system. It opens the door to more detailed studies of protein-electrode interactions. Apart from measurements of the midpoint potential, the dynamics of electron transfer processes at the electrode can be exposed by analysis of the switching dynamics in time-tagged fluorescence time traces.

References

1. Warren JJ, Ener ME, Vlček A, Winkler JR, and Gray HB. 2012. Electron hopping through proteins. *Coordination Chemistry Reviews* 256(21-22):2478–2487.
2. Khoshtariya DE, Dolidze TD, Shushanyan M, Davis KL, Waldeck DH, and Van Eldik R. 2010. Fundamental signatures of short- and long-range electron transfer for the blue copper protein azurin at Au/SAM junctions. *Proceedings of the National Academy of Sciences of the United States of America* 107(7):2757–62.
3. Chen F and Tao NJ. 2009. Electron transport in single molecules: from benzene to graphene. *Accounts of chemical research* 42(3):429–38.
4. Nitzan A and Ratner M a. 2003. Electron transport in molecular wire junctions. *Science (New York, N.Y.)* 300(5624):1384–9.
5. Dennison C. 2005. Investigating the structure and function of cupredoxins. *Coordination Chemistry Reviews* 249(24):3025–3054.
6. Vijgenboom E, Busch JE, and Canters GW. 1997. In vivo studies disprove an obligatory role of azurin in denitrification in *Pseudomonas aeruginosa* and show that *azu* expression is under control of *rpoS* and ANR. *Microbiology (Reading, England)* 143 (Pt 9(1 997):2853–63.
7. Fujita K, Nakamura N, and Ohno H. 2004. Mimicking protein-protein electron transfer: Voltammetry of *Pseudomonas aeruginosa* azurin and the *Thermus thermophilus* CuA domain

- at ω -derivatized self-assembled-monolayer gold electrodes. *Journal of the American Chemical Society* 126(4):13954–13961.
8. Jeuken LJC, McEvoy JP, and Armstrong F a. 2002. Insights into Gated Electron-Transfer Kinetics at the Electrode–Protein Interface: A Square Wave Voltammetry Study of the Blue Copper Protein Azurin. *The Journal of Physical Chemistry B* 106(9):2304–2313.
 9. Vargo ML, Gulka CP, Gerig JK, Manieri CM, Dattelbaum JD, Marks CB, Lawrence NT, Trawick ML, and Leopold MC. 2010. Distance dependence of electron transfer kinetics for azurin protein adsorbed to monolayer protected nanoparticle film assemblies. *Langmuir : the ACS journal of surfaces and colloids* 26(1):560–9.
 10. Armstrong FA, Heering HA, and Hirst J. 1997. Reaction of complex metalloproteins studied by protein-film voltammetry. *Chemical Society Reviews* 26(3):169. The Royal Society of Chemistry.
 11. Léger C, Elliott SJ, Hoke KR, Jeuken LJC, Jones AK, and Armstrong FA. 2003. Enzyme electrokinetics: using protein film voltammetry to investigate redox enzymes and their mechanisms. *Biochemistry* 42(29):8653–62. American Chemical Society.
 12. Wijma HJ, Jeuken LJC, Verbeet MP, Armstrong FA, and Canters GW. 2007. Protein film voltammetry of copper-containing nitrite reductase reveals reversible inactivation. *Journal of the American Chemical Society* 129(27):8557–65. American Chemical Society.
 13. Jeuken LJC and Armstrong FA. 2001. Electrochemical Origin of Hysteresis in the Electron-Transfer Reactions of Adsorbed Proteins: Contrasting Behavior of the “ Blue ” Copper Protein , Azurin , Adsorbed on Pyrolytic Graphite and Modified Gold Electrodes. *Journal of Physical Chemistry B* 105:5271–5282.
 14. Alessandrini A, Salerno M, Frabboni S, and Facci P. 2005. Single-metalloprotein wet biotransistor. *Applied Physics Letters* 86(13):133902.
 15. Zhang J, Kuznetsov AM, Medvedev IG, Chi Q, Albrecht T, Jensen PS, and Ulstrup J. 2008. Single-molecule electron transfer in electrochemical environments. *Chemical reviews* 108(7):2737–91.
 16. Chi Q, Farver O, and Ulstrup J. 2005. Long-range protein electron transfer observed at the single-molecule level: In situ mapping of redox-gated tunneling resonance. *Proceedings of the National Academy of Sciences of the United States of America* 102(45):16203–8.
 17. Artés JM, Díez-Pérez I, Sanz F, and Gorostiza P. 2011. Direct Measurement of Electron Transfer Distance Decay Constants of Single Redox Proteins by Electrochemical Tunneling Spectroscopy. *ACS Nano* 5(3):2060–2066. American Chemical Society.
 18. Heller I, Kong J, Heering HA, Williams KA, Lemay SG, and Dekker C. 2005. Individual single-walled carbon nanotubes as nanoelectrodes for electrochemistry. *Nano letters* 5(1):137–42. American Chemical Society.
 19. Lemay SG, Kang S, Mathwig K, and Singh PS. 2013. Single-molecule electrochemistry: present status and outlook. *Accounts of chemical research* 46(2):369–77. American Chemical Society.
 20. Powell H V, Schnippering M, Cheung M, Macpherson J V, Mackenzie SR, Stavros VG, and Unwin PR. 2010. Probing redox reactions of immobilized cytochrome c using evanescent wave cavity ring-down spectroscopy in a thin-layer electrochemical cell. *Chemphyschem : a European journal of chemical physics and physical chemistry* 11(13):2985–91.
 21. Ashur I, Schulz O, McIntosh CL, Pinkas I, Ros R, and Jones AK. 2012. Transparent gold as a platform for adsorbed protein spectroelectrochemistry: investigation of cytochrome c and azurin. *Langmuir : the ACS journal of surfaces and colloids* 28(13):5861–71.
 22. Whitaker G, Belogay E, and Smith E. 2007. Spectroelectrochemical Determination of the Redox Potential of Cytochrome c via Multiple Regression. *fau.edu*:1–27.

23. Clair CS, Ellis W, and Gray H. 1992. Spectroelectrochemistry of blue copper proteins: pH and temperature dependences of the reduction potentials of five azurins. *Inorganica chimica acta* 191:149–155.
24. Krzemiński Ł, Ndamba L, Canters GW, Aartsma TJ, Evans SD, and Jeuken LJC. 2011. Spectroelectrochemical investigation of intramolecular and interfacial electron-transfer rates reveals differences between nitrite reductase at rest and during turnover. *Journal of the American Chemical Society* 133(38):15085–93.
25. Ash P a and Vincent KA. 2012. Spectroscopic analysis of immobilised redox enzymes under direct electrochemical control. *Chemical communications (Cambridge, England)* 48(10):1400–9. The Royal Society of Chemistry.
26. Wang Y, Sevinc PC, He Y, and Lu HP. 2011. Probing ground-state single-electron self-exchange across a molecule-metal interface. *Journal of the American Chemical Society* 133(18):6989–96. American Chemical Society.
27. Cortés E, Etchegoin PG, Le Ru EC, Fainstein A, Vela ME, and Salvarezza RC. 2010. Monitoring the electrochemistry of single molecules by surface-enhanced Raman spectroscopy. *Journal of the American Chemical Society* 132(51):18034–7.
28. Nar H, Messerschmidt A, Huber R, Van de Kamp M, and Canters GW. 1991. Crystal structure analysis of oxidized *Pseudomonas aeruginosa* azurin at pH 5.5 and pH 9.0. A pH-induced conformational transition involves a peptide bond flip. *Journal of Molecular Biology* 221(3):765–72.
29. Choi J-W, Oh B-K, Kim YJ, and Min J. 2007. Protein-based biomemory device consisting of the cysteine-modified azurin. *Applied Physics Letters* 91(26):263902.
30. Rinaldi R, Biasco a., Maruccio G, Arima V, Visconti P, Cingolani R, Facci P, et al. 2003. Electronic rectification in protein devices. *Applied Physics Letters* 82(3):472.
31. Wilson TD, Yu Y, and Lu Y. 2012. Understanding copper-thiolate containing electron transfer centers by incorporation of unnatural amino acids and the CuA center into the type 1 copper protein azurin. *Coordination Chemistry Reviews* 257(1):1–17.
32. Den Blaauwen T and Canters GW. 1993. Creation of type-1 and type-2 copper sites by addition of exogenous ligands to the *Pseudomonas aeruginosa* azurin His117Gly mutant. *Journal of the American Chemical Society* 115(3):1121–1129. American Chemical Society.
33. Jeuken L and Vliet P Van. 2000. the surface-exposed and copper-coordinating histidine in blue copper proteins: The electron-transfer and redox-coupled ligand binding properties of His117Gly azurin. *Journal of the American Chemical Society*(11):12186–12194.
34. Alagaratnam S, Meeuwenoord NJ, Navarro JA, Hervás M, De la Rosa MA, Hoffmann M, Einsle O, Ubbink M, and Canters GW. 2011. Probing the reactivity of different forms of azurin by flavin photoreduction. *The FEBS journal* 278(9):1506–21.
35. Solomon E and Hare J. 1980. Spectroscopic studies of stellacyanin, plastocyanin, and azurin. Electronic structure of the blue copper sites. *Journal of the American Chemical Society* 102(1):168–178.
36. Garner DK, Vaughan MD, Hwang HJ, Savelieff MG, Berry SM, Honek JF, and Lu Y. 2006. Reduction potential tuning of the blue copper center in *Pseudomonas aeruginosa* azurin by the axial methionine as probed by unnatural amino acids. *Journal of the American Chemical Society* 128(49):15608–17. American Chemical Society.
37. Yanagisawa S and Dennison C. 2005. Reduction potential tuning at a type 1 copper site does not compromise electron transfer reactivity. *Journal of the American Chemical Society* 127(47):16453–9. American Chemical Society.

38. Schmauder R, Alagaratnam S, Chan C, Schmidt T, Canters GW, and Aartsma TJ. 2005. Sensitive detection of the redox state of copper proteins using fluorescence. *Journal of biological inorganic chemistry: JBIC: a publication of the Society of Biological Inorganic Chemistry* 10(6):683–7.
39. Kuznetsova S, Zauner G, Schmauder R, Mayboroda O a, Deelder AM, Aartsma TJ, and Canters GW. 2006. A Förster-resonance-energy transfer-based method for fluorescence detection of the protein redox state. *Analytical biochemistry* 350(1):52–60.
40. Davis JJ, Burgess H, Zauner G, Kuznetsova S, Salverda J, Aartsma T, and Canters GW. 2006. Monitoring interfacial bioelectrochemistry using a FRET switch. *The journal of physical chemistry. B* 110(41):20649–54.
41. Zauner G, Lonardi E, Bubacco L, Aartsma TJ, Canters GW, and Tepper AWJW. 2007. Tryptophan-to-dye fluorescence energy transfer applied to oxygen sensing by using type-3 copper proteins. *Chemistry-A European Journal* 13(25):7085–90.
42. Gustiananda M, Andreoni A, Tabares LC, Tepper AWJW, Fortunato L, Aartsma TJ, and Canters GW. 2012. Sensitive detection of histamine using fluorescently labeled oxido-reductases. *Biosensors & Bioelectronics* 31(1):419–25.
43. Strianese M, Zauner G, Tepper AWJW, Bubacco L, Breukink E, Aartsma TJ, Canters GW, and Tabares LC. 2009. A protein-based oxygen biosensor for high-throughput monitoring of cell growth and cell viability. *Analytical biochemistry* 385(2):242–8. Elsevier Inc.
44. Kuznetsova S, Zauner G, Aartsma TJ, Engelkamp H, Hatzakis N, Rowan AE, Nolte RJM, Christianen PCM, and Canters GW. 2008. The enzyme mechanism of nitrite reductase studied at single-molecule level. *Proceedings of the National Academy of Sciences of the United States of America* 105(9):3250–5.
45. Goldsmith RH, Tabares LC, Kostrz D, Dennison C, Aartsma TJ, Canters GW, and Moerner WE. 2011. Redox cycling and kinetic analysis of single molecules of solution-phase nitrite reductase. *Proceedings of the National Academy of Sciences of the United States of America* 108(42):17269–74.
46. Tabares LC, Kostrz D, Elmalk A, Andreoni A, Dennison C, Aartsma TJ, and Canters GW. 2011. Fluorescence lifetime analysis of nitrite reductase from *Alcaligenes xylosoxidans* at the single-molecule level reveals the enzyme mechanism. *Chemistry A European Journal* 17(43):12015–9.
47. Salverda JM, Patil A V., Mizzon G, Kuznetsova S, Zauner G, Akkilic N, Canters GW, Davis JJ, Heering HA, and Aartsma TJ. 2010. Fluorescent cyclic voltammetry of immobilized azurin: direct observation of thermodynamic and kinetic heterogeneity. *Angewandte Chemie (International ed. in English)* 49(33):5912–5915.
48. Patil AV and Davis JJ. 2010. Visualizing and tuning thermodynamic dispersion in metalloprotein monolayers. *Journal of the American Chemical Society* 132(47):16938–44. American Chemical Society.
49. Van de Kamp M, Hali FC, Rosato N, Agro a F, and Canters GW. 1990. Purification and characterization of a non-reconstitutable azurin, obtained by heterologous expression of the *Pseudomonas aeruginosa* *azu* gene in *Escherichia coli*. *Biochimica et biophysica acta* 1019(3):283–92.
50. Nicolardi S, Andreoni A, Tabares LC, Van der Burgt YEM, Canters GW, Deelder AM, and Hensbergen PJ. 2012. Top-down FTICR MS for the identification of fluorescent labeling efficiency and specificity of the Cu-protein azurin. *Analytical chemistry* 84(5):2512–20.
51. Van Baarle GJC, Troianovski a. M, Nishizaki T, Kes PH, and Aarts J. 2003. Imaging of vortex configurations in thin films by scanning-tunneling microscopy. *Applied Physics Letters* 82(7):1081.

52. Horcas I, Fernández R, Gómez-Rodríguez JM, Colchero J, Gómez-Herrero J, and Baro AM. 2007. WSXM: a software for scanning probe microscopy and a tool for nanotechnology. *The Review of scientific instruments* 78(1):013705.
53. Elmalk AT, Salverda JM, Tabares LC, Canters GW, and Aartsma TJ. 2012. Probing redox proteins on a gold surface by single molecule fluorescence spectroscopy. *The Journal of chemical physics* 136(23):235101.
54. Chi Q and Zhang J. 2001. Ordered assembly and controlled electron transfer of the blue copper protein azurin at gold (111) single-crystal substrates. *Journal of Physical Chemistry B* 105(111):4669–4679.
55. Levitus M and Ranjit S. Cyanine dyes in biophysical research: the photophysics of polymethine fluorescent dyes in biomolecular environments. *Quarterly Reviews of Biophysics* 44(01):123–151.
56. Ha T and Tinnefeld P. 2012. Photophysics of fluorescent probes for single-molecule biophysics and super-resolution imaging. *Annual review of physical chemistry* 63:595–617.
57. Reynafarje B, Costa LE, and Lehninger AL. 1985. O₂ solubility in aqueous media determined by a kinetic method. *Analytical Biochemistry* 145(2):406–418.
58. Hadt RG, Sun N, Marshall NM, Hodgson KO, Hedman B, Lu Y, and Solomon EI. 2012. Spectroscopic and DFT studies of second-sphere variants of the type 1 copper site in azurin: covalent and nonlocal electrostatic contributions to reduction potentials. *Journal of the American Chemical Society* 134(40):16701–16. American Chemical Society.
59. Warren JJ, Lancaster KM, Richards JH, and Gray HB. 2012. Inner- and outer-sphere metal coordination in blue copper proteins. *Journal of inorganic biochemistry* 115(null):119–26.
60. Cascella M, Magistrato A, Tavernelli I, Carloni P, and Rothlisberger U. 2006. Role of protein frame and solvent for the redox properties of azurin from *Pseudomonas aeruginosa*. *Proceedings of the National Academy of Sciences of the United States of America* 103(52):19641–6.
61. Lu Y, Yeung N, Sieracki N, and Marshall NM. 2009. Design of functional metalloproteins. *Nature* 460(7257):855–62.
62. Machczynski MC, Gray HB, and Richards JH. 2002. An outer-sphere hydrogen-bond network constrains copper coordination in blue proteins. *Journal of Inorganic Biochemistry* 88(3-4):375–380.
63. Lancaster KM, Sproules S, Palmer JH, Richards JH, and Gray HB. 2010. Outer-sphere effects on reduction potentials of copper sites in proteins: the curious case of high potential type 2 C112D/M121E *Pseudomonas aeruginosa* azurin. *Journal of the American Chemical Society* 132(41):14590–5. American Chemical Society.

Chapter 4

Chemically-induced redox switching of single azurin molecules[#]

[#] Namik Akkiliç, Fenna van der Grint, Gerard W. Canters, Thijs J. Aartsma (2013). to be submitted.

Abstract

We use an optical method for the detection of the redox state of proteins based on excited state energy transfer (FRET) from an attached dye molecule to the protein redox center. This method is applied to azurin, a 14 kDa type I blue copper protein. We show that the fluorescence intensity of a single azurin molecule as a function of time, i.e. the fluorescence time-trace, shows an on-off switching behavior which depends on the redox conditions in solution. We observed a reversible change of the fluorescence intensity of Cy5 labeled azurin upon addition of oxidant or reductant: The fluorescence intensity in the oxidized state decreases by about a factor of 10 compared to that in the reduced state. Fluorescence lifetimes of surface-immobilized azurin were found to be 0.7 ± 0.15 and 1.8 ± 0.2 ns in the oxidized (fluorescence off) and the reduced states (on), respectively. Finally, using change point (CP) analyses of the fluorescence time traces from individual azurin molecules, we were able to measure their reaction kinetics and redox parameters as a function of the chemical redox potential in solution. As a result, to the best of our knowledge for the first time, we were able to determine the midpoint potential (E_0) of a single redox protein. We observed a significant heterogeneity in reaction kinetics and redox thermodynamics at the single molecule level.

4.1 Introduction

An overwhelming number of chemical reactions in nature, both in the living cell and in the inanimate world are redox reactions. When two compounds engage in such a reaction, one will be reduced, the other oxidized. Redox reactions play a major role in almost all metabolic pathways, as well as in the chemical and biochemical cycles that operate in the environment. The study of biological electron transfer (ET) reactions of proteins is not only crucial for our knowledge of many physiological functions such as cellular respiration, photosynthesis, and redox homeostasis (1, 2), but also for potential applications in biotechnology which drives the current proliferation of research on biofuel cells, protein biochips and biosensors (3, 4). The ability to monitor redox reactions of proteins and enzymes with high sensitivity is scientifically and commercially of great importance. Greatly enhanced sensitivity and specificity can be achieved with the FluRedox method (see chapter 1) by which redox turn-over can be monitored down to the single-molecule level, breaking new ground in redox enzymology.

As single-molecule techniques developed over the past two decades, their potential for the investigation of the reaction dynamics of proteins and enzymes was recognized early on (5): reaction mechanisms and associated kinetic models can be unraveled in unprecedented detail. Instead of monitoring the concentration change of the substrate or the product to measure the reaction rate, a single-molecule experiment follows individual catalytic turnovers in real time and records the waiting times (τ) for completing individual reactions (5–7). Single-molecule kinetic theories have been developed to explore underlying reaction mechanisms and the associated kinetic models by analysing probability distributions and statistical properties of the waiting time parameters (8, 9). In one of the first experiments of Förster resonance energy transfer (FRET) at the single molecule level, Szabo *et al.* (10) demonstrated how to extract info from two-state single-molecule time trajectories which opened new doors in biomolecular research.

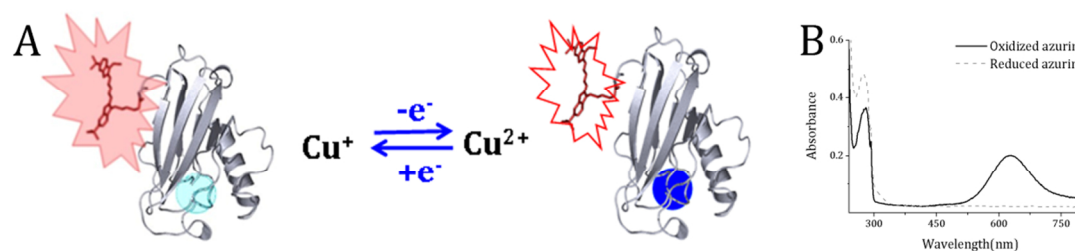


Figure 4.1. (A) Model of Cy5-NHS labeled wt azurin based on the crystal structure of wt azurin by Nar et al. [1] (4AZU.pdb). The covalently attached Cy5 label is excited at a wavelength close to its extinction maximum, λ_{ex} . In the reduced form of the protein the Cy5 relaxes by the conventional route, with emission of a photon at a characteristic wavelength, λ_{em} . In the oxidized form of the protein a FRET process can occur between the excited Cy5 label and the copper redox center (blue sphere), resulting in loss of fluorescence emission. (B) Absorption spectra of Cu-Az in its reduced (dash line) and oxidized (solid line) form. The absorption spectra were measured at room temperature, with 50 μM of Az in 20 mM Hepes buffer solution. The absorption spectrum of oxidized Cu-Az shows two main peaks at 280 nm and 628 nm (Cu^{2+} absorption). Reduced Cu-Az shows only the 280 nm band.

The observation of single electron transfer reactions will show the time-dependence of the redox properties of an individual protein, the distribution of redox properties over several proteins, and heterogeneity in the interaction with reaction partners. None of these important issues can be investigated equally well with existing ensemble methods. By combining the FluRedox method with potentiostatic or electrochemical control, we can relate the fluctuations of the fluorescence intensity to the exact conditions and properties of individual redox proteins and enzymes.

We have applied the FluRedox principle to study the chemically-induced redox switching of individual azurin molecules. Azurin (Figure 4.1A), from the pathogenic bacteria *Pseudomonas aeruginosa*, belongs to the family of T1 type redox proteins that contains a mononuclear Cu-site (11, 12) in which two histidines (H46 and H117), one cysteine (C312), and one methionine (M121) coordinate to the Cu-ion in a distorted tetrahedral manner (13–15). Azurin is a blue Cu protein with a mass of 14.6 kDa, which is common as an electron shuttle in ET chains of plants and bacteria, and is believed to play a role in oxidative

stress response (16). The hydrophobic patch around His117 at the protein surface, close to the redox-active site, is believed to mediate the formation of electron-transfer complexes (17). It has been shown that azurin can exchange electrons *in vitro* with cytochrome c551, nitrite reductase, and several dehydrogenases, although its physiological partner has not yet been identified (16–21). Importantly, azurin has been reported to selectively induce and trigger apoptosis in several human cancer cells, most probably by stabilizing p53 (22, 23). Moreover, azurin can serve as a highly sensitive amperometric biosensor for the detection of superoxide radical that can be used to understand radical reactions at cellular level (24).

In its oxidized (Cu^{2+}) form, this protein has an intense absorption band in the visible region of 600 nm ($\epsilon = 5700 \text{ M}^{-1}\text{cm}^{-1}$) that corresponds to a charge-transfer transition involving mainly the $d_{x^2-y^2}$ orbital of Cu^{2+} and a 3p orbital of the sulfur atom of Cys112 (Figure 4.1B). This absorption disappears when the molecular orbital in the d^{10} configuration of Cu^+ is filled, thus when the Cu site is reduced (25, 26). Previously, it has been demonstrated that this spectroscopic feature can be used to monitor the redox states of a protein with an attached fluorophore based on FRET, the so called “FluRedox principle” (25, 27), as illustrated in Figure 4.1A. Notably, fluorescence detection is highly selective with unmatched sensitivity, features that are very promising for biosensor applications (28–30). Most importantly, the enhanced sensitivity opens the doors for single-molecule detection of redox turn-over of proteins and enzymes (31–35). Recently, it was shown that the FluRedox principle can be combined with electrochemistry (36, 37), by which kinetic and thermodynamic heterogeneity of azurin on gold electrodes was investigated with a detection sensitivity as low as 100 protein molecules (38).

Herein, we report direct monitoring of electron transfer of single, fluorescently labeled azurin molecules covalently attached to a glass substrate, one electron at a time. We obtained continuous on-off switching of fluorescence, i.e. the

temporal fluorescence intensity profile, from the azurin construct under anoxygenic conditions, which depends on the chemical redox potential in solution. Control experiments show that, this switching behavior is directly correlated with the redox state of the Cu-center in the azurin molecule. Using change point analyses (39) of the time traces we were able to measure the reaction kinetics and redox parameters of individual azurin molecules as a function of the chemical redox potential in solution. As a result, we were able to determine redox chemical behavior one molecule at a time, offering for the first time the distribution of key electron transfer parameters, such as the midpoint potential (E_0) and reaction kinetics (k_{red} and k_{ox}) of the redox protein immobilized on a passive surface. We observed a significant heterogeneity in these parameters, in the lifetimes of oxidized and reduced azurin (τ_{ox} and τ_{red} , respectively), and in the switching ratio (SR) of individual azurin molecules.

4.2 Experimental Section

4.2.1 Azurin Purification and Labeling

Wild type azurin from *Pseudomonas aeruginosa* was expressed in *E. coli* and purified as previously described (40). Cells from *E. coli* JM109 were transformed using a pUC-derived plasmid containing the azurin gene (41) followed by a signal peptide for periplasmic translocation. After culturing, cells were harvested and resuspended in a solution of 20% (w/v) sucrose in 30 mM Tris/HCl, pH 8.0, containing 1 mM EDTA for 20 min at room temperature. Subsequently, the solution was centrifuged at 8000 rpm for 15 min, and the supernatant was collected (sucrose fraction). The cells were resuspended in Milli-Q water at 4 °C, stirred for 20 min, and centrifuged at 8000 rpm for 15 min. The supernatant was collected and added to the above obtained sucrose fraction while the pellet was discarded. In *E. coli*, azurin is normally expressed in its apo-form. Therefore, after cells were lysed, copper sulfate was slowly added to the medium, to a final concentration of 600 μM in order to incorporate Cu in the polypeptide matrix.

Potassium ferricyanide was added to the solution to a final concentration of 100 μM to produce an oxidizing environment. A stepwise precipitation step was included by lowering the pH of the solution to pH 4 by adding concentrated acetic acid. The precipitated proteins were removed by centrifugation (8000 rpm, 20 min). The resulting clarified solution containing azurin was loaded on a home-packed CM Sepharose Fast Flow (Amersham Biosciences) column, and elution was performed using a pH gradient from pH 4 to pH 6.9 (50 mM ammonium acetate). Fractions containing azurin were collected and, after buffer exchange and reduction with sodium dithionite, loaded onto a home-packed DEAE Sepharose Fast Flow (Amersham Biosciences) column and eluted using a salt gradient from 0 to 50 mM of NaCl in 5mM Tris/HCl at pH 8.5. After a buffer exchange and oxidation using 1 mM potassium ferricyanide, azurin-containing fractions were loaded on a 5 ml HiTrap SP column (GE Healthcare) and eluted using a pH gradient of pH 4 to pH 6.9 (50 mM ammonium acetate). All the chromatographic steps were performed on an Äkta Purifier system (GE Healthcare). The purification process was monitored by checking the purity of the protein after each chromatographic step on SDS-PAGE and by means of UV/VIS spectroscopy (Cary 50 spectrophotometer, Varian Inc., Agilent Technologies, USA). The final product, after the last cation exchange column, appeared on an SDS-PAGE gel as a single band with apparent mass of ~ 14 kDa and showed an UV/Vis spectrum with a ratio $\text{Abs}_{628\text{nm}}/\text{Abs}_{280\text{nm}}$ of ~ 0.57 which indicates full loading of the Cu-site (40).

Protein labeling was performed using a slightly modified version of a previously described protocol (27). Azurin was incubated in a molar ratio of 1:1 with the NHS-ester of the fluorescent label Cy5 (GE Healthcare, UK) in 20 mM HEPES buffer pH 8.3, for 2 hours. The unreacted label was then removed using a 5 ml HiTrap Desalting column (GE Healthcare). During the desalting step a buffer exchange to 5 mM Tris/HCl pH 8.5 was performed before the purification step described in the next section.

4.2.2 Purification of labeled species

Ion exchange chromatography (IEC) of the labeled protein species was performed on a 1 ml MonoQ column (GE Healthcare) using an Äkta Purifier (GE Healthcare) system (42). The labeled azurin fraction was loaded on the column (equilibrated with 5mM Tris pH 8.5) and subsequently protein species were eluted with a gradient from 0 to 100 mM NaCl in 5mM Tris pH 8.5 in 30 column volumes at a flow rate of 1 ml/min as recommended by the manufacturer. The elution process was followed by monitoring the absorbance at 280 nm (azurin) and 650 nm (characteristic absorption of Cy5) as shown in Figure 4.2A. The fractions corresponding to each peak were then collected and checked by means of UV/Vis spectroscopy to confirm the presence of protein (Figure 4.2B).

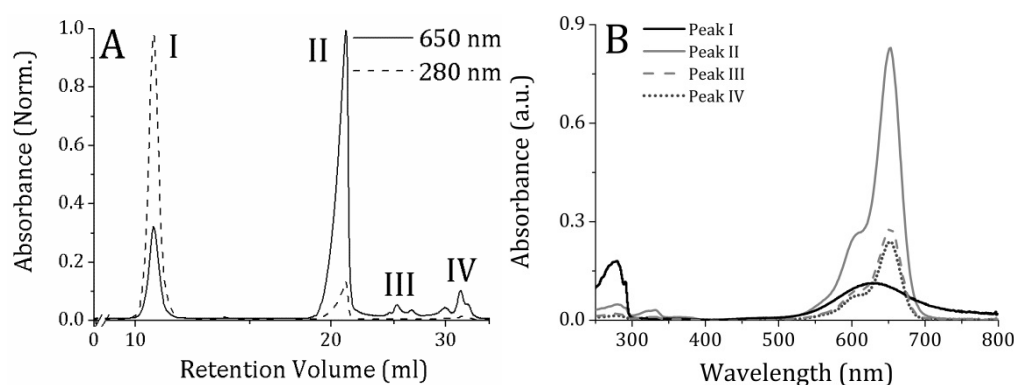


Figure 4.2. (A) Azurin was labeled with Cy5 and the resulting species were separated with anion exchange chromatography, recording both overall protein absorbance at 280 nm and the specific absorbance of the Cy5 label at 650 nm. (B) Display of the spectra corresponding to the peaks I-IV. The spectra of peaks III and IV strongly overlap, and are almost indistinguishable. The absorbance spectrum of Peak I has the same shape as the UV-Vis absorption spectrum of wt Cu-azurin from *Ps. aeruginosa* in the oxidized form, and is attributed to unlabeled azurin (confirmed by the ratio Abs_{628nm}/Abs_{280nm} of ~ 0.57 , typical of wt azurin) The presence of protein is inferred from two spectral characteristics: the absorption at 280 nm and the typical sharp peak at 291 nm due to the only tryptophan in the sequence.

4.2.3 Absorption and Fluorescence Spectroscopy

Absorption spectra were measured using a Perkin Elmer Instruments Lambda 800 spectrophotometer with a slit width equivalent to a bandwidth of 2 nm. Fluorescence spectra and time courses in bulk were measured with an LS 55 commercial fluorimeter (Perkin Elmer, USA), with a red sensitive photomultiplier (R928, Hamamatsu, Japan), set to 5 nm band pass. Cy5 fluorescence was excited at 645 nm, and the fluorescence intensity at 665 nm was used for the analysis of the FRET efficiency.

To verify redox changes in bulk solution, fluorescence time courses were measured in a 5x5 mm quartz cuvette (Perkin Elmer) in 100 mM phosphate buffer at pH 7.0 buffer solution. The concentration of the Cy5 labeled protein was 100 nM. Protein reduction and oxidation during measurement was performed by adding reductants (dithiothreitol, DTT) and oxidant (potassium ferricyanide, $K_3(FeCN)_6$) from freshly prepared concentrated stock solutions (2-20 mM) directly into the cuvette to a final concentration of 5-20 μ M, i.e. in 50 to 200-fold excess.

4.2.4 Azurin immobilization on glass

All glass slides were MENZEL GLÄSER Nr. 1 (Gerhard Menzel GmbH, Germany) which were cleaned by sonication in spectrometer grade acetone (45 min), then dipped in 10% NaOH/H₂O (45 min) and finally stored in methanol. Between each step, the slides were thoroughly rinsed and sonicated in deionized water (MilliQ). Before use the cover slips were blow dried under N₂ flow and ozone-cleaned (UVP PR-100 UV-ozone photoreactor) for 1 h immediately before silanization.

The surface of the cleaned glass slides was modified by depositing a layer of a 4:1 mixture of triethoxysilane (TES) and mercaptopropyl trimethoxysilane (MPTS) as described previously (32). All the silanes were purchased from Fluka and used

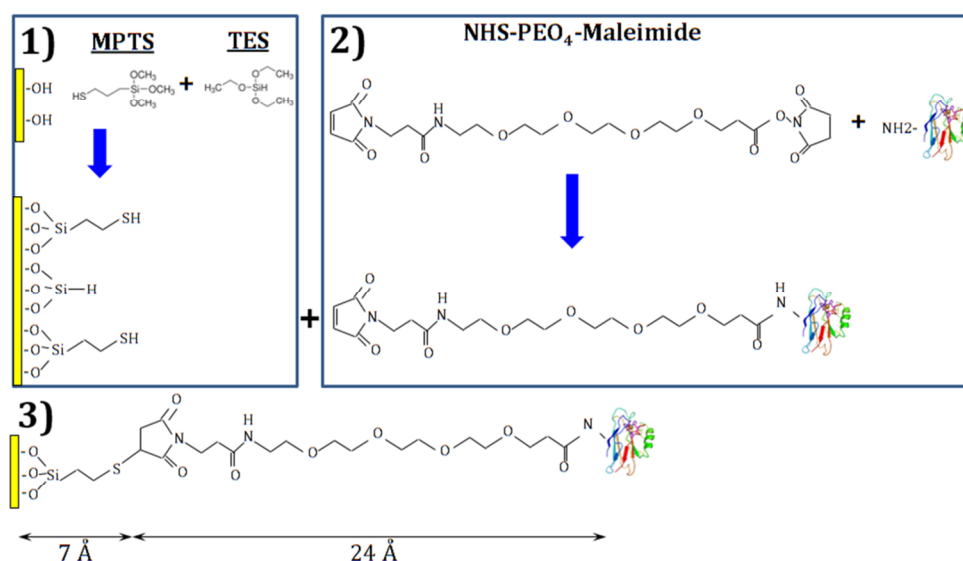


Figure 4.3. Protein immobilization in 3 steps: In step 1, glass slides were modified by depositing a layer of a 4:1 mixture of TES/MPTS with -SH groups exposed at the surface. Separately, in step 2, the NHS-PEO₄-maleimide linker is covalently bound to wt-azurin. Finally, the maleimide-end of the latter construct is attached to the exposed thiols at the silanized glass surface via the 24 Å long linker. The overall length of the linkers between the surface and the protein is about 31 Å.

without purification. In the second step, wt-azurin was covalently bound through the succinimidyl-[(N-maleimidopropionamido)-hexaethyleneglycol] ester) (NHS-PEO₄-maleimide, Pierce) to the modified glass slides (see Figure 4.3). Following the instructions from the manufacturer, the NHS-PEO₄-maleimide linker was added in a 100-fold excess of the protein, followed by a reaction time of 1 hour. The excess of the linker was then removed using a Centriscin-10 size exclusion column with a 5-kDa cut-off (Princeton Separations, Adelphia, NJ, USA) (32). Finally, 100 pM of NHS-PEO₄-maleimide-modified azurin was incubated on the silanized glass slide overnight at 4 °C and then rinsed with 10 mM potassium phosphate buffer at pH 7.0 to remove free azurin. This gave reproducible results of specifically immobilized individual, Cy5-labeled azurin molecules on the glass surface. The steps to functionalize the glass surface are summarized in Figure 4.3.

4.2.5 Single molecule imaging setup and single photon counting

The single molecule fluorescence measurements were conducted on a home-built sample scanning confocal microscope (Figure 4.4). The scanning confocal microscope was equipped with Time-Correlated Single-Photon Counting (TCSPC) capabilities. For fluorescence excitation a pulsed picosecond diode laser with 40 MHz repetition rate (PDL 800-B, PicoQuant GmbH) and an output wavelength of 639 nm was sent through a narrow-band clean-up filter (LD01-640/8-25, Semrock, USA), then coupled into a single-mode optical fiber, the output of which was collimated using a telescope system made of two achromatic lenses (+60 mm and +40 mm). The collimated beam was directed into the back entrance of an Axiovert 100 microscope (Zeiss), reflected by a dichroic mirror (Z 532/633 M, Chroma technology, USA) to a high numerical aperture (NA) oil objective (100 \times oil, NA 1.4, Zeiss, Germany) and then focused to a diffraction-limited spot (\sim 300 nm) on the sample surface. A power density of \sim 0.4 kW/cm² was used at the sample to avoid excessive bleaching while recording fluorescence time traces. Epi-fluorescence from the labeled azurin was filtered with an emission filter (D 675/50 M, Chroma technology, USA) and focused with a +80 mm focal length achromatic lens on to the active area of an avalanche photodiode (Perkin-Elmer SPCM-AQR-14). The data acquisition was performed by the TimeHarp 200 TCSPC PC-board (PicoQuant, GmbH) operating in the special Time-Tagged Time-Resolved (T3R) mode, which stores the arrival time of each individual photon event. Samples were mounted onto a P-517 nanopositioner which was connected to a E-71 control unit, both from Physik Instrumente GmbH. Scanning, accurate positioning, data collection and lifetime analysis were performed by the SymPhoTime software package (PicoQuant GmbH).

Fluorescence images were acquired by scanning a 10 \times 10 μ m² area of the sample on the glass surface with a step size of 100 nm and a dwell time of 2 ms per point. A characteristic fluorescence lifetime image (FLIM) is shown in Figure 4.5. After imaging, the molecules in the scanned area were manually selected and

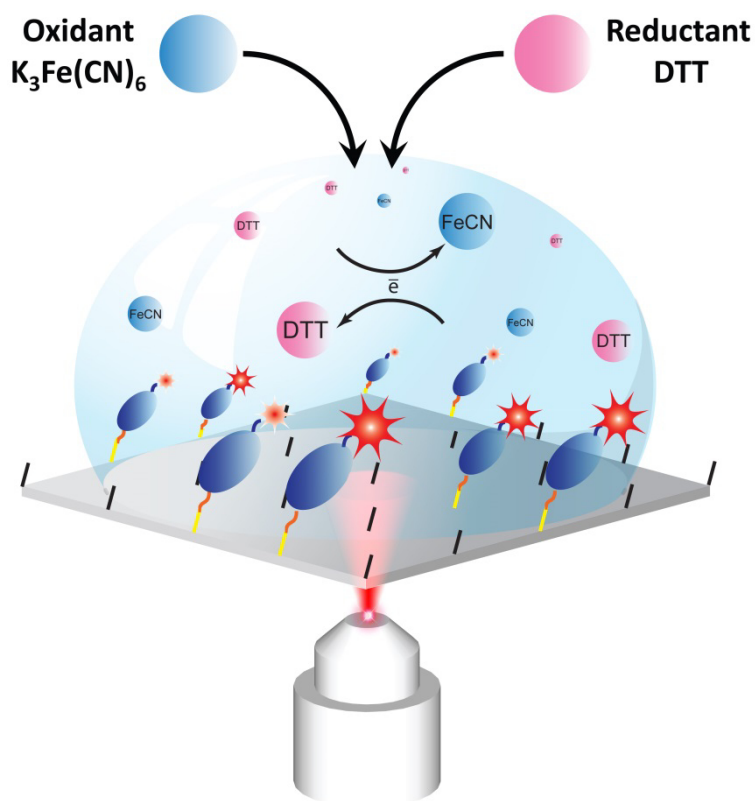


Figure 4.4. Single molecule fluorescence detection of azurin/Cy5 molecules. The redox state of the surface-immobilized protein was monitored using a mixture of DTT and $K_3(FeCN)_6$ as reductant and oxidant in the buffer solution. The redox potential of the solution was determined with a reference electrode (SCE) and counter electrode (platinum wire) connected to a voltmeter. The Az/Cy5-linker (orange curve, NHS-PEO4-maleimide) was covalently attached to the MPTS (yellow line)/TES (black line) covered glass surface (see section 4.2.4 for details).

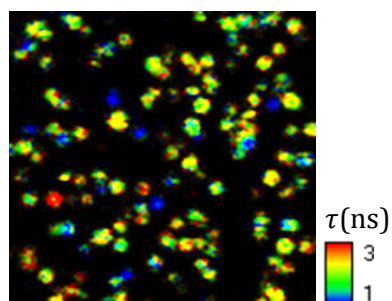


Figure 4.5. The fluorescence lifetime image ($10 \times 10 \mu m^2$) of immobilized azurin-Cy5 on a glass surface with a dwell time of 2 ms per pixel. The image contains, both, oxidized and reduced azurin in the presence of $200 \mu M K_3(FeCN)_6$ and $100 \mu M$ DTT in the buffer solution.

an automatic recording procedure was started. During this procedure the scanner was moved successively to each selected spot and the fluorescence time trace was recorded over a time interval of up to 120 seconds before moving on to the next spot until all the selected spots had been processed. The fluorescence recorded from each single molecule was stored in a file to be further elaborated off-line.

4.2.6 Redox potential of buffer solution

Single molecule detection was performed in 100 mM phosphate buffer solution at pH 7.0 with freshly prepared $K_3[Fe(CN)_6]$ and DTT as oxidant and reductant (Figure 4.4), respectively. The chemical redox potential of the buffer solution (E) in single molecule experiments was varied around the midpoint potential of azurin by adjusting the relative concentration of $K_3[Fe(CN)_6]$ and DTT. The initial concentration of the $K_3[Fe(CN)_6]$ was 200 μ M in all cases and DTT was added to reach the final potentials of -20, 0, 20, 40, 60, 80 and 100 mV. The potential of the solution was measured with a voltmeter (Fluke 111) using a saturated calomel electrode (SCE) as a reference (RE) and 0.5 mm platinum wire as a counter electrode (CE). The experiments were performed in a sealed container under oxygen-free conditions by purging the solution with argon beforehand, and by maintaining an argon flow over the solution during fluorescence measurements.

4.2.7 Data elaboration and analysis

The files containing the time-tagged time-resolved data were converted to ASCII format, and processed using a changepoint-finding algorithm implemented in software which was kindly provided by Dr. Haw Yang, Princeton University (39). The changepoint-finding algorithm was run using a parameter value of $\alpha = 0.01$ for Type I errors (false positive) and a confidence parameter value of $\beta = 0.95$ to set the confidence interval around each change point. In essence, the changepoint-finding software performs a statistical analysis of the fluorescence time traces to determine the points where a change in the fluorescence intensity

occurs without making any prior assumptions. Furthermore, the software clusters the intensities in up to 5 different levels using an expectation-maximization algorithm and determines the most likely number of states for modeling the system, using a Bayesian information criterion (BIC) (39). The output of the changepoint-finding algorithm was further elaborated by using a home written algorithm to determine the time intervals associated with the oxidized and the reduced state, respectively. Only traces longer than 0.5 second and showing at least 2 transitions between different states (fluorescence on and off) were taken into account for further analysis. The in-bulk switching ratio was used as a threshold criterion to discriminate on-times (above the threshold) and off-times (below the threshold). In particular, the condition for a state change was imposed such that the intensity ratio before and after fell within ± 2.5 standard deviations of the in-bulk switching ratio (90% confidence interval around the mean). Intensity drops to the background level due to blinking events were distinguished by assuming that the intensity of the oxidized state is at least a factor of 1.2 higher than the background level. Such blinking events were not counted as state changes. The on and off times from the selected single molecules were stored and subsequently analyzed. Data analysis was performed using custom-written algorithms in Matlab 7.9.

Histograms of the on- and off-times were built using a bin size of 1 ms. Fitting of the on- and off-times histogram was performed with a mono-exponential function defined as follows:

$$y = y_0 e^{-kx} \quad (1)$$

where x is the time bin number and y is its occurrence. The fitted parameters are: y_0 , the y value at time zero and k , the rate constant of the decay. According to which distribution was fitted, an “on” or “off” subscript was added to k , corresponding to the reduced and oxidized state of azurin, respectively, to distinguish the two parameters.

The parameter \bar{P}_{ox} (\bar{P}_{red}) is used in the present work to describe the time-averaged probability that the molecule is in the oxidized (reduced) state (33).

The value of \bar{P}_{ox} for each time trace was calculated as follows:

$$\bar{P}_{\text{ox}} = \frac{\sum_{i=1}^n \tau_{i,\text{off}}}{\sum_{i=1}^n \tau_{i,\text{off}} + \sum_{j=1}^m \tau_{j,\text{on}}} \quad (2)$$

where $\tau_{i,\text{off}}$ and $\tau_{j,\text{on}}$ are the i -th off- and j -th on-times, respectively; n and m are the total number of off- and on-time intervals in a single trace, respectively. A similar expression is used to calculate \bar{P}_{red} . The denominator is essentially the total duration of the time trace (before bleaching).

4.3 Redox thermodynamics of single molecules

The Nernst equation

The electrode potential of a redox couple in solution, i.e. the free energy when referenced against a standard hydrogen electrode, is given by the Nernst equation in terms of the concentrations of reductant and oxidant ($[red]$ and $[ox]$, respectively),

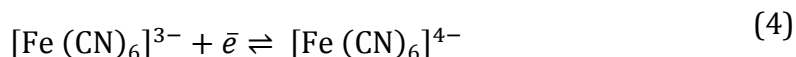
$$E = E_0 - \frac{RT}{nF} \ln \frac{[red]}{[ox]} \quad (3)$$

Here, R is the universal gas constant ($R = 8.314\,472\text{ J K}^{-1}\text{ mol}^{-1}$), T is the absolute temperature, and E_0 is the midpoint potential of the reaction. F is the Faraday constant ($F = 9.648\,53399 \times 10^4\text{ C mol}^{-1}$), and n corresponds to the number of electrons that are transferred in the reaction ($n = 1$ for azurin).

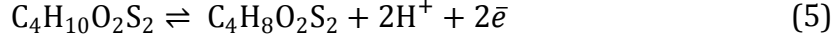
Redox system

In our experiments, we have a system consisting of three redox couples:

- Ferricyanide and ferrocyanide, ($E_{0, \text{FeCN}} = 116\text{ mV}$ at pH7, vs. SCE):



- DTT (dithiothreitol) and oxidized DTT, ($E_{0,DTT} = -574$ mV at pH7, vs. SCE) (43)):



- Oxidized azurin (Az_{ox}) and reduced azurin (Az_{red}), ($E_{0,Az} = 21 \pm 19$ mV at pH7, vs SCE (44)):



At equilibrium, we have the following expression for the redox potential of the system, according to the Nernst equation:

$$E = E_{0,FeCN} - \frac{RT}{F} \ln \frac{[Fe(CN)_6]^{3-}}{[Fe(CN)_6]^{4-}} = E_{0,DTT} - \frac{RT}{2F} \ln \frac{[DTT_{red}]}{[DTT_{ox}]} \quad (7)$$

Thus the redox potential can be calculated if we know the total concentrations of ferri- and ferrocyanide or of oxidized and reduced DTT.

The next treatment follows the theory as developed in Ref. (45). Depending on the redox conditions in the sample, an individual azurin molecule will continually switch between the oxidized and the reduced state at a rate which is determined by the concentrations of oxidizing and reducing species. We can evoke the ergodicity principle to formulate the Nernst equation in terms of the population distribution over time in such a two-state model (45).

The energy difference, ΔE , that is associated with the electron transfer reaction of azurin (Eq. 6), in the presence of the working electrode at a potential E is given by:

$$\Delta E = ne\Delta V = ne(E_0 - E) \quad (8)$$

Here, e is the elementary charge, and n is the number of electrons involved in the reaction, *i.e.* the charge transferred in the reaction is ne . Assuming that the time-averaged probabilities for the oxidized and reduced state of azurin, \bar{P}_{ox} and \bar{P}_{red} , respectively, obey the Boltzmann distribution, we have

$$\frac{\bar{P}_{\text{red}}}{\bar{P}_{\text{ox}}} = e^{ne(E_0 - E)/k_B T} \quad (9)$$

We have just retrieved the Nernst equation (Eq. 3), in terms of \bar{P}_{ox} and \bar{P}_{red} , as can be seen when we rearrange this equation:

$$E = E_0 - \frac{k_B T}{ze} \ln \frac{\bar{P}_{\text{red}}}{\bar{P}_{\text{ox}}} \quad (10)$$

This is clear when it is denoted that $R = k_B \cdot N_A$ and $e = F/N_A$. The only difference is that the concentrations of reduced and oxidized molecules are now replaced by the probabilities of being in either of the two states.

The time-averaged probabilities of being in these states must obey the condition $\bar{P}_{\text{red}} + \bar{P}_{\text{ox}} = 1$. Solving for \bar{P}_{red} and \bar{P}_{ox} gives

$$\bar{P}_{\text{red}} = \frac{1}{1 + e^{-\Delta E/k_B T}} \quad (11a)$$

$$\bar{P}_{\text{ox}} = \frac{1}{1 + e^{\Delta E/k_B T}} \quad (11b)$$

If we define the forward and backward rates in Eq. 6 as k_{red} and k_{ox} , respectively, we can also write

$$\frac{k_{\text{ox}}}{k_{\text{red}}} = e^{\Delta E/k_B T} \quad (12)$$

If a single molecule, which switches between the two states, is followed for a certain amount of time, we can determine the probability distribution of the dwell times, i.e. the times the molecule stays in either of the two states. For the present case, these distributions are given by

$$P_{\text{ox}}(t) = k_{\text{red}} e^{-k_{\text{red}} t} \quad (13a)$$

$$P_{\text{red}}(t) = k_{\text{ox}} e^{-k_{\text{ox}} t} \quad (13b)$$

We have thus established a firm relationship between redox properties of a single molecule and its dynamic behavior over time. Details for this description

of a two-state system can be found in the textbook on Biological Physics by Philip Nelson (45).

4.4 Results

4.4.1 Purification of labeled azurin

In vitro single-molecule experiments require a high level of protein purification on account of an inhomogeneous population which can otherwise significantly complicate the experimental results (46). Azurin contains a number of exposed lysines which compete with the N-terminus for binding of the Cy5-NHS ester, which may result not only in multiple labeled species, but also in multiple labels per protein molecule (42). To obtain a monodisperse and homogenous species for the single molecule experiments, azurin was further purified after labeling. The Az-Cy5 was fractionated using high resolution anion exchange chromatography, recording both overall protein absorbance at 280 nm as well as the specific absorbance of Cy5 at 650 nm. A typical chromatogram is shown in Figure 4.2A.

In the chromatographic separation we observed multiple peaks. The presence of protein in each fraction is inferred from two spectral characteristics: the absorption at 280 nm and the typical sharp peak at 291 nm due to the only tryptophan in the sequence. From the UV-vis spectral analysis of each eluting species (Figure 4.2B), fraction I shows the same spectrum as of the oxidized azurin, and is therefore ascribed to the unlabeled protein. The band around 628 nm in this case is due to the absorption of the Cu⁺ center. Moreover, in Figure 4.2B the ratio $Abs_{628nm}/Abs_{280nm} = 0.57$ for Peak I, the same as that of the unlabeled protein. The UV-vis spectra of fraction II-IV in Figure 4.2B display features of the protein as well as the label and are ascribed to labeled protein fractions. The spectra show an intense peak around 650 nm accompanied by a shoulder at 600 nm, characteristic of the Cy5 label.

We have used fraction II in all the single molecule experiments. The use of such a homogeneous sample proved to be essential for consistent recordings of the fluorescence dynamics of single molecules of labeled azurin.

4.4.2 Fluorescence switching *in bulk*

To assess the efficacy of fluorescence detection of redox-induced switching of Az-Cy5 we performed ensemble measurements using conventional spectrometry. The sample was excited at 645 nm and the fluorescence emission was monitored at 665 nm after addition of reducing or oxidizing agents.

It is well known for all type-1 Cu centers that the absorption band at 590-630 nm is only observed in the Cu^{2+} state, *i.e.* it is absent in the Cu^+ state. Thus, it is inferred (the FluRedox principle) that resonance energy transfer from the fluorescent label to the Cu center occurs in the oxidized, but not in the reduced state of azurin. This is demonstrated in Figure 4.6 (black trace), where, upon addition of oxidant ($\text{K}_3(\text{FeCN})_6$), the fluorescence intensity decreases, while subsequent addition of reductant (DTT) results in its increase. In principle, this reduction-oxidation cycle can be repeated indefinitely as previously reported (25, 27). The slight decline in fluorescence amplitude is due to dilution of the sample upon repetitive addition of reactants. We define the switching ratio (SR) of the Az-Cy5 construct as follows:

$$SR = \frac{I_{\text{red}} - I_{\text{ox}}}{I_{\text{red}}} \times 100 \% \quad (14)$$

where I_{red} and I_{ox} are the fluorescence intensity values in the reduced (on) and oxidized (off) state, respectively. For the Cy5 labeled azurin fraction associated with peak II in Figure 4.2, we found that in solution the $SR \cong 90 \%$.

The Cu ion in azurin can be reconstituted with Zn^{2+} . This Zn-azurin moiety is not redox active, and we therefore used it as a control (27, 31). Zn-azurin when labeled with Cy5 did not show any fluorescence switching upon addition of oxidant or reductant (grey line in Figure 4.6). Moreover, the control measure-

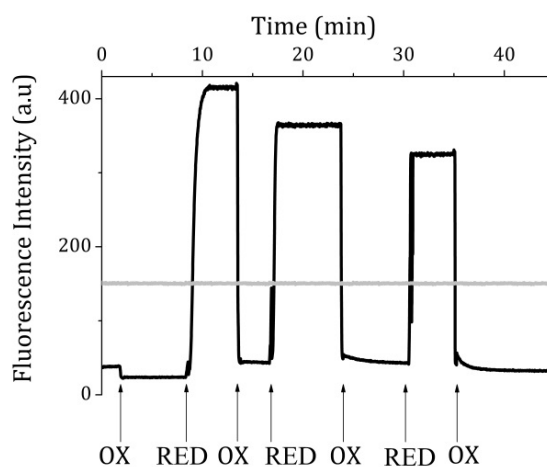


Figure 4.6. FRET-based on-off switching in bulk. 100 nM Cu-azurin labeled with Cy5 (black line) titrated with aliquots of reductant (DTT) and oxidant ($K_3(FeCN)_6$) in 100 mM phosphate buffer at pH 7.0. We observed a significant reversible change of the fluorescence intensity of Cy5 labeled azurin upon addition of oxidant or reductant. The fluorescence intensity in the oxidized state is reduced by about a factor of 10 compared to that in the reduced state. 50 nM Zn-azurin labeled with Cy5 (grey line) was used as a control and did not show any fluorescence switch.

ments also demonstrate that the Cy5 fluorescence intensity is not affected by the addition of reductant (DTT) or oxidant ($K_3(FeCN)_6$).

4.4.3 Resolving fluorescence time traces

In order to ascertain the redox-based fluorescence switching of the individual azurin molecules immobilized on a MPTS/TES coated glass substrate, we applied the fluorescence detection method that is based on the FluRedox principle. For this we tuned the chemical redox potential of the solution around the midpoint potential of azurin by means of varying the concentration of oxidant ($K_3(FeCN)_6$) and/or reductant (DTT). The final redox potentials of the solution were adjusted to -20, 0, 20, 40, 60, 80 and 100 mV, respectively, as measured with a reference electrode (standard calomel, SCE) and a counter electrode (a Pt wire) which were inserted in the droplet that covered the functionalized glass substrate. The two electrodes were wired to a voltmeter. We obtained only stable potentials

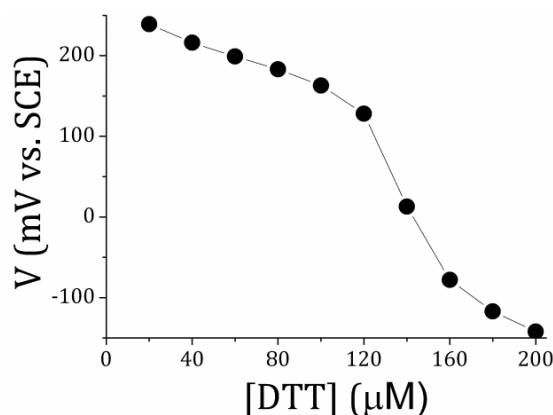


Figure 4.7. Redox titration of $\text{K}_3(\text{FeCN})_6$ at an initial concentration of about $200 \mu\text{M}$ with DTT, while measuring the potential between the SCE and Pt wire electrodes.

under oxygen-free conditions. A potentiometric titration of a solution of $\text{K}_3(\text{FeCN})_6$ with DTT under anaerobic conditions is shown in Figure 4.7. The half-wave potential for the $\text{K}_3(\text{FeCN})_6$ /DTT couple obtained from the Boltzman fit is about 31 mV vs SCE which is close to the midpoint potential of azurin (44).

As shown on Figure 4.3, Az-Cy5 was immobilized on a mixed monolayer of TES/MPTS on glass at low density such that fluorescence from single molecules can be resolved in the confocal microscope. Fluorescence time traces were obtained by successively parking the laser at each fluorescent spot in the image, and then recording the arrival times of the emitted photons. Time traces were obtained for up to 2 minutes duration. Photobleaching of Cy5 limited the time duration for which photon emission was observed to tens of seconds, and was marked by a drop of the count rate to background levels in a single step. The sample was de-aerated beforehand by bubbling with argon, and the measurements were performed under oxygen-free conditions in a sealed cell under an argon atmosphere. This not only improved the stability of the redox potential, but also enhanced the photostability of Az-Cy5, extending the time at which photobleaching occurred by at least an order of magnitude.

Typical time traces are shown in Figure 4.8 for two single Az-Cy5 molecules at

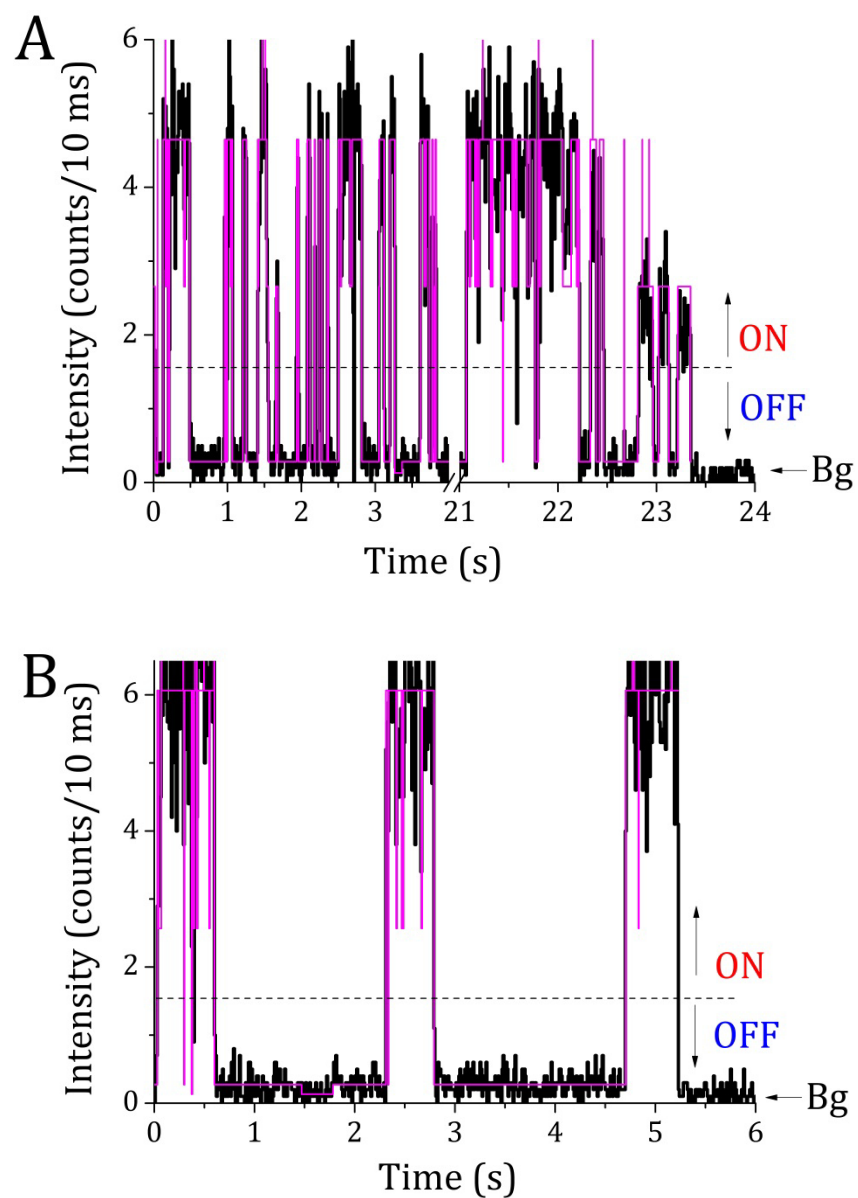


Figure 4.8. The real time fluorescence intensity traces of a single azurin molecule with a 10 ms bin size (black) and calculated intensity change-point states (purple) overlaid as a function of time. They exhibit an on-off switching behavior which depends on the redox potential in solution: A) at 20 mV vs. SCE, $\bar{P}_{\text{ox}} = 0.52$, and B) at 60 mV, $\bar{P}_{\text{ox}} = 0.76$.

different redox potentials. They show a pronounced fluorescence switching behavior, and appear to be dominated by two discrete intensity levels, corresponding to the oxidized and the reduced state, respectively, of that particular Az-Cy5 molecule. This assignment is supported by the fact that the

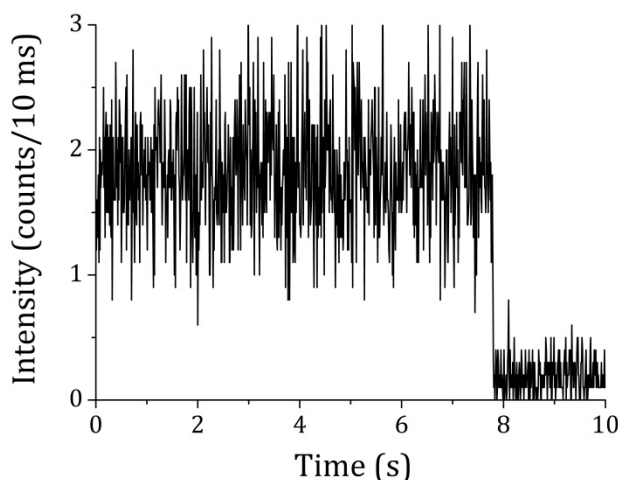


Figure 4.9. The real time fluorescence intensity trace of a Cy5 labeled single Zn-Az with a 10 ms bin size. The redox potential in solution is 20 mV vs SCE. Zn-Az does not show any fluorescence switching under the same conditions as Cu-Az (see Fig. 4.8).

control sample of Cy5-labeled Zn-Az did not show any fluorescence switching under the same condition (Fig. 4.9). The observed fluorescence time profile (Fig. 4.8, black line) of Cu-Az-Cy5 generally depends on the redox potential in solution. No redox switching was observed at potentials higher than 100 mV and lower than -20 mV: the molecule is either fully oxidized or reduced, respectively. At a potential of 60 mV (Fig. 4.8B) the Az-Cy5 molecules is mostly in the oxidized state ($\bar{P}_{\text{ox}} = 0.76$), while the reduced fraction increases at 20 mV ($\bar{P}_{\text{ox}} = 0.52$, Fig. 4.8A).

These numbers were obtained by a quantitative analysis of the time traces using the change point analysis program developed (and kindly provided) by Watkins and Yang (39). This program uses a generalized likelihood ratio test that determines the location of an intensity change point based on individual photon arrival times. Expectation maximization clustering and the Bayesian information criterion are then used for accurate determination of the true number of states accessible to the system. This procedure allows rigorous and quantitative determination of intensity change points without the artificial time resolution limitations that arise from binning and thresholding.

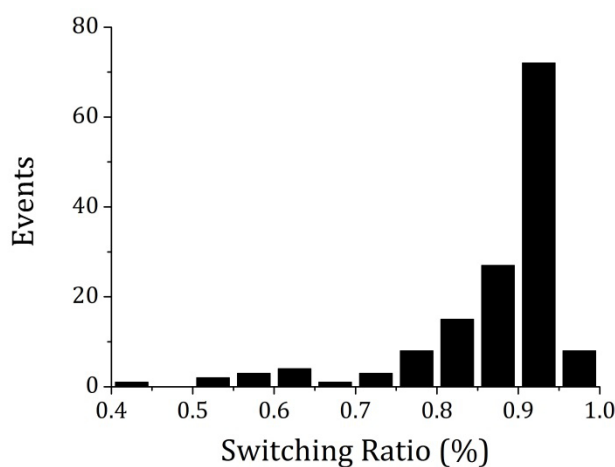


Figure 4.10. FRET-based fluorescence switching ratio (SR) of individual azurin-Cy5 molecules immobilized on a glass surface. The histogram is based on data from 150 single molecules, and the average SR of $87 \pm 5\%$ correlates well with that of labeled azurin in bulk solution (see figure 4.6).

In Figure 4.8, the time traces that resulted from the change point (CP) analysis (purple lines) were overlaid with the experimental data which are accurately reproduced. The CP analyses were actually performed in terms of 5 intensity levels, because then we were able to reliably identify the occasional blinking event by the intensity drop to the background level. Blinking is attributed to the photophysical behavior of Cy5 (47–52). The events are relatively rare, and are not counted as a redox transition. The other 4 intensity levels were assigned as "on" (Az-Cy5 reduced) or "off" (Az-Cy5 oxidized) depending on the threshold level (dashed, horizontal line in Figure 4.8) that was based on the switching ratio measured in bulk solution (see Figure 4.6). Because of the high switching ratio the fluorescence intensity of an oxidized Az-Cy5 molecule is rather close to the background level.

We calculated the fluorescence SR s of individual Az-Cy5 molecules using Equation 14. Here, the values for I_{red} and I_{ox} were obtained from the CP fits similar to the ones shown in Figure 4.8 (purple lines). The histogram in Figure 4.10 shows the distribution of fluorescence SR s of individual azurin molecules immobilized on a glass surface. The maximum SR has a value of about 91%,

while the average is $87 \pm 5\%$, in good agreement with that of redox-induced fluorescence switching in bulk. However, we observe some heterogeneity in the distribution of single azurin *SRs*, possibly associated with (average) variations in distance of Cy5 to the redox center by virtue of the length of the linker.

4.4.4 Heterogeneity in fluorescence lifetimes

To provide further insight into the FRET-based redox changes, fluorescence lifetime studies were carried out on the immobilized Az-Cy5 molecules. Since we know (from the time-tag) whether each detected photon in a particular time trace is associated with the reduced or the oxidized state, we can reconstruct separate fluorescence decay curves for both states of the same molecule. The fluorescence decay curves of individual Az-Cy5 molecules were then fitted to mono-exponential decays convoluted with the instrument response function (IRF), to determine τ_{ox} and τ_{red} , the fluorescence lifetimes in the oxidized and the reduced state, respectively.

The results are shown in Figure 4.11 for the reduced and oxidized form of Az-Cy5. In Figure 4.11A, we show an example of the fluorescence decays and their exponential fit of a single Az-Cy5. In this example, the lifetimes are $\tau_{\text{red}} = 1.8$ ns (red curve) and $\tau_{\text{ox}} = 0.8$ ns (blue curve). Here, the oxidized Az-Cy5 lifetime is reduced by the effect of FRET.

To investigate the heterogeneity in fluorescence lifetime of Az-Cy5 in its reduced/oxidized form we have analyzed more than 150 time traces. The distribution of the lifetimes of oxidized and reduced single azurin molecules are shown in Figure 4.11B which shows a significant heterogeneity for both the oxidized and the reduced forms of azurin. The experiments were repeated with the redox-inactive variant, Zn-azurin, in order to verify that the observed lifetimes were not affected by the redox components in solution. In contrast to Az-Cy5, the labeled Zn-azurin did not show any fluorescence switching, and the fluorescence lifetimes were similar to the lifetime of reduced Az-Cy5.

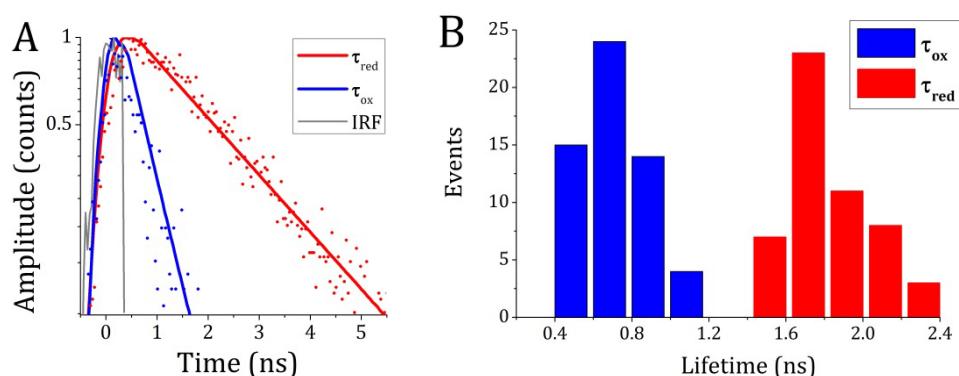


Figure 4.11. (A) Fluorescence lifetimes (dots) and fitted mono-exponential decays (lines) of surface-immobilized single azurin molecule in the oxidized (blue) and the reduced states (red): $\tau_{\text{red}} = 1.8$ and $\tau_{\text{ox}} = 0.8$ ns. (B) Fluorescence lifetime distribution of surface-immobilized single azurin molecules in the oxidized (blue) and the reduced state (red). Average lifetimes are $\bar{\tau}_{\text{ox}} = 0.7 \pm 0.15$ ns and are $\bar{\tau}_{\text{red}} = 1.8 \pm 0.2$ ns.

4.4.5 Redox parameters of a single Az-Cy5 molecule

The redox potential of the solution, E , was tuned by adding oxidant ($\text{K}_3(\text{FeCN})_6$) and reductant (DTT) to the solution. The initial concentration of $\text{K}_3(\text{FeCN})_6$ was $200 \mu\text{M}$ in all experiments, and DTT was added in small aliquots to adjust the potential. The redox potential (E) of the buffer solution covering the Az-Cy5 functionalized glass surface was thus adjusted to -20 , 0 , 20 , 40 , 60 , 80 , and 100 mV, respectively. At each potential we recorded a series of fluorescence time traces from individual Az-Cy5 molecules, and for each time trace we calculated \bar{P}_{ox} and \bar{P}_{red} (Eq. 2). From these results we calculated the midpoint potential of each single Az-Cy5 molecule using Equation 10.

The result of this analysis is summarized in Figure 4.12, which shows the distributions of the calculated midpoint potentials (E_0) at a number of solution potentials. The midpoint potentials range from -100 to 150 mV which is consistent with electrochemical data (53). All the measured midpoint potentials are lumped together in the histogram shown in Figure 4.13.

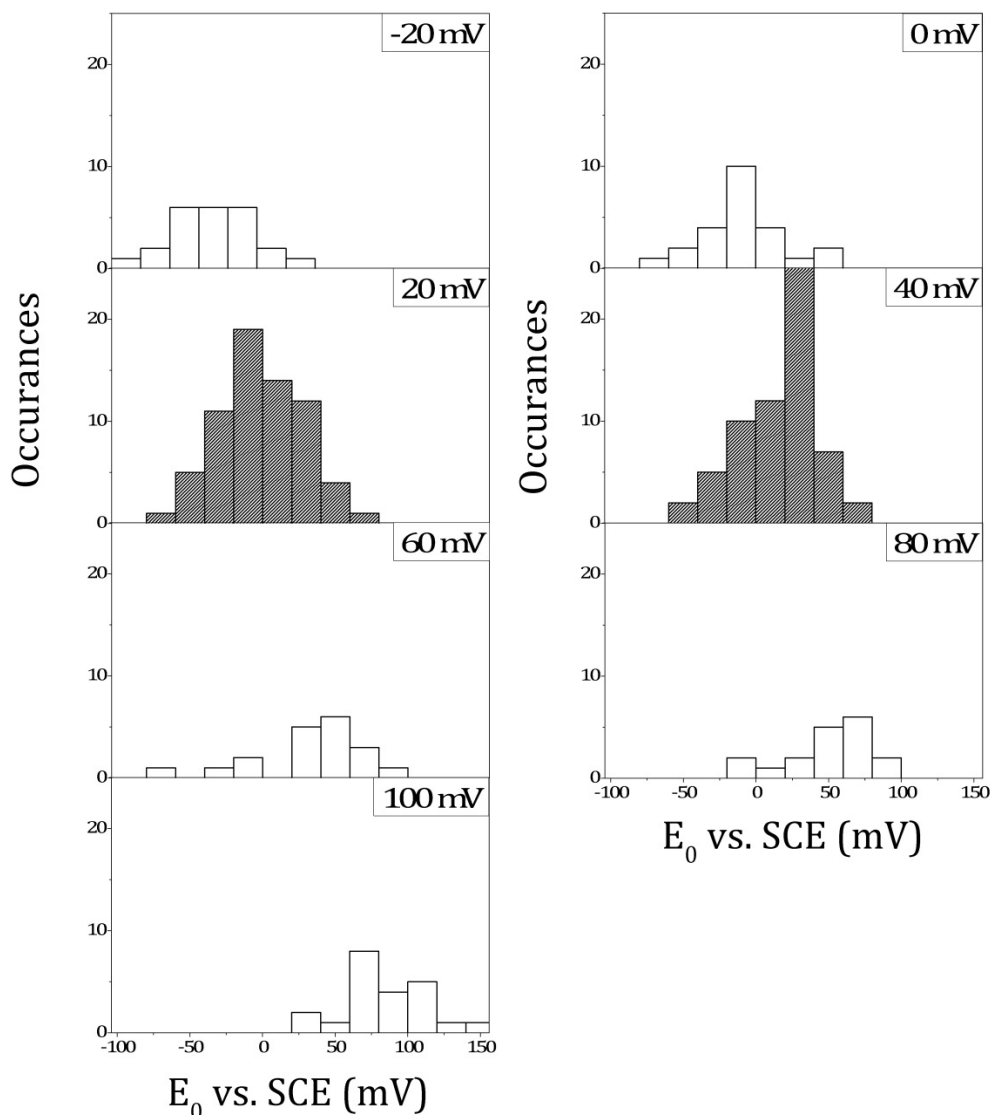


Figure 4.12. The histogram of midpoint potential (E_0) of single azurin molecules at solution potentials (E) of -20 , 0 , 20 , 40 , 60 , 80 and 100 mV. The initial concentration of $K_3[Fe(CN)_6]$ was $200 \mu M$ and DTT was added to adjust the redox potential in solution which was measured with a voltmeter using a saturated calomel electrode as a reference and 0.5 mm platinum wire as a counter electrode. All the measurements were performed under anaerobic conditions in a sealed sample-holder under continuous argon flow. E_0 was calculated using the Nernst equation (see Equation 10 in the text).

We observe that the measured distribution of midpoint potentials shifts with the actual redox potential of the solution. This can be explained by the fact that the data contain a bias towards selection of Az-Cy5 molecules that are relatively

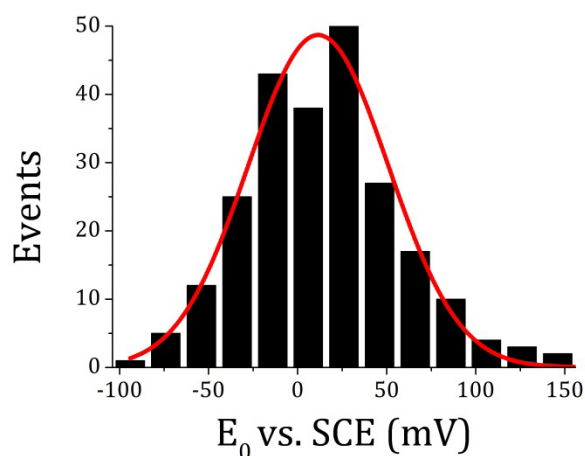


Figure 4.13. The histogram of midpoint potential (E_0) of about 200 single azurin molecules. The average midpoint potential was calculated from a Gaussian fit as 12 ± 3 mV with a fwhm = 92 mV vs SCE. E_0 of each single molecule was calculated using the Nernst equation (see Equation 10 in the text).

bright. Because of the high switching ratio, molecules that are mostly in the oxidized state are under-represented because of low visibility. Furthermore, we have only analysed molecules that show fluorescence switching activity, which implies a bias by selecting molecules with a range of midpoint potential around the redox potential in solution. It is estimated that the fraction of molecules that are actively switching is about 50% at 20 and 40 mV, and is decreasing at higher and lower redox potentials, dropping to about 10% at -20 and 100 mV.

We note, however, that the overall distribution in Figure 4.13 is dominated by the measurements at 20 and 40 mV, both close to the average midpoint potential. For these measurements the bias is relatively small, and we believe that the distribution in Figure 4.13 is representative of the heterogeneity of the midpoint potentials of individual Az-Cy5 molecules. The histogram in Figure 4.13 for about 200 individual molecules was fitted with a Gaussian. The average midpoint potential is 12 ± 3 mV vs. SCE, and the distribution is characterized by a fwhm of 92 mV.

4.4.6 Electron transfer kinetics of a single azurin

The final aspect of fluorescence-detected redox switching of single Az-Cy5 molecules is the time scale, and thus the rate at which the switching occurs. The relevant parameters are the reaction rate constants of the electron transfer, k_{ox} and k_{red} , for the oxidation and reduction reaction, respectively. They can be deduced for each molecule from the time traces through the distribution of dwell times, *i.e.* the times the molecule stays in a certain state before jumping to the

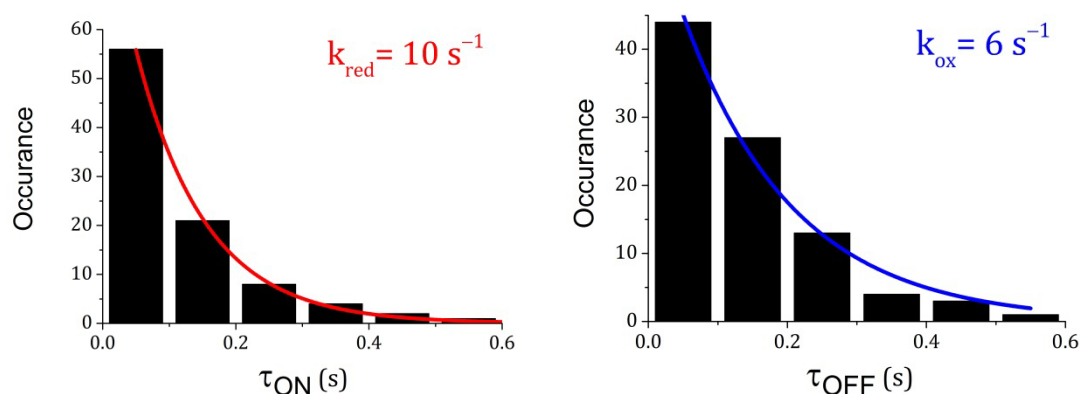


Figure 4.14. Histograms of on and off times for a single azurin-Cy5 at solution potential of 20 mV. The rate constant is given by the inverse of the characteristic time constants of the mono-exponential fits of the distributions. This result is obtained from the time trace in Figure 4.8A.

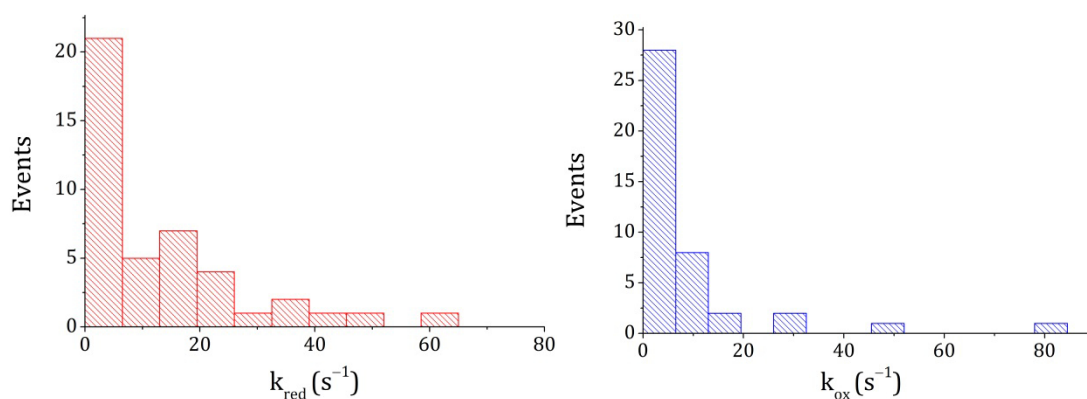


Figure 4.15. The distribution of the reaction rates of individual Az-Cy5 molecules.

other state. The reaction rate constants can be derived from the dwell time distributions using equation 13a and 13b. The dwell times of both states (oxidized and reduced) were measured for all the switching time traces.

The dwell time distributions obtained in this way were fitted to a mono-exponential decay for both states (oxidized and reduced), from which the characteristic time constant and its reciprocal, the reaction rate, were deduced. In Figure 4.14, we show the distribution of dwell times for both, the reduced and oxidized state of a single azurin molecule (see Figure 4.8A). From the characteristic time constants of the mono-exponential fits we find for this case that k_{ox} and k_{red} are equal to 10 s^{-1} and 6 s^{-1} , respectively.

We have determined the reaction rate constants, k_{ox} and k_{red} , for a limited number of molecules, because not all time traces were long enough to obtain a meaningful fit of the dwell times. Figure 4.15 shows that the distribution of reaction rates is rather broad.

4.5 Discussion

Photophysics of Cy5: In the present work, azurin was labeled with Cy5-NHS forming the donor in a FRET pair with the Cu redox center which acts as the acceptor. In FRET experiments Cy5 is notorious because of its complex excited state dynamics (for reviews, see (47, 54)). This involves the formation of triplet states and of long-lived conformational isomers, both of which are susceptible to photochemical transformations leading to permanent photobleaching. For the latter, not only the presence of oxygen, but also reactions with thiols play a key role (49). At the single-molecule level, the transient population of non-fluorescent states in Cy5 is the main cause of blinking, which may interfere with other signals that are being monitored via Cy5 excitation. In order to reduce the blinking and photobleaching rates, the effects of oxidizing and reducing agents (e.g., *N,N*-methylviologen, ascorbic acid) and triplet state quenchers (TSQs; e.g.,

Trolox, β -mercaptoethylamine) on the excited state properties of Cy5 in solution have been studied extensively (48, 55–58). It was shown that thiol-induced blinking of Cy5 can be overcome using Trolox in combination with a reducing/oxidizing system. Notably, the conjugation of Cy5 to biomolecules can also strongly reduce the efficiency of photoisomerization, resulting in a large increase of fluorescence quantum yield and lifetime (59–63).

In FRET experiments, photo-induced blinking of Cy5 seems to be most problematic when it is used as the acceptor, in which case the shorter-wavelength excitation of the donor may also affect the photophysics of Cy5 (64). Fluctuations in Cy5 fluorescence due to the population of transient, non-fluorescent states can be easily mistaken as fluctuations in FRET efficiency (65).

In the measurements on Cy5-labeled azurin described in this chapter, it proved, indeed, essential to remove oxygen from the solution. Adding oxygen scavengers to the solution was not an option because they may interact with the label or the chemicals in solution. Moreover, TSQs have key limitations, including poor aqueous solubility, problems with membrane permeability and biological toxicity (66,67). Rather, oxygen was removed by sparging with argon. It dramatically increased the number of emitted photons from the Cy5-label before bleaching. Under those conditions, and with 100-200 μ M of reductant and oxidant in solution, we did not see any blinking in the control experiments with Cy5-labeled Zn-Az on the millisecond time scale. We can actually not exclude that blinking still occurs on the sub-millisecond time scale. It is quite possible that the redox components in solution contribute to triplet quenching and the suppression of subsequent photochemical reactions of Cy5 labeled azurin. The conjugation of Cy5 with azurin is also likely to reduce the propensity for photoisomerization. These possibilities were not explored in further detail.

Fluorescence lifetimes: The fluorescence lifetime of Cy5 is somewhat variable, depending on the solvent and the viscosity, for example. The fluorescence lifetime increases from 1.0 ns in water (68) to 2.0 ns when embedded in

polyvinylalcohol (PVA) (52). It is generally believed that this variability of the fluorescence lifetime is associated with the freedom of rotation of the polymethine chain (with heterocyclic moieties at each end) upon excitation of Cy5, which is associated with cis-trans photoisomerisation. This is corroborated by the relatively long fluorescence lifetime of Cy5 in a PVA matrix (52). For the average fluorescence lifetime of reduced Az-Cy5 we obtain a value of 1.8 ± 0.2 ns, and similar values of Cy5-labeled Zn-Az. This is substantially longer than for Cy5 in water, and suggests that conjugation to azurin significantly affects the dynamics of the photoisomerisation process. Presumably the rate of photoisomerization is lower than that of the free dye in aqueous solution. The distribution of the fluorescence lifetimes in Figure 4.11B could be due, at least partially, to different ways at which the Cy5 label can arrange itself at the protein surface.

When Az-Cy5 is oxidized, the average fluorescence lifetime is reduced to 0.7 ± 0.15 ns because of fluorescence quenching by FRET from the fluorophore to the Cu-center. From the fluorescence lifetimes we calculate a FRET efficiency of $E = 1 - (\tau_{\text{ox}}/\tau_{\text{red}}) = 0.60 \pm 0.09$. This number clearly deviates from the value of 0.87 that we calculate from the average switching ratios (Figure 4.10). It is an observation that we cannot explain at this moment, and that needs to be investigated in more detail.

Midpoint potentials: The average value of the midpoint potentials as measured by the single-molecule fluorescence time traces are consistent with other measurements, including those presented in Chapters 2 and 3 of this thesis. New in these experiments is the fact that we can obtain the distribution of midpoint potentials of individual Az-Cy5 molecules in solution, which is characterized by a fwhm of 92 mV. This value is significantly larger than the value of 14-15 mV found by FCV of Az-Cy5 adsorbed on an octanethiol SAM-coated gold electrode, both, at the single-molecule level (Figure 3.13, Chapter 3) and with high-density coverage (Figure 2.4a). The latter samples involve adsorption of Az-Cy5 on the thiolalkane SAM through hydrophobic interaction.

It is well established that the electrostatic environment of the entire protein and solvent system is a determining factor in fine-tuning the electronic properties of the metal-binding site of copper-containing proteins (69). In particular, hybrid quantum mechanics/molecular mechanics model calculations have shown that the electronic properties of the Cu-center in azurin are sensitive to long-range electrostatic interactions (70). These calculations also show a significant solvent rearrangement in a region close to the copper ion, specifically, around the copper-bound His117 residue upon reduction. It is claimed that the water rearrangement accounts for ~80% of the calculated value of the reorganization energy in this process. A similar conclusion was reached on the basis of experiments on electron tunneling in azurin crystals (71). Presumably the rearrangement is driven by modification of the electrostatic potential at the protein surface around His117, reflecting the change in the oxidation state of Cu. It may also affect the conformation of solvent-exposed side chains.

It thus seems reasonable to conclude that the local variations in the outer sphere around His117 can contribute to variations in the midpoint potential of individual azurin molecules. This residue, which has a key role in the electron transfer reaction of azurin, is normally in direct contact with the solvent. The experiments described in this chapter were designed to minimize the effect of the (modified) glass surface by using a rather long linker to covalently immobilize the protein. It may be assumed that under those conditions the Az-Cy5 behaves as a free molecule in solution with the His117 residue fully exposed to the solvent environment. This is different for the immobilization method that was used in Chapters 2 and 3. Here, the hydrophobic patch of the protein around His117 is largely shielded from the solution. In fact, at the hydrophobic interface between the protein and the SAM, most water molecules will be expelled. The result is a more homogeneous and a more static environment of the His117 residue than for azurin in solution. This is reflected in the relatively small heterogeneity of the midpoint potential, compared to that of Az-Cy5 in solution.

Dwell times and reaction rates: We observe a large heterogeneity in the forward and backward electron transfer reactions of Az-Cy5 with oxidants and reductants in solution (Figure 4.15). We attribute this heterogeneity to variations in the reorganisation energies from molecule to molecule. It would be interesting to extend these experiments to include different oxidants and reductants at a wider range of concentrations.

4.6 Conclusions

In summary, we have successfully immobilized Cy5-labeled azurin at the SM level by using a thiol-based, site-specific covalent linker. We have demonstrated that the fluorescence intensity of a single azurin molecule as a function of time shows on-off switching behavior which depends on the redox conditions in solution. Purified single Az-Cy5 molecules show a 87% switching ratio that is consistent with results of ensemble measurements.

To the best of our knowledge, we were able to determine for the first time the reaction kinetics and thermodynamic midpoint potential of individual azurin molecules. We have made a quantitative assessment of the heterogeneity of the midpoint potential, electron transfer rates and the lifetimes at the single-protein level. The local environment of the His117 residue was shown to be a determining factor for the distribution of midpoint potentials of single Az-Cy5 molecules. The FluRedox method could be easily applied to many other redox molecules, opening new doors for the application of fluorescence-based biosensor and molecular electronics.

References

1. Moore GF and Brudvig GW. 2011. Energy Conversion in Photosynthesis: A Paradigm for Solar Fuel Production. *Annual Review of Condensed Matter Physics* 2(1):303–327. Annual Reviews.
2. Ramirez BE, Malmström BG, Winkler JR, and Gray HB. 1995. The currents of life: the terminal electron-transfer complex of respiration. *Proceedings of the National Academy of Sciences of the United States of America* 92(26):11949–51.
3. Jonkheijm P, Weinrich D, Schröder H, Niemeyer CM, and Waldmann H. 2008. Chemical strategies for generating protein biochips. *Angewandte Chemie (International ed. in English)* 47(50):9618–47.
4. Willner I. 2002. Tech.Sight. Bioelectronics. Biomaterials for sensors, fuel cells, and circuitry. *Science (New York, N.Y.)* 298(5602):2407–8.
5. Yang H, Luo G, and Karnchanaphanurach P. 2003. Protein conformational dynamics probed by single-molecule electron transfer. *Science* 302(October):262–266.
6. Smiley RD and Hammes GG. 2006. Single molecule studies of enzyme mechanisms. *Chemical reviews* 106(8):3080–94.
7. Blank K, De Cremer G, and Hofkens J. 2009. Fluorescence-based analysis of enzymes at the single-molecule level. *Biotechnology journal* 4(4):465–79.
8. Gopich I V and Szabo A. 2006. Theory of the statistics of kinetic transitions with application to single-molecule enzyme catalysis. *The Journal of chemical physics* 124(15):154712.
9. English BP, Min W, Van Oijen AM, Lee KT, Luo G, Sun H, Cherayil BJ, Kou SC, and Xie XS. 2006. Ever-fluctuating single enzyme molecules: Michaelis-Menten equation revisited. *Nature chemical biology* 2(2):87–94.
10. Flomenbom O, Klafter J, and Szabo A. 2005. What can one learn from two-state single-molecule trajectories? *Biophysical journal* 88(6):3780–3.
11. Solomon EI. 1992. Electronic structures of active sites in copper proteins: Contributions to reactivity. *Journal of Inorganic Biochemistry* 47(3-4):29.
12. Jeuken LJC, P Van Vliet, Verbeet MPH, Camba R, McEvoy JP, Armstrong FA and CG. 2000. Role of the surface-exposed and copper-coordinating histidine in blue copper proteins: The electron-transfer and redox-coupled ligand binding properties of His117Gly azurin. *Journal of the American Chemical Society* (11):12186–12194.
13. Adman E and Stenkamp R. 1978. A crystallographic model for azurin a 3 Å resolution. *Journal of molecular biology* 123:35–47.
14. Nar H, Messerschmidt A, Huber R, Van de Kamp M, and Canters GW. 1991. Crystal structure analysis of oxidized *Pseudomonas aeruginosa* azurin at pH 5.5 and pH 9.0: A pH-induced conformational transition involves a peptide bond. *Journal of Molecular Biology* 221(3):765–72.
15. Baker EN. 1988. Structure of azurin from *Alcaligenes denitrificans* refinement at 1.8 Å resolution and comparison of the two crystallographically independent molecules. *Journal of molecular biology* 203(4):1071–95.
16. Vijgenboom E, Busch JE, and Canters GW. 1997. In vivo studies disprove an obligatory role of azurin in denitrification in *Pseudomonas aeruginosa* and show that *azu* expression is under control of *rpoS* and ANR. *Microbiology (Reading, England)* 143 (Pt 9(1997):2853–63.
17. Van de Kamp M, Silvestrini MC, Brunori M, Van Beeumen J, Hali FC, and Canters GW. 1990. Involvement of the hydrophobic patch of azurin in the electron-transfer reactions with

- cytochrome C551 and nitrite reductase. *European journal of biochemistry / FEBS* 194(1):109–18.
18. Simon J and Klotz MG. 2012. Diversity and evolution of bioenergetic systems involved in microbial nitrogen compound transformations. *Biochimica et biophysica acta*: Elsevier B.V.
 19. Farver O, Brunori M, Cutruzzola F, Rinaldo S, Wherland S, and Pecht I. 2009. Intramolecular electron transfer in *Pseudomonas aeruginosa* cd(1) nitrite reductase: thermodynamics and kinetics. *Biophysical journal* 96(7):2849–56. Biophysical Society.
 20. Tepper AWJW. 2010. Electrical contacting of an assembly of pseudoazurin and nitrite reductase using DNA-directed immobilization. *Journal of the American Chemical Society* 132(18):6550–7.
 21. Bizzarri AR. 2011. Steered molecular dynamics simulations of the electron transfer complex between azurin and cytochrome c551. *The journal of physical chemistry. B* 115(5):1211–9.
 22. Yang D, Miao X, Ye Z, and Feng J. 2005. Bacterial redox protein azurin induce apoptosis in human osteosarcoma U2OS cells. *Pharmacological Research* 52:413–421.
 23. Yamada T, Hiraoka Y, Ikehata M, Kimbara K, Avner BS, Das Gupta TK, and Chakrabarty AM. 2004. Apoptosis or growth arrest: Modulation of tumor suppressor p53's specificity by bacterial redox protein azurin. *Proceedings of the National Academy of Sciences of the United States of America* 101(14):4770–5.
 24. Shleev S, Wetterö J, Magnusson K-E, and Ruzgas T. 2006. Electrochemical characterization and application of azurin-modified gold electrodes for detection of superoxide. *Biosensors & bioelectronics* 22(2):213–9.
 25. Schmauder R, Alagaratnam S, Chan C, Schmidt T, Canters GW, and Aartsma TJ. 2005. Sensitive detection of the redox state of copper proteins using fluorescence. *Journal of biological inorganic chemistry: JBIC: a publication of the Society of Biological Inorganic Chemistry* 10(6):683–7.
 26. Solomon E and Hare J. 1980. Spectroscopic studies of stellacyanin, plastocyanin, and azurin. Electronic structure of the blue copper sites. *Journal of the American Chemical Society* 102(1):168–178.
 27. Kuznetsova S, Zauner G, Schmauder R, Mayboroda O a, Deelder AM, Aartsma TJ, and Canters GW. 2006. A Förster-resonance-energy transfer-based method for fluorescence detection of the protein redox state. *Analytical biochemistry* 350(1):52–60.
 28. Zauner G, Lonardi E, Bubacco L, Aartsma TJ, Canters GW, and Tepper AWJW. 2007. Tryptophan-to-dye fluorescence energy transfer applied to oxygen sensing by using type-3 copper proteins. *Chemistry-A European Journal* 13(25):7085–90.
 29. Strianese M, Zauner G, Tepper AWJW, Bubacco L, Breukink E, Aartsma TJ, Canters GW, and Tabares LC. 2009. A protein-based oxygen biosensor for high-throughput monitoring of cell growth and cell viability. *Analytical biochemistry* 385(2):242–8. Elsevier Inc.
 30. Gustiananda M, Andreoni A, Tabares LC, Tepper AWJW, Fortunato L, Aartsma TJ, and Canters GW. 2012. Sensitive detection of histamine using fluorescently labeled oxido-reductases. *Biosensors & Bioelectronics* 31(1):419–25.
 31. Schmauder R, Librizzi F, Canters GW, Schmidt T, and Aartsma TJ. 2005. The oxidation state of a protein observed molecule-by-molecule. *Chemphyschem: a European journal of chemical physics and physical chemistry* 6(7):1381–6.
 32. Kuznetsova S, Zauner G, Aartsma TJ, Engelkamp H, Hatzakis N, Rowan AE, Nolte RJM, Christianen PCM, and Canters GW. 2008. The enzyme mechanism of nitrite reductase studied at single-molecule level. *Proceedings of the National Academy of Sciences of the United States of America* 105(9):3250–5.

33. Tabares LC, Kostrz D, Elmalk A, Andreoni A, Dennison C, Aartsma TJ, and Canters GW. 2011. Fluorescence lifetime analysis of nitrite reductase from *Alcaligenes xylosoxidans* at the single-molecule level reveals the enzyme mechanism. *Chemistry A European Journal* 17(43):12015–9.
34. Elmalk AT, Salverda JM, Tabares LC, Canters GW, and Aartsma TJ. 2012. Probing redox proteins on a gold surface by single molecule fluorescence spectroscopy. *The Journal of chemical physics* 136(23):235101.
35. Goldsmith RH, Tabares LC, Kostrz D, Dennison C, Aartsma TJ, Canters GW, and Moerner WE. 2011. Redox cycling and kinetic analysis of single molecules of solution-phase nitrite reductase. *Proceedings of the National Academy of Sciences of the United States of America* 108(42):17269–74.
36. Krzemiński Ł, Ndamba L, Canters GW, Aartsma TJ, Evans SD, and Jeuken LJC. 2011. Spectroelectrochemical investigation of intramolecular and interfacial electron-transfer rates reveals differences between nitrite reductase at rest and during turnover. *Journal of the American Chemical Society* 133(38):15085–93.
37. Davis JJ, Burgess H, Zauner G, Kuznetsova S, Salverda J, Aartsma T, and Canters GW. 2006. Monitoring interfacial bioelectrochemistry using a FRET switch. *The journal of physical chemistry. B* 110(41):20649–54.
38. Salverda JM, Patil A V., Mizson G, Kuznetsova S, Zauner G, Akkilic N, Canters GW, Davis JJ, Heering HA, and Aartsma TJ. 2010. Fluorescent cyclic voltammetry of immobilized azurin: direct observation of thermodynamic and kinetic heterogeneity. *Angewandte Chemie (International ed. in English)* 49(33):5912–5915.
39. Watkins LP and Yang H. 2005. Detection of intensity change points in time-resolved single-molecule measurements. *The journal of physical chemistry. B* 109(1):617–28.
40. Van de Kamp M, Hali FC, Rosato N, Agro a F, and Canters GW. 1990. Purification and characterization of a non-reconstitutable azurin, obtained by heterologous expression of the *Pseudomonas aeruginosa* *azu* gene in *Escherichia coli*. *Biochimica et biophysica acta* 1019(3):283–92.
41. Canters GW. 1987. The azurin gene from *Pseudomonas aeruginosa* codes for a pre-protein with a signal peptide. *FEBS Letters* 212(1):168–172.
42. Nicolardi S, Andreoni A, Tabares LC, Van der Burgt YEM, Canters GW, Deelder AM, and Hensbergen PJ. 2012. Top-down FTICR MS for the identification of fluorescent labeling efficiency and specificity of the Cu-protein azurin. *Analytical chemistry* 84(5):2512–20.
43. Cleland W. 1964. Dithiothreitol, a New Protective Reagent for SH Groups*. *Biochemistry* 0(1960):480–482.
44. Marshall NM, Garner DK, Wilson TD, Gao Y-G, Robinson H, Nilges MJ, and Lu Y. 2009. Rationally tuning the reduction potential of a single cupredoxin beyond the natural range. *Nature* 462(7269):113–6.
45. Nelson P. 2007. *Biological Physics (Updated Edition)*. 600. W. H. Freeman.
46. Brouhard GJ. 2010. Quality control in single-molecule studies of kinesins and microtubule-associated proteins. *Methods in cell biology* 97:497–506.
47. Ha T and Tinnefeld P. 2012. Photophysics of fluorescent probes for single-molecule biophysics and super-resolution imaging. *Annual review of physical chemistry* 63:595–617.
48. Heilemann M, Margeat E, Kasper R, Sauer M, and Tinnefeld P. 2005. Carbocyanine dyes as efficient reversible single-molecule optical switch. *Journal of the American Chemical Society* 127(11):3801–6.

49. Dempsey GT, Bates M, Kowtoniuk WE, Liu DR, Tsien RY, and Zhuang X. 2009. Photoswitching mechanism of cyanine dyes. *Journal of the American Chemical Society* 131(51):18192–3.
50. Huang Z, Ji D, Wang S, Xia A, Koberling F, Patting M, and Erdmann R. 2006. Spectral identification of specific photophysics of cy5 by means of ensemble and single molecule measurements. *The journal of physical chemistry. A* 110(1):45–50.
51. Huang Z, Ji D, and Xia A. 2005. Fluorescence intensity and lifetime fluctuations of single Cy5 molecules immobilized on the glass surface. *Colloids and Surfaces A: Physicochemical and Engineering Aspects* 257-258:203–209.
52. Singh MK. 2009. Time-resolved single molecule fluorescence spectroscopy of Cy5-dCTP: influence of the immobilization strategy. *Physical chemistry chemical physics: PCCP* 11(33):7225–30.
53. Jeuken LJC and Armstrong FA. 2001. Electrochemical Origin of Hysteresis in the Electron-Transfer Reactions of Adsorbed Proteins: Contrasting Behavior of the “ Blue ” Copper Protein , Azurin , Adsorbed on Pyrolytic Graphite and Modified Gold Electrodes. *Journal of Physical Chemistry B* 105:5271–5282.
54. Levitus M and Ranjit S. Cyanine dyes in biophysical research: the photophysics of polymethine fluorescent dyes in biomolecular environments. *Quarterly Reviews of Biophysics* 44(01):123–151.
55. Cordes T, Vogelsang J, Anaya M, Spagnuolo C, Gietl A, Summerer W, Herrmann A, Müllen K, and Tinnefeld P. 2010. Single-molecule redox blinking of perylene diimide derivatives in water. *Journal of the American Chemical Society* 132(7):2404–9.
56. Vogelsang J, Kasper R, Steinhauer C, Person B, Heilemann M, Sauer M, and Tinnefeld P. 2008. A reducing and oxidizing system minimizes photobleaching and blinking of fluorescent dyes. *Angewandte Chemie (International ed. in English)* 47(29):5465–9.
57. Rasnik I, McKinney S, and Ha T. 2006. Nonblinking and long-lasting single-molecule fluorescence imaging. *Nature Methods* 3(11):891–893.
58. Cordes T, Vogelsang J, and Tinnefeld P. 2009. On the mechanism of Trolox as antiblinking and antibleaching reagent. *Journal of the American Chemical Society* 131(14):5018–9.
59. Blanchard SC, Kim HD, Gonzalez RL, Puglisi JD, and Chu S. 2004. tRNA dynamics on the ribosome during translation. *Proceedings of the National Academy of Sciences of the United States of America* 101(35):12893–8.
60. Widengren J and Schwille P. 2000. Characterization of Photoinduced Isomerization and Back-Isomerization of the Cyanine Dye Cy5 by Fluorescence Correlation Spectroscopy. *The Journal of Physical Chemistry A* 104(27):6416–6428.
61. Yasuda R, Masaike T, Adachi K, Noji H, Itoh H, and Kinosita K. 2003. The ATP-waiting conformation of rotating F1-ATPase revealed by single-pair fluorescence resonance energy transfer. *Proceedings of the National Academy of Sciences of the United States of America* 100(16):9314–8.
62. Tolosa L, Malak H, Raob G, and Lakowicz JR. 1997. Optical assay for glucose based on the luminescence decay time of the long wavelength dye Cy5TM. *Sensors and Actuators B: Chemical* 45(2):93–99.
63. Schobel U, Egelhaaf H-J, Brecht A, Oelkrug D, and Gauglitz G. 1999. New Donor–Acceptor Pair for Fluorescent Immunoassays by Energy Transfer. *Bioconjugate Chemistry* 10(6):1107–1114. American Chemical Society.
64. Eggeling C, Widengren J, Brand L, Schaffer J, Felekyan S, and Seidel CAM. 2006. Analysis of photobleaching in single-molecule multicolor excitation and Förster resonance energy

- transfer measurements. *The journal of physical chemistry. A* 110(9):2979–95. American Chemical Society.
65. Koopmans WJA, Brehm A, Logie C, Schmidt T, and Van Noort J. 2007. Single-pair FRET microscopy reveals mononucleosome dynamics. *Journal of fluorescence* 17(6):785–95.
 66. Altman RB, Terry DS, Zhou Z, Zheng Q, Geggier P, Kolster R a, Zhao Y, Javitch J a, Warren JD, and Blanchard SC. 2012. Cyanine fluorophore derivatives with enhanced photostability. *Nature methods* 9(1):68–71.
 67. Dave R, Terry DS, Munro JB, and Blanchard SC. 2009. Mitigating unwanted photophysical processes for improved single-molecule fluorescence imaging. *Biophysical journal* 96(6):2371–81. Biophysical society.
 68. Tinnefeld P and Buschmann, V Dirk-Peter Herten, Kyung-Tae Han SM. 2000. Confocal fluorescence lifetime imaging microscopy (FLIM) at the single molecule level. *Single Molecules* 1:215–223.
 69. Olsson MHM, Hong G, and Warshel A. 2003. Frozen density functional free energy simulations of redox proteins: computational studies of the reduction potential of plastocyanin and rusticyanin. *Journal of the American Chemical Society* 125(17):5025–39.
 70. Cascella M, Magistrato A, Tavernelli I, Carloni P, and Rothlisberger U. 2006. Role of protein frame and solvent for the redox properties of azurin from *Pseudomonas aeruginosa*. *Proceedings of the National Academy of Sciences of the United States of America* 103(52):19641–6.
 71. Crane BR, Di Bilio AJ, Winkler JR, and Gray HB. 2001. Electron Tunneling in Single Crystals of *Pseudomonas a eruginosa* Azurins. *Journal of the American Chemical Society* 123(47):11623–11631. American Chemical Society.

Summary

Copper proteins are involved in a wide range of electron transfer processes, predominantly in biological energy conversion cycles, but also in a wide range of biochemical transformations occurring, e.g., in metabolic processes.

The availability of single-molecule fluorescence detection techniques has brought about a breakthrough in the optical studies of biomolecular properties and functions by enabling the study of molecules one at a time. In this thesis, single-molecule detection is used to obtain detailed information of electron transfer reactions at the interface of a copper protein and a gold electrode. The approach is based on Förster resonance energy transfer (FRET) in a suitably labeled redox protein, where a site-specifically attached, fluorescent dye-label (the donor) and the redox center (the acceptor, with a characteristic absorption spectrum) form a FRET pair. The FRET efficiency depends on the overlap integral of emission and absorption bands of the donor and acceptor, respectively. Thus, changes in the absorbance upon reduction or oxidation of the protein can be monitored via changes in the fluorescence intensity of the covalently attached label. Fluorescence detection provides a much enhanced sensitivity compared to absorbance measurements, down to the single-molecule level.

In the present work, azurin was labeled with Cy5, the latter forming the donor in a FRET pair with the Cu redox center of the protein, acting as the acceptor. Especially in the measurements on Cy5-labeled azurin described in Chapters 3 and 4, it was essential to remove all oxygen from the solution, and to add a purification step after protein labeling.

In the work described in this thesis, it was shown that fluorescence-detected electrochemistry and chemical control of the redox state-changes of a metalloprotein provide excellent methods to explore the kinetic and thermodynamic mechanisms of redox proteins at the single-molecule level.

Especially, fluorescence detected electrochemistry may be used for further investigation of protein-electrode or protein-protein interactions. The methods can be easily applied to many other redox proteins or enzymes, and have potential for applications in fluorescence-based biosensors and molecular electronics.

In **Chapter 1**, an overview is given of the concepts and methods that are basic to this thesis, e.g., electrochemistry, single-molecule fluorescence detection and the FluRedox principle. Also, the theoretical background of thermodynamics and electron transfer of biological redox reactions is briefly described.

In **Chapter 2**, a novel method, fluorescence detected cyclic voltammetry (FCV), is applied to investigate a monolayer of azurin labeled with Cy5, immobilized on a semi-transparent gold electrode by adsorption on a hexanethiol self-assembled monolayer which was deposited on the gold film. Conventional cyclic voltammetry (CV) was applied at scan rates ranging from 10 mV/s to 10 V/s. From the CV curves of electrode current versus applied potential, the midpoint potential of azurin was determined to be 45 ± 5 mV (at pH 7) relative to a saturated calomel electrode, in agreement with literature values.

For fluorescence-detected electrochemistry azurin, labeled with Cy5, was immobilized at a relatively low density on a semi-transparent gold electrode by adsorption on a 1-octanethiol self-assembled monolayer which was deposited on the gold film. The gold film was configured as the working electrode in an electrochemical cell. The fluorescence intensity of Cy-5 labeled azurin was shown to be determined by the redox state of the Cu-center which was controlled by the applied electrode potential. Fluorescence images of the functionalized electrode were acquired in rapid succession and with high time resolution, synchronous with the variation in time of the applied potential profiles. Intensity time traces of the Cy5-azurin fluorescence as a function of the electrode potential were constructed from the microscope images for further analysis. These epifluorescent voltammograms of Cy5-azurin were measured at

scan rates ranging from 10 mV/s to 1 V/s, and redox parameters were determined by fitting the data based on the Butler-Volmer theory. From the scan-rate dependence of, both, fluorescence-detected and conventional cyclic voltammetry, values were obtained for the midpoint potential and electron-transfer rate constants. These parameters are associated with only a relatively small number of molecules, as low as a few hundred, by limiting the intensity measurements to a few pixels in the image. A large heterogeneity was observed in the fluorescence intensity response across the surface. The thermodynamic midpoint potential was found to vary by tens of millivolts across the electrode surface, and the standard electron-transfer rate constant varied by more than a factor of 100. Our study shows that fluorescent cyclic voltammetry provides an excellent tool to probe surface homogeneity, molecular conductance and redox site coupling to electrodes.

In **Chapter 3**, real-time measurements of single electron transfer events under electrochemical control are presented and discussed. In this work, a confocal microscope with electrochemical potential control was used to monitor the redox state changes of fluorescently labeled, surface-confined azurin with single-molecule resolution. In these experiments we used the FRET-based redox state detection of the Cy5-azurin construct as a model system. Like in the previous chapter, an octanethiol surface-assembled monolayer was used to adsorb and immobilize the Cy5-azurin construct on the thin, semi-transparent gold electrode. The system was shown to be electrochemically active by cyclic voltammetry measurements. The individual Cy5-azurin molecules immobilized on the thin Au electrodes were monitored by confocal fluorescence microscopy. They showed an on (reduced)-off (oxidized) switching behavior of the fluorescence intensity with a varying, externally applied potential. By analysis of the fluorescence intensity as a function of the applied potential it was found that the distribution of optically-determined midpoint potentials of individual azurin molecules has an average value of 45.7 ± 0.5 mV and a full width at half maximum of 15 mV (relative to a saturated calomel electrode). These results constitute the

first direct observation of fluorescence detected electrochemistry and thermodynamic dispersion of individual redox proteins.

In **Chapter 4**, another powerful method was introduced to follow chemically induced redox reactions of an individual metalloprotein which was covalently immobilized on a glass surface. In this method, fluorescence emission from individual Cy5-azurin molecules was detected as a function of the redox potential in solution, using time-correlated single-photon counting. The chemical redox potential was controlled by adjusting reductant and oxidant concentrations in the buffer solution. It was measured with a voltammeter connected to the two inserted electrodes, a reference electrode (saturated calomel) and a counter electrode (platinum wire). Pronounced intensity switching of the fluorescence was observed, by almost a factor of 10, reflecting transitions between the oxidized and the reduced state of Cy5-azurin. Zinc-azurin, used as a control, did not show any fluorescent switching under the same conditions. In addition, the redox-based changes of surface-immobilized Cy5-azurin were investigated by fluorescence lifetime imaging. Fluorescence lifetimes were found to be 0.7 ± 0.15 and 1.8 ± 0.2 ns in the oxidized and the reduced state, respectively. The average midpoint potential is 12 ± 3 mV vs. a saturated calomel electrode, and the distribution of midpoint potentials is characterized by a full width at half maximum of 92 mV. The electron transfer rates for both states vary between 1 and 80 s^{-1} . Remarkably, the distribution of the midpoint potentials is much broader than observed in the fluorescence-detected cyclic voltammetry measurements described in chapter 3. This is tentatively attributed to the difference in the local environment of the Cu-redox center of Cy5-azurin in the two experiments. To the best of our knowledge, we were able to determine for the first time the reaction kinetics and thermodynamic midpoint potential of individual azurin molecules immobilized on a glass substrate.

Samenvatting

In elke levende cel zijn metaaleiwitten betrokken bij een groot aantal elektron-overdrachtsprocessen, voornamelijk in biologische cycli van energieconversie, maar ook in tal van biochemische transformaties in metabolische processen. Het belang daarvan is een sterke drijfveer voor het onderzoek beschreven in dit proefschrift.

De ontwikkeling van nieuwe technieken voor fluorescentiedetectie van één molecuul heeft tot een doorbraak geleid in het onderzoek naar biomoleculaire eigenschappen en functies met optische technieken. Het is nu mogelijk moleculen individueel te bestuderen, en daarmee heterogeniteit, fluctuaties en andere variaties van eigenschappen van overigens identieke moleculen in kaart te brengen. In dit proefschrift worden deze technieken toegepast om gedetailleerde informatie te verkrijgen over electronoverdracht op het grensvlak van een kopereiwit en een goud-electrode. De aanpak is gebaseerd op Förster-resonante energieoverdracht (FRET) in een gelabeld redoxeiwit, waar een plaats-specifiek gebonden, fluorescerend kleurstoflabel (de donor) en het redox-actieve centrum (de acceptor, met een karakteristiek absorptiespectrum) een FRET-paar vormen. De efficiëntie van FRET hangt af van de overlapintegraal van de emissie- en absorptiebanden van, respectievelijk, de donor en de acceptor. Op deze manier kunnen veranderingen in de redox-toestand van het eiwit worden gevolgd door middel van veranderingen in de fluorescentie-intensiteit van het covalent gebonden label: de fluorescentieintensiteit is hoog ("aan") in de gereduceerde en laag ("uit") in de geoxideerde toestand. Detectie van fluorescentie biedt een sterk verhoogde gevoeligheid in vergelijking met absorptiemetingen, tot detectie van individuele moleculen toe.

Voor het werk beschreven in dit proefschrift werd azurine gelabeld met Cy5 als donor in een FRET paar met het Cu redoxcentrum van het eiwit, de acceptor. Voor de metingen aan Cy5-gelabeld azurine, met name die welke beschreven

worden in hoofdstukken 3 en 4, was het noodzakelijk om alle zuurstof te verwijderen uit de oplossing en een extra eiwitzuivering uit te voeren na labeling.

De resultaten beschreven in dit proefschrift laten zien dat fluorescentie-detectie van chemisch en elektrochemisch geïnduceerde veranderingen van de redoxtoestand van een metaaleiwit een bij uitstek geschikte methode is om kinetische en thermodynamische aspecten van het reactiemechanisme van redoxeiwitten op het niveau van één molecuul te verkennen. Vooral fluorescentie-gedetecteerde elektrochemie kan worden gebruikt voor verder onderzoek van eiwit-elektrode- of eiwit-eiwitinteracties. De methode kan eenvoudig worden toegepast op tal van andere redoxeiwitten of -enzymen, en biedt mogelijkheden voor toepassing in op fluorescentie-detectie gebaseerde biosensoren en moleculaire elektronica.

In **hoofdstuk 1** wordt een beknopt overzicht gegeven van de begrippen en methoden die fundamenteel zijn voor dit proefschrift, zoals elektrochemie, enkel-molecuul fluorescentiedetectie en het FluRedox principe. Ook worden enkele belangrijke elementen gememoreerd van de theoretische achtergrond en de thermodynamische beschrijving van elektronoverdracht in biologische redoxreacties.

In **hoofdstuk 2** wordt een nieuwe werkwijze, fluorescentie-gedetecteerde cyclische voltammetrie (FCV), beschreven met toepassing op een monolaag van Cy5-gelabeld azurine. Het gelabeld eiwit werd geïmmobiliseerd op een semi-transparante goud elektrode door adsorptie op een door zelf-assemblage op de goudlaag gevormde monolaag van 1-hexaanthiol of 1-octaanthiol. Conventionele cyclische voltammetrie (CV) werd toegepast met scan-snelheden variërend van 10 mV/s tot 10 V/s. Uit de CV curve van elektrodestroom versus aangelegde spanning bleek de midpunt-potentiaal van azurine 45 ± 5 mV te zijn (bij pH 7) met een verzadigde calomel elektrode als referentie, in overeenstemming met waarden uit de literatuur.

Voor fluorescentie-gedetecteerde elektrochemie werd Cy5-gelabeld azurine geïmmobiliseerd met een relatief lage dichtheid op een semi-transparante goudelektrode door adsorptie op een zelfassemblerende monolaag van 1-octaanthiol die was aangebracht op de goudlaag. De goudlaag fungeerde als de werk-electrode in een electrochemische cel. De fluorescentie-intensiteit van het Cy5 gelabelde azurine bleek af te hangen van de redoxtoestand van het Cu-centrum, die werd bepaald door de aangelegde elektrodepotentiaal. Fluorescentiebeelden van de gefunctionaliseerde werk-elektrode werden snel achter elkaar opgenomen met een hoge tijdsresolutie, synchroon met de variatie in de tijd van de aangelegde potentiaal. Het verloop van de fluorescentie-intensiteit van Cy5-azurine als functie van de elektrodepotentiaal werd gereconstrueerd uit de microscoopbeelden voor verdere analyse. Deze fluorescentie-voltammogrammen van Cy5-azurine werden gemeten bij scansnelheden variërend van 10 mV/s tot 1 V/s. Aan de hand daarvan werden de redoxparameters bepaald door een analyse gebaseerd op de Butler-Volmer theorie. Uit de afhankelijkheid van zowel fluorescentie-gedetecteerde als conventionele cyclische voltammetrie van de scansnelheid werden waarden verkregen voor de midpunt-potentiaal en de snelheidsconstanten voor elektronoverdracht. Deze parameters zijn geassocieerd met slechts een klein aantal moleculen, niet meer dan een paar honderd, door de intensiteitsmetingen te beperken tot enkele pixels in het beeld. Een grote heterogeniteit werd waargenomen in het gedrag van de fluorescentie-intensiteit over het hele oppervlak. De thermodynamische midpunt-potentiaal blijkt tientallen millivolt te variëren over het elektrodeoppervlak, en de snelheid van elektronoverdracht verandert met meer dan een factor 100. Dit onderzoek toont aan dat de combinatie van fluorescentie detectie en cyclische voltammetrie een uitstekend methode is voor onderzoek naar heterogeniteit, elektronoverdracht, wisselwerking met de elektrode, en moleculair gedrag van redox-eiwitten.

In **hoofdstuk 3** worden metingen beschreven waarin de fluorescentie veranderingen van individuele Cy5-azurinemoleculen per electron werden

geregistreerd als functie van de electrochemisch gecontroleerde electrode-potentiaal. De metingen zijn gebaseerd op de hierboven beschreven FRET-detectie van de redoxtoestand van Cy5-gelabeld azurine met voldoende gevoeligheid om individuele moleculen waar te nemen. Daarvoor werd een confocale fluorescentiemicroscoop gebruikt, voorzien van een potentiostaat om een goed gedefiniëerde, elektrochemische potentiaal aan te leggen op de semi-transparante werkelectrode. Deze elektrode bestond uit een dunne goudlaag (~10 nm dik) waarop, net als in het vorige hoofdstuk, een zelf-assemblerende monolaag van 1-octaanthiol was aangebracht om Cy5-azurinemoleculen te adsorberen en te immobiliseren.

De electrochemische activiteit van het systeem werd geverifieerd door metingen van conventionele cyclische voltammetrie. Het gedrag van *individuele* Cy5-azurine moleculen, geïmmobiliseerd op de dunne goudelectrode, kon worden gevolgd door middel van confocale fluorescentiemicroscopie. Afhankelijk van de extern aangelegde potentiaal was de fluorescentie “aan” (gereduceerd azurine) of “uit” (geoxideerd azurine). Door analyse van de fluorescentie-intensiteit als functie van de aangelegde spanning bleek dat de verdeling van de optisch gemeten midpunt-potentiaal van individuele Cy5-azurine moleculen een gemiddelde waarde heeft van 45.7 ± 0.5 mV en een breedte van 15 mV op halve hoogte (ten opzichte van een verzadigde calomel elektrode). Deze resultaten vormen de eerste directe waarneming van fluorescentie-gedetecteerde elektrochemie en de meting van thermodynamische parameters van individuele redoxeiwitten.

In de experimenten beschreven in **Hoofdstuk 4** werd een zelfde methode gebruikt om *chemisch* geïnduceerde redoxreacties van een individueel metaaleiwit te volgen. In dit geval werd het fluorescerend gelabelde eiwit door covalente binding geïmmobiliseerd op het oppervlak van een microscoop-dekglasje. De fluorescentie-intensiteit van individuele Cy5-azurinemoleculen werd gedetecteerd als functie van de redoxpotentiaal in oplossing, gebruik makend van tijd-gecorrleerde telling van fotonen. De chemische

redoxpotential werd gevarieerd door het aanpassen van reductant- en oxidantconcentraties in de bufferoplossing. De potentiaal werd gemeten met een spanningsmeter die was verbonden met de twee electrodes in de bufferoplossing op het gefunctionaliseerde dekglasje, een referentie-electrode (verzadigd calomel) en een meet-electrode (platinumdraad). Metingen aan individuele Cy5-azurinmoleculen toonden stapsgewijze veranderingen van de fluorescentie tussen twee intensiteitsniveaus die verschilden met bijna een factor 10, corresponderend met overgangen tussen de geoxideerde en de gereduceerde toestand van Cy5-azurine. In controle-metingen aan een kunstmatige variant, zink-azurine dat niet redox-actief is, werden onder dezelfde omstandigheden geen veranderingen van de fluorescentie-intensiteit waargenomen.

De gemiddelde midpunt-potentiaal van Cy5-azurinmoleculen die op deze manier werd gemeten is 12 ± 3 mV ten opzichte van een verzadigde calomel electrode, en de verdeling daarvan wordt gekarakteriseerd door een breedte van 92 mV op halve hoogte. De waarden van de snelheid van electronoverdracht van individuele Cy5-azurinmoleculen variëren tussen 1 en 80 s^{-1} . Opmerkelijk is dat de verdeling van de midpunt-potentiaal veel breder is dan die welke is waargenomen in de fluorescentie-gedetecteerde cyclische voltammetrie-metingen in hoofdstuk 3. Dit wordt toegeschreven aan het verschil in de lokale omgeving van het redox-actieve Cu-centrum van Cy5-azurine in beide experimenten. Verder werd het redox-geassocieerde gedrag van het oppervlakte-gebonden Cy5-azurine onderzocht met levensduur-afhankelijk fluorescentie microscopie. De fluorescentielevensduur is 0.7 ± 0.15 ns in de geoxideerde, en 1.8 ± 0.2 ns in de gereduceerde toestand.

Voor zover ons bekend hebben we daarmee voor de eerste keer de reactie kinetiek en thermodynamische midpunt-potentiaal kunnen meten van individuele azurine moleculen, geïmmobiliseerd op een glas-substraat, dan wel een goudelectrode.

List of Publications

N. Akkilic, F. van d. Grient, G.W. Canters, T.J. Aartsma, "Chemically-induced redox switching of a single metalloprotein"; in preparation.

N. Akkilic, J.M. Salverda, G.W. Canters, T.J. Aartsma, "Fluorescent detected electrochemistry on the single redox protein"; in preparation.

J.M. Salverda, A.V. Patil, G. Mizzon, S. Kuznetsova, G. Zauner, **N. Akkilic**, G.W. Canters, J.J. Davis, H.A. Heering, and T.J. Aartsma, "Fluorescent Cyclic Voltammetry of Immobilized Azurin: Direct Observation of Thermodynamic and Kinetic Heterogeneity"; *Angewandte Chemie International Edition*, **49**, 1–5, (2010).

N. Akkilic, M. Mustafaev, V. Chegel, "Conformational Dynamics of Poly(acrylic acid)-Bovine Serum Albumin Polycomplexes at Different pH Conditions"; *Macromolecular Symposia*, **269**, 138 – 144, (2008).

N. Akkilic, Z. Mustafaeva, M. Mustafaev, "High Performance Liquid Chromatography Study of Water-Soluble Complexes and Covalent Conjugates of Polyacrylic Acid with Bovine Serum Albumin"; *Journal of Applied Polymer Science*, **105**, 3108-3120, (2007).

Curriculum Vitae

Namık Akkılıç was born in Istanbul, Turkey, on February 16, 1979. He studied at the Hasan Polatkan High School with extended science education, where after he started his studies in Physics at the Yildiz Technical University. Meanwhile, he completed an internship at the Ford Calibration Laboratories. His final BSc. project supervised by Prof. G. Dereli was on the “Electronic Properties of Single Wall Carbon Nanotubes”. After he obtained his BSc degree in 2003, he successfully completed the study for a MSc. degree in Bioengineering in 2006, at the same university, under the supervision of Prof. M. Mustafaev. His MSc thesis, titled “Investigation of Water-Soluble Complexes and Covalent Conjugates of Polyacrylic Acid with Bovine Serum Albumin by HPLC”, was published in the journal of Applied Polymer Science. From 2005-2008 he worked as a full time research assistant in the Bioengineering Department. In that period, he collaborated with Dr. V. Chegel (Institute of Semiconductor Physic, Ukraine) on Surface Plasmon Resonance Spectroscopy of polymer-protein complexes.

In January 2008, he joined the group of Prof T.J. Aartsma and Prof. G.W. Canters at the Leiden Institute of Physics, The Netherlands as a Marie Curie Early Stage Researcher in the EdRox Research and Training Network. The research was aimed at the control of single electron transfer events of a metalloprotein immobilized on a surface. His work was presented at the Gordon Research conference (Italy) on Single Molecule Approaches to Biology, the European Biophysics Congress (Italy), the Workshop on Single Molecule Spectroscopy (Berlin) and several national conferences. Oral presentations were given at the Biosensor World Congress (UK), the Dutch Meeting on Protein Chemistry (Veldhoven) and in EdRox Network meetings in Modena, Oxford and Leiden.

Starting May 2013, he will continue his academic career as a postdoctoral fellow at the Membrane Technology Group at the University of Twente.

